Understanding Interfacial Chemistry in Metal Based Soft Materials

by

Michael Anthoy-Loren LeRoy

A dissertation accepted and approved in partial fulfillment of the

requirements for the degree of

Doctor of Philosophy

in Chemistry

Dissertation Committee:

Christopher H. Hendon, Chair

Carl K. Brozek, Advisor

Paul Kempler, Core Member

Matthew Polizzotto, Institutional Representative

University of Oregon

Spring 2024

DISSERTATION ABSTRACT

Michael Anthony-Loren LeRoy

Doctor of Philosophy in Chemistry

Title: Understanding Interfacial Chemistry in Metal Based Soft Materials

Soft materials are a class of materials including colloids, polymers, DNA, and proteins. Due to their organization on the mesoscopic length scales they exhibit a wide variety of properties such as self-assembly and response to external stimuli. This has led soft materials to be employed in a wide array of applications ranging from catalysis, electrochemistry, and membrane technologies. Ionic liquids and metal-organic framework are two distinct classes of hybrid organic-inorganic soft materials, that are well studied and used as filler materials for polymer membrane separation technologies. However, a current challenge is understanding how the interfacial chemistry between these filler materials and polymer impacts membrane structures and properties. In this dissertation, molecular chemistry is used to explore how mesoscopic properties give rise to those found in the bulk of ionic liquids and nanoscale metal-organic frameworks respectively.

This dissertation includes previously published material co-authored material.

CURRICULUM VITAE

NAME OF AUTHOR: Michael A-L LeRoy

GRADUATE AND UNDERGRADUATE SCHOOLS ATTENDED:

University of Oregon, Eugene, OR
University of California-Santa Cruz, Santa Cruz, CA

DEGREES AWARDED:

Doctor of Philosophy, Chemistry, 2024 University of Oregon
Bachelor of Science, Chemistry, 2012 University of California-Santa Cruz

AREAS OF SPECIAL INTEREST:

Metal-Organic Frameworks
Ionic Liquids
Colloids
nanomaterials

PUBLICATIONS:

LeRoy, M.A.; Perera, A.S.; Laminchhane, S.; Mapile, A.N.; Khaliq, F. Kadota, K.; Zhang, X.; Ha, S.; Fisher, R.; Wu, D.; Risko, C.; Brozek, C.K., *Chem. Mater.*, **2024**, *36*, 8, 3673-3682 https://doi.org/10.1021/acs.chemmater.3c03191

LeRoy, M.A.; Mroz, A.M.; Manusco, J.L.; Miller, A.; Van Cleve, A.; Check, C.; Heinz, H.; Hendon, C.H.; Brozek, C.K., *J. Mater. Chem*, **2020**, *8*, 2267-22685 https://doi.org/10.1039/D0TA06195F

ACKNOWLEDGMENTS

This wouldn't have been possible without the amazing amount of support of the communities I've had the privilege of being apart of in my life. To the chemistry department at the University of Oregon, for being a place to be myself and accepting me when the outside world felt uncomfortable. Thank you, Carl Brozek, for the opportunity to join and work in a new lab, while giving me the grace to make and learn from my mistakes while growing as a scientist. To all the lab members past and present, I appreciate all the discussions and challenges we've overcome as the lab has grown throughout the years. I look forward to seeing what the future lab looks like in just a few years. To my friends and community and Eugene thank you for keeping me grounded and showing me, you don't have to be an academic to be successful individuals. For all the communities from Illinois to California, thank you for all the love, support, and wisdom you've given me throughout the years this wouldn't have been possible without all of you.

DEDICATION

This dissertation is dedicated to all the family and friends, throughout the years human and animal. Especially Cat and Sulu for always being the safe harbor I didn't know I needed.

TABLE OF CONTENTS

LIST OF FIGURES

Figure Page

LIST OF TABLES

Table Page

LIST OF SCHEMES

Chapter I.

Introduction

Soft materials are a diverse class of materials that include rubbers, adhesives, liquid crystals, colloids, polymers, food and living tissues.[1,2] The softness of these materials comes from their low elastic moduli and ability to withstand deformations in structure from applied stimuli. The organization of these materials are unique in that they are on the nm to μm or mesoscopic scale due to the self-organization of their atomic or molecular constituents. The behavior of the material at the microscopic scale has distinct impacts on the behavior at the macroscopic scale arising from the complex intermolecular interactions at play.

For soft materials a fundamental understanding of structure-property relationship is important to understand for applications. The understanding of structure and property is enhanced when soft materials are combined with nanotechnology to form the field of soft nanotechnology. By making use of soft materials ability to self-assemble, fine control can be used to create precise nanostructured materials for optics, electronics, and mechanics that have well defined and tailored properties.[3,4] Self-assembly is important as it allows for the templating of materials in a patterned and order fashion, such as the formation of monolayers or vesicles.

Soft materials are able to self-assemble because the energy that is released by molecular or particle motions and reorientations, are comparable to the thermal energy K_bT or the Brownian motion.[5] The low thermal energy barrier of these materials at the nanoscale makes them highly susceptible to influences brought on by external stimuli due to weak non-covalent interactions that are easily broken and reformed. The ease at which soft matter can undergo restructuring leads to a diverse set of phase transitions these materials are able to undergo. The weak intermolecular interactions at play in the ordering of soft materials consist of hydrogen bonding, van der Waals interactions, ionic interactions, coordination bonds, and hydrophobic interactions.

Hydrogen bonding for example plays a predominant role in protein interactions, where water is a stabilizing force for protein structure. Whether that be proteins in the α helix or β sheet structure, the degree of hydrogen bonding in the folded protein give rise to its stability. The more hydrogen bonds in the protein the more stable and lower the free energy and vice versa. This is due to the hydrogen bonds having a strength of around 20 kJ mol^{-1}, allowing for superstructures to from without the need of chemical reactions and the strength to maintain shape once formed.

Electrostatic and van der Waals are important interactions that influence the stability of colloidal systems. Colloidal systems such as those found in paints need to be stabilized to ensure a long shelf-life. This can be accomplished by having charged particles in electrolyte medium, that balances the repulsive electrostatic forces with those of the balancing van der Waals interactions.[4,6] Another method of to prevent aggregation of colloidal systems is through steric stabilization by long-chain molecules such as polymers or fatty acids that are attached to the colloidal particle surface and cause particle repulsion.

With the Nobel prize in physics being awarded to Pierre-Gilles de Gennes in 1991, there has been a strong focus to better understand and comprehend the field of soft materials.[7,8] In particular, the integration of inorganic and hybrid nanomaterials for use in creating colloidal suspensions. Of the soft materials for this integration process, the most well studied and know are polymers. From the fundamental research on polymer growth mechanisms, to the large scalability, interest as industrial materials, and fine synthetic control and versatility polymers have been an ideal candidate for the incorporation of inorganic materials. Polymers are an interesting class of soft material due to the wide synthetic scope and degree of applications. They can be used to create hydrogels that are highly biocompatible and have tunable mechanical properties.[9–11] Other classes of polymers include block copolymers, which consist of multiple chemically distinct blocks of polymers connected end to end, star polymers macromolecules polymeric chains anchored to a center point, and dendrimers which are starburst molecules.[6,12] Due to the block copolymers having distinct domains based upon the homopolymers in each segment, they have the ability to self-assemble into distinct assemblies on the mesoscopic scale.[13] Within the field of polymers there are already a wide range of soft materials to study from theoretical, synthesis, and structural understanding as they relate to materials properties.

Though the field of polymers is important to the field of soft materials, they're limited by the fact that they are primarily organic molecules, which has limits on versatility and applications. To overcome this barrier creating materials that are hybrids of both organic and inorganic molecules is ideal. By combining both organic and inorganic systems together, properties of both can be realized all in one single material in a cohesive and tailored manner.[14] Through the use of organics physical properties such as flexibility, hydrophobicity, and connectivity can be applied. While the use of inorganic moieties can enhance mechanical or thermal stability, improve electrical conductivity, and modulate viscoelastic properties. Of the

many hybrid materials studied ionic liquids and nanosized metal-organic frameworks have unique properties and applications.

Ionic Liquids

Ionic liquids (ILs) offer a unique platform for materials design due to their composition being a mixture of low molar mass cations and anions, without the need for solvent.[15,16] Specific properties that ILs have are low vapor pressure, low melting temperature, high thermal stability, wide electrochemical window, and nonvolatility to name a few.[17–19] ILs are often called designer solvents due to the ability to have highly systematic control of both the cation and anions involved to make these materials.[20,21] This lends ILs to have a plethora of combinations to achieve specific design and materials properties. Due the diversity of ILs these materials are able to show a variety of intermolecular interactions that influence the overall physiochemical properties. These intermolecular interactions include electrostatics, hydrogen bonding, van der Waals forces and π-π stacking.[22–24]

The most commonly used cations consistent of 1-methyl-3-alkylimidazolium, N-alkyl-N-alkyl-pyrrolidnium, 1,2-dialkylpyrazolium, N-alkyl-pyridinium, tetraalkylammonium, and tetraakylphosphonium.[25] For anions the most common are thiocyanate, halides, sulfates, nitrates, acetates, tetrafluoroborate, hexafluorophosphate, and bis(trifluoromethane)sulfonimide. Though a wide combinations of ILs exist, the most widely studied are those based on the 1-methyl-3-alkylimidazolium cations for applications that include gelation, polymer solubility, electrochemistry, and understanding physiochemical properties.[18,19,26–30]. Even with the recent expansion of ILs into colloidal ionic liquids (CILs) a subclass of polymerized ionic liquids (PILs), which cover the nano to meso length-scales and distinct topologies from 0D-3D, the majority of the synthetic work focuses on organic based building blocks for both cations and anions, giving more synthetic space but limited moieties to choose form.[31] Even with the limited structural diversity of ILs they have been widely used as on component in membrane technologies which will be discussed in detail further on.[31,32] However a fundamental understanding of the interfacial interactions that govern ILs as single components is needed to better grasp how they impact membrane functionalization when combined with multiple and diverse systems such as polymers, silicas, zeolites and metal-organic frameworks (MOFs). These materials range from traditional solely organic and inorganic materials to hybrid

inorganic/organic materials which range from non-porous to porous hard materials to soft materials.

Nano Metal-organic frameworks

Metal-organic frameworks (MOFs) are well known porous-coordination polymers that have attracted a significant amount of attention due to their porosity, large surface areas, tunable pore sizes and topologies, and wide synthetic tunability.[33,34] MOFs are composed of metal ions and organic linkers ranging from single ion clusters to metal chain clusters, allowing for wide combination of metal and linker idenitites.[35–37] MOF synthesis is traditionally done through hydrothermal or solvothermal methods using polar solvents such as DMF, water, water, and alcohols.[14] With these relatively simple building blocks the field of MOF chemistry has grown exponentially with over 20,000 MOF structures having been identified and under study.[38]

MOFs with their wide range of structures offer a scaffold for studying a diverse array of applications such as gas adsorption, catalysis, sensors, etc.[39] Though MOFs due to their hybrid organic-inorganic nature offer better tunability compared to other porous materials such as zeolites, the majority of them are synthesized as bulk materials and need to be nanosized in order to increase their use for diverse applications.[40,41]By nanosizing MOFs into nanoMOFs materials they have an increase in surface to volume ratio, particle size control, and solution processability. Unfortunately, of all the MOF structures available only a few have been synthesized as nanoparticles through the use of modulators as competitive binding moieties.[42] Though a "seesaw" model for nanoMOF growth has been proposed, and has allowed for the synthesis of 6 nm MOF particles still is left to understand how nanoMOFs interact in colloidal and filler materials[43,44]. This understanding is important as MOFs are important filler materials for use in gas separation technologies such as mixed-matrix membranes (MMMs) that employ polymers and other materials as substrate and binder materials respectively.[45–48]

Mixed-Matrix Membranes

Gas separation plays a crucial role in today's energy and chemical production industries, for the capture of fossil fuels, purification of plastics, and isolation of gases. Within the U.S alone the separation industry uses 16 quadrillion BTU of energy per year, due to the use of separation technology for thermally driven reactions such as distillation.[49] Distillation is a high energy consumption process with over 200 unique separation globally, with the largest being olefin/paraffin separation.[50] The current distillation separation method of olefins/paraffins relies

on their differences in volatility, which is a difference between 170 and 184K. Due to the small difference in volatility, necessitates the use of large towers between 200-300 feet tall and high reflux ratio just to achieve 99.9% pure olefins, that still require further purification downstream of this already energy intensive process.[51] This is an example of one high energy cost distillation process that requires a shift away from current technology to new methodologies to not only reduce energy consumption but increase separation efficiency and lower overall costs to producers and consumers. To this end the use of membrane technologies has become an attractive candidate for separation technology that improves efficiency and cost.

Membranes are an attractive form of separations technology due to their energy cost as they don't require feedstock to undergo a thermally drive phase change or the regeneration of solid or liquid adsorbents. For gas-based separation membranes are simply able to rely solely on the intrinsic properties of gas diffusion and sorption, which is dictated by the identity of the membrane. Monsanto in 1977, was the first company to launch the use of membranes as an industrially relevant separations technique for hydrogen purge recovery from petrochemical and ammonia plants.[52] When looking at materials used in membrane technologies for gas separation a few important factors need to be considered: permeability, membrane structure and thickness, configuration and overall design.[53] Permeability is the rate which a gas is able to move through the membrane based upon thermodynamics and kinetics. Selectivity is another key parameter for achieving high product purity at high rates of recovery. For most gas-separation membranes, industry has turned towards the use of organic polymers, due to the ability to be spun into hollow fibers therefore increasing their surface-area to volume ratios, resulting in an increase in performance and efficiency.

A drawback of polymers is that they cannot withstand the high temperatures and harsh chemical environments of due to exposure to CO_2 and petrochemicals leading them to swell or plasticize, causing a decrease in efficacy and potentially being irreversibly damaged. Polymers also show a distinct trade-off between permeability and selectivity for specific gases, this limit is known as the Robeson upper bound.[54] In addition the variety of polymers currently employed in membrane technologies is limited and lacks diversity. To improve the performance of polymer based membranes for both selectivity and permeability, the addition of a filler material to the polymer matrix has been employed, i.e. mixed-matrix membranes (MMMs). MMMs are

composed of a polymer matrix the continuous phase and inorganic micro- or nanocrystalline particles dispersed the discrete phase into the polymer.

By combining these two materials, an ideally synergistic effect is created where the ease of processability of the polymer and the higher performance of the inorganic filler increase the overall performance of the composite membrane. While MMMs have been shown to have increased physical, mechanical, and thermal properties; they still have disadvantages in interfacial defects, brittleness, ideal ratio of filler to polymer, etc.[47,48] Other considerations that industry and researchers should consider is filler identity whether it be a porous or non-porous material such as zeolites or silica nanoparticles. This choice will influence the way the target moieties are separated such as solution-diffusion mechanism, Knudsen diffusion, surface diffusion, or molecular sieving.[55]

MOFs have been an attractive candidate for use in MMMs due to their porous nature, organic linker that allow for favorable interactions with the polymer matrix, and tunable chemistries for gas selectivity. Some MOFs such as ZIF-8, HKUST-1, and UiO-66 are able to nanosized which allows for better integration with the polymer due to better adhesion and less generated void space between the MOF and polymer. However, one current draw-back is the need to prevent agglomeration of the nanoMOFs, low MOF loadings and the lack of a fundamental understanding of the MOF/polymer intermolecular interactions as they apply to the structure-property relationships of the MMM.[56] By understanding the intermolecular interactions of the hybrid material, more selective membrane fabrication can be developed for a wider variety of gas separations, and increase the usage above the Robeson upper bound.

Ionic liquids have also been implemented in membrane technologies specifically for use in CO_2 separations. A variety of ionic liquid membrane architectures have been deployed and studied such as, supported ionic liquid membranes, polymer/IL membranes, gelled IL membranes and poly(ionicliquid)-(PIL) based membranes.[32] A recent advance of the IL membrane field has been the development of ionogel membranes, which incorporate ionic liquids dispersed in a solid continuous phase such as a polymer matrix. When combined with an inorganic filler a new subclass of MMMs has been developed, that of mixed-matrix ion gel membranes.[57] The addition of ILs to MMM matrix has the added advantage of decreasing the poor adhesion between polymer and filler materials, filling of interfacial defects, and improved selectivity. Though showing promise this class of MMMs is relatively new and more research is

needed to evaluate these materials as compared to industry standard membranes. In order to do so a fundamental understanding of the individual components is needed, in order for a judicious decision to be made when targeting a specific separations application.

The focus of this dissertation is to apply molecular chemistry to investigate the intermolecular interactions involved in two classes of soft materials and the impact on structure-property behaviors, specifically perhalometallate ionic liquids and nanoMOFs. In Chapter II, the use of perhalometalle anions in ionic liquids to use post-synthetic modification and monitor the influence of structural composition on IL composition and viscoelastic properties. Work from this chapter was previously published from LeRoy, M.A.; Mroz, A.M.; Manusco, J.L.; Miller, A.; Van Cleve, A.; Check, C.; Heinz, H.; Hendon, C.H.; Brozek, C.K., *J. Mater. Chem*, **2020**, *8*, 2267-22685 https://doi.org/10.1039/D0TA06195F. In Chapter III, we investigated the forces that govern the colloidal stability and solubility of nanoMOF particles, demonstrating the solvent-linker interactions dictate stability. This work was previously published from LeRoy, M.A.; Perera, A.S.; Laminchhane, S.; Mapile, A.N.; Khaliq, F. Kadota, K.; Zhang, X.; Ha, S.; Fisher, R.; Wu, D.; Risko, C.; Brozek, C.K., *Chem. Mater.*, **2024**, *36*, 8, 3673-3682 https://doi.org/10.1021/acs.chemmater.3c03191. These findings elucidate important intermolecular interactions in soft materials, that can be extended to understanding the structure-property relationships that govern MMM efficiency and selectivity for gas separations.

Chapter II

Post-synthetic modification of ionic liquids by ligand-exchange and redox chemistry

Work in the chapter was published from LeRoy, M.A.; Mroz, A.M.; Manusco, J.L.; Miller, A.; Van Cleve, A.; Check, C.; Heinz, H.; Hendon, C.H.; Brozek, C.K., *J. Mater. Chem*, **2020**, *8*, 2267-22685 https://doi.org/10.1039/D0TA06195F.

As molten salts below 100 ºC, ionic liquids (ILs) find widespread use as non-aqueous high-concentration electrolyte media with low volatilities, high thermal stabilities, and wide electrochemical windows.[58–62] These "solvent-free" electrolytes can improve the performance of redox flow[62–66] and multivalent-ion batteries,[67] dye-sensitized solar cells,[68–70] capacitors,[71–73] thermoelectrics,[74–76] and electrocatalysts[77] by enhancing ion mobility[78] or by forming bonds with reactive substrates.[77,79–84] In these applications, ILs serve as bulk materials, but their functional properties derive from the molecular composition of the cations and anions. Through competing intermolecular interactions,[85] the constituent ions generate supramolecular structures[86] that govern bulk properties such as viscosity and conductivity.[87] For instance, Kornyshev has proposed that ion composition and molecular steric bulk and ion-pairing produce the non-classical electrical double layer capacitance of ILs.[88–92]

Despite the importance of molecular composition in controlling the functional properties

Scheme 2.1

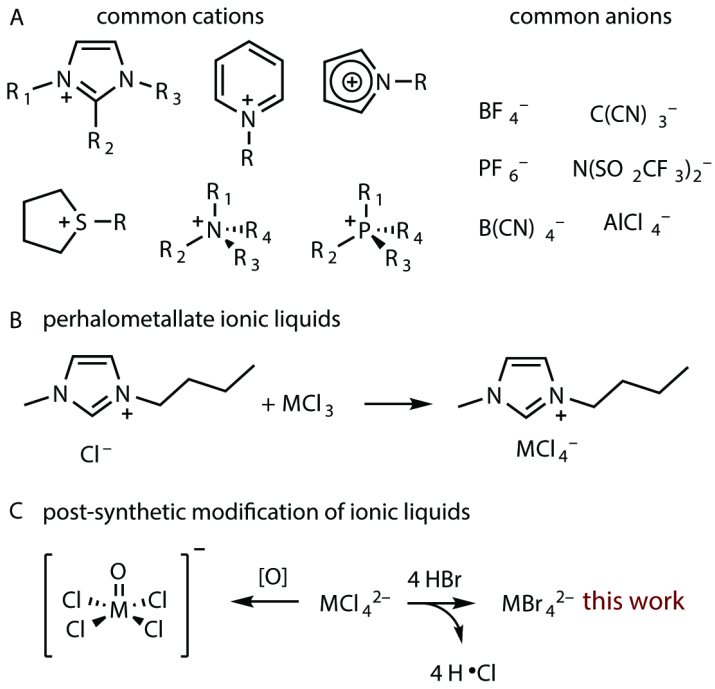

of ILs, several key challenges remain. First, whereas the vast majority of IL research has

explored a wide set of organic cations, little is known about the impact of anions due to their limited tunability. Second, greater insight into the supramolecular structure and molecular speciation of ILs is required for their design as advanced electrolytes, especially at electrode interfaces. Third, we lack general design rules for predicting the magnitude of the effect of specific intermolecular interactions on the bulk behavior of ILs.

Scheme 2.1A shows common cations and anions incorporated into ILs. The cations are typically organic species, such imidazolium, phosphonium, pyridinium, or sulfonium ions, with long alkyl chains amenable to functionalization, whereas the anions tend to be inorganic species lacking straightforward tunability. Therefore, while systematic modification of cation functional groups has revealed interesting relationships between composition and bulk properties, such as the non-linear dependence of viscosity on alkyl chain length,[93] similar studies with anions have not been possible. A promising platform for such structure-property investigations is the perhalometallate anions because they can be prepared with alkaline earth and transition metals, and main group and f-block elements through single-step halide abstraction reactions (Scheme 1B).[67,94–100] To-date, most perhalometallate anion examples include only chloride ligands, however, and little is known about how the composition of these anions dictate supramolecular ordering, which, in turn, controls functional behavior such as viscosity, conductivity, and electrical double layer capacitance. Additionally, certain perhalometallate anions, including $SnCl_3^-$, $ZnCl_4^{2-}$, and $AlCl_4^-$,[67,94,95] exist in dynamic equilibrium with species of varying nuclearities and coordination numbers. Employing these ILs in technologies such as multivalent ion batteries requires identification of the anion speciation, but current analysis relies on difficult interpretations of Raman spectra. Clearly, alternative synthetic and analytical methods are needed for a molecular understanding of IL function as solvents and electrolytes.

Here, we report post-synthetic modification of perhalometallate anions to achieve ionic liquid-to-ionic liquid transformations and apply electronic absorption spectroscopy for insight into their molecular and supramolecular environments. By treating perhalometallate anions as coordination compounds, we reimagine ligand exchange and redox chemistry as facile tools for precise modification of ILs that can be confirmed through routine UV-visible-NIR measurements. This convenient application of electronic absorption spectroscopy allows insight into the competition between intermolecular interactions, permitting quantification of how variable intermolecular interactions ranging from dispersion to covalent dictate bulk properties

such as viscosity. These insights combined with post-synthetic modification provide powerful tools to control IL properties for their application in diverse technologies.

Experimental Section

Materials and Equipment. All manipulations were performed under an atmosphere of nitrogen in an LC Technology Glovebox or by using standard Schlenk techniques. Phosphonium salts, anhydrous VCl_3, and anhydrous VBr_3 were purchased from commercial sources and used without further purification. Hydrated metal salts and imidazolium salts were heated to 100˚C under reduced pressure for 2 days. Tetrabutylammonium hexafluorophosphate ($TBAPF_6$) was recrystallized from ethanol prior to use. Solvents were purified using a LC Technologies SP-1 solvent purification system.

Synthetic Procedures. Synthesis of the materials was carried out by a modification of a literature procedure.[1] In a general procedure the imidazolium or the phosphonium salts were combined with the corresponding metal halides in a 2:1 molar ratio for divalent metals, and 1:1 molar ratio fortrivalent ions, respectively. The mixtures were heated to 100˚C under reduced pressure until a homogeneous mixture was obtained.

Material Characterization. UV-Vis measurements were conducted using a Perkin Elmer Lambda 1050 UV/Vis/NIR spectrometer, with a 150mm InGaAs integrating sphere over 2500-200 nm. Electronic absorption spectra of neat samples were prepared by placing a drop of the ionic liquid between two glass slides. IR spectra were collected on a Bruker Alpha II with an ATR attachment in a nitrogen filled glovebox. X-band EPR spectra were recorded on a Bruker Elexys E 500 at room temperature. Rheological measurements were conducted on a TA Instruments Discovery HR-2 hybrid rheometer, using a Peltier cone plate (Al), 40mm, 1.021˚, and 26-μm truncation gap. Variable temperature rheometry was conducted between 25-200˚C at a shear rate of 10 rad/s. DSC measurements were collected using a DSC 2910 (Du Pont Instruments), cooled with liquid N_2. Electrostatic potential maps were generated by coloring the electron density isosurface plotted up to 0.03 eV/Å^3 according to its electrostatic potential; regions colored red are associated with relatively positive areas of the molecules. IL densities were determined by using the volume displacement method. A graduated cylinder was filled with hexanes as non-polar solvent and weighed. The IL was then added to the graduated cylinder, with the change in

volume and mass recorded. Molar volume was calculated by dividing the molecular weight of each IL by their respective densities.

Results and Analysis

We synthesized a suite of previously reported[97] ILs containing 1-butyl-3-methylimidazolium ([BMIm]$^+$) cations and a variety of perchlorometallate anions based on the hypothesis that, as coordination compounds, these anions would be amenable to redox and ligand-exchange manipulations, although such chemistry had not been demonstrated with ILs.

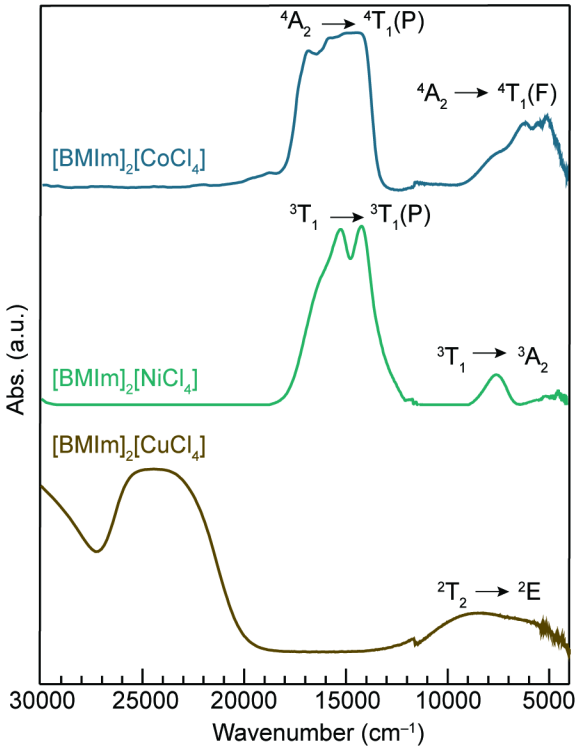

Figure 2.1: Absorption spectra of neat ionic liquids 1-butyl-3-methylmidazolium (BMIm) perchlorometallate ions. [BMIm]$_2$[CoCl$_4$] in blue, [BMIm]$_2$[NiCl$_4$] in green, and [BMIm]$_2$[CuCl$_4$] in yellow.

Through facile combination of BMImCl and metal chloride salts in the appropriate stoichiometric ratios, free-flowing colored liquids were generated in single-step routes with proposed formulas BMIm$_x$*M*Cl$_4^{x-}$ (*M* = Cr^{3+}, Fe^{3+}, Mn^{2+}, Co^{2+}, Ni^{2+}, and Cu^{2+}). Determining the purity of ILs typically involves NMR spectroscopy,[101–103] which probes the identity of the organic cations, detects for adventitious water content, and yet applies to only certain perhalometallate anion nuclei, such as ^{119}Sn.[104] Given the propensity of perhalometallates to

speciate into complex anionic equilibrium mixtures, we sought analytical methods with broader applicability.

Figure 2.1 plots electronic absorption spectra of neat ILs composed of $[BMIm]^+$ and $CoCl_4^{2-}$, $NiCl_4^{2-}$, and $CuCl_4^{2-}$ perhallometallate anions. Spectra collected for ILs containing Cr^{3+}, Fe^{3+}, and Mn^{2+} are shown in Figure A1. All spectra in Figure 2.1 display ligand field (d-d and charge transfer) bands expected of these ions in tetrahedral chloride environments. For precise verification of anion speciation, we performed ligand field analysis to derive the ligand field parameters *Dq*, which measure ligand bonding character, and Racah parameters *B*, which quantifies the interelectronic repulsion experienced by metal d-orbital electrons. As both parameters depend on the geometries and ligand environments of metal ions, they provide exceptional accuracy in assigning metal ion speciation. Analysis of the Co-containing material gives *Dq* and *B* values of 315.82 cm^{-1} and 791.92 cm^{-1} respectively, which agrees with previously reported values for tetrahedral $CoCl_4^{2-}$.[105–107] The spectral bands centered at 15492 cm^{-1} and 5592.5 cm^{-1} can thus be assigned to the $^4A_2 \rightarrow {}^4T_1(P)$ and $^4A_2 \rightarrow {}^4T_1(F)$ transitions, respectively. For the Ni-containing IL, assigning the bands at 14999 cm^{-1} and 7511.7 cm^{-1} to the $^3T_1 \rightarrow {}^3T_1(P)$ and $^3T_1 \rightarrow {}^3A_2$ electronic transitions gives D*q* and *B* values of 408.01 cm^{-1} and 812.76 cm^{-1} respectively. These values are each approximately ~50 cm^{-1} higher than prior analysis of $NiCl_4^{2-}$ ions, but this result can be attributed to distortions in the geometry of the anion.[105,107–109] Finally, assignment of the band at 8337.2 cm^{-1} at for the Cu-containing spectrum to the $^2T_2 \rightarrow {}^2E$ transition of tetrahedral Cu^{2+} gives a *Dq* value of 368 cm^{-1}, which is consistent with a chloride ligand field for a $CuCl_4^{2-}$ with a slight distortion from ideal tetrahedral geometry.[107,110] As expected for metal ions with d^5 electronic configurations, spectra of the Fe^{3+}- and Mn^{2+}-based ILs did not display d-d transitions (Figure A1). Interestingly, the spectrum of the Cr^{3+} IL showed hallmark ligand field bands expected for O_h, rather than T_d, symmetry, suggesting this ionic liquid contains $CrCl_6^{3-}$ instead of $CrCl_4^-$ anions.[111,112] Although water contamination poses a constant threat to IL purity, the sensitivity of these spectra provide clear proof of the absence of water in the metal ion environments. Therefore, electronic absorption spectroscopy serves as a powerful method for understanding IL speciation.

Equipped with a method to probe the coordination environments of IL anions, we sought to demonstrate post-synthetic modification by ligand exchange chemistry. Halide exchange of the $CoCl_4^{2-}$ IL served as an initial target due to the well-resolved spectral bands that would offer

convenient handles for monitoring reaction progress. Treating $[BMIm]_2[CoCl_4]$ with aqueous HBr caused an immediate color change from blue to green, consistent with Co^{2+} entering the weaker ligand environment of Br^-. Due to the miscibility of $[BMIm]^+$ with water, however, extraction of the product was difficult, resulting in low yields. Instead, we repeated a similar procedure using trihexyltetradecylphosphonium ($[P_{6,6,6,14}]^+$) as the cation due to its enhanced hydrophobicity. Layering of $[P_{6,6,6,14}]_2[CoCl_4]$ onto a 1-M HBr aqueous solution followed by vigorous shaking resulted in clean separation of a green viscous liquid from the aqueous layer that could be removed by simple decanting. Following drying procedures, successful ligand exchange was confirmed by UV-vis-NIR spectroscopy of the resultant neat ionic liquid. Figure 2.2 shows the $^4A_2 \rightarrow {}^4T_1(P)$ transition split by spin-orbit coupling for the product as the red dotted trace, which matches the spectrum of $[P_{6,6,6,14}]_2[CoBr_4]$ prepared directly (brown dashed trace). Both spectra appear red-shifted relative to the spectrum of $[P_{6,6,6,14}]_2[CoCl_4]$ (blue solid trace), which is consistent with the weaker ligand field of Br^-.[113] Interestingly, temperature-dependent viscoelastic measurements of these Co-based ILs evidenced a three-fold decrease in the room-temperature viscosity from 20.77 to 80.96 Pa·s following Br-exchange (Figure S2). The magnitude of this viscosity change is expected between ILs with significantly different cations, but was not expected for anions that only differ in the identity of halides ligands. Additionally, the viscosities of these ILs are higher than monoanionic chlorometallate ILs,[114–117] which could be attributed to greater Coulombic attraction resulting from the dianionic charges.

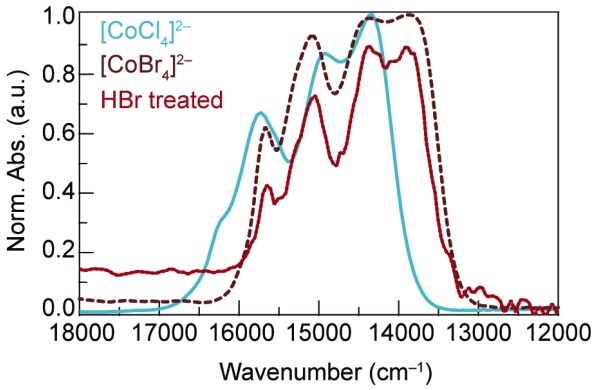

Figure 2.2: Electronic absorption spectra of neat ionic liquids composed of trihexyltetradecylphosphonium ($P_{6,6,6,14}$) perhalocobaltate ions synthesized directly or through post-synthetic ligand exchange. Spectra in blue and brown correspond to directly synthesized $[CoCl_4]^{2-}$- and $[CoBr_4]^{2-}$-based ionic liquids. The spectrum of the $CoBr_4^{2-}$ prepared through ligand exchange is shown in red.

To further explore another strategy for post-synthetic modification of ILs, we investigated redox chemistry. In surveying viable perhalometallate anions, vanadium-based ions are noticeably absent the IL literature which we suspected was due to their air sensitivity. To test this hypothesis, we attempted the preparation of $[BMIm][VCl_4]$ in air and observed color changes from violet to dark green, suggestive of aerobic oxidation. Indeed, a UV-vis-NIR spectrum of the resulting neat green liquid displayed absorption bands consistent with V^{4+} in chloride ligand spheres, rather than V^{3+}.[118] Therefore, we reattempted the synthesis of $[BMIm][VCl_4]$ under an inert atmosphere, which resulted in a highly viscous violet material that retained its color indefinitely. For ease of handling, we synthesized an analogous blue IL with $[P_{6,6,6,14}]^+$ cations due to its significantly lower viscosity. Deliberate exposure of this liquid to air caused a single-step color change from blue to green, as evidenced by UV-vis-NIR spectra of the

Scheme 2.2

neat material before and after reaction completion (Figure 2.3A). To verify that the reaction proceeded through a single-step process, a 4.35-mM MeCN solution of $[P_{6,6,6,14}][VCl_4]$ was prepared in an air-free cuvette, opened to atmosphere, and monitored by UV-vis spectroscopy

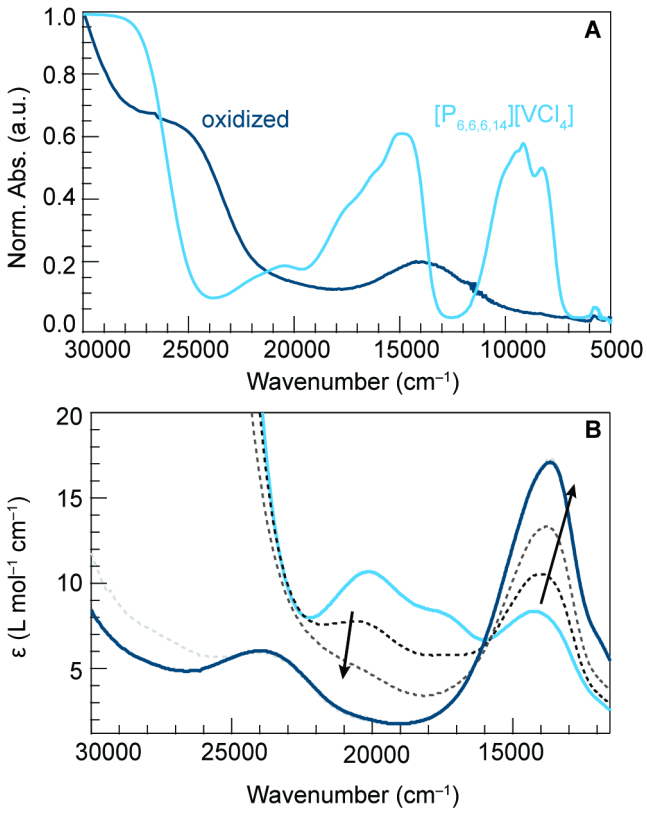

Figure 2.3: Absorption spectra of $[P_{6,6,6,14}][VCl_4]$ and $[P_{6,6,6,14}]_2[OVCl_4]$ prepared neat (A) and dissolved in MeCN (B). Light blue and green correspond to the $[P_{6,6,6,14}][VCl_4]$ and $[P_{6,6,6,14}][VOCl_4]$, respectively. Data in panel B were collected by preparing a 4.35 mM MeCN solution of $[P_{6,6,6,14}][VCl_4]$ that was kept air-free and then introduced to air. Arrows indicate the direction of spectral evolution.

over a 5-hour period whereby the solution turned from light purple to light green (Figure 2.3B). Indeed, the time-evolved spectra reveal an isosbestic point, indicating a single-step reaction that proceeds only by introduction of air. Interestingly, this reaction requires both moisture and O_2. Based on previous mechanistic studies of VCl_3 oxidation to vanadyl ions, we propose the mechanism shown in Scheme 2.2.[119,120] Comparison of the data in Figure 2.3 to spectra of vanadium-chloride eutectic mixtures suggested the oxidation of V^{3+} to V^{4+} to generate a vanadyl-based ionic liquid.[121–124]

Confirmation of vanadium oxidation and generation of a V=O vanadyl moiety was achieved by measuring ATR-IR and X-band EPR spectra of $[P_{6,6,6,14}][VCl_4]$ before and after air exposure. Comparison of the IR spectra shows the growth of a band around 1000 cm^{-1}, which is consistent with literature reports for V=O stretching modes (Figure 2.4A).[125] Whereas $[P_{6,6,6,14}][VCl_4]$ is EPR silent, as expected for S=1 from a d^2 electronic configuration, the air-exposed product displays the characteristic splitting pattern for V^{4+} resulting from a d^1

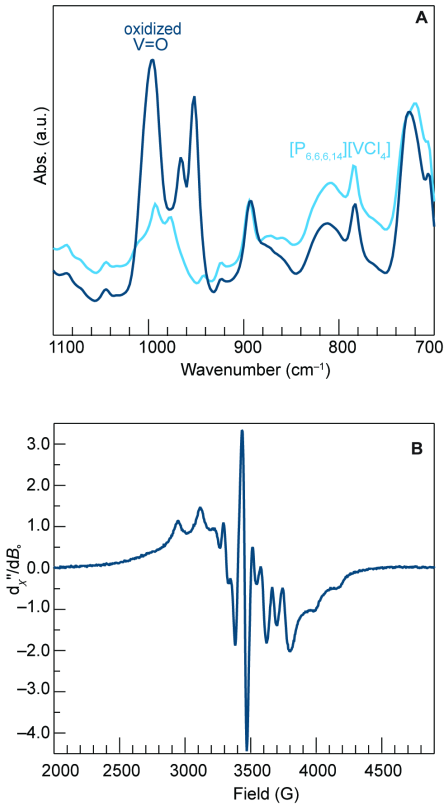

Figure 2.4: Spectroscopic evidence for post-synthetic conversion of VCl_4^- ions into $OVCl_4^{2-}$. (A) ATR-IR spectra of $[P_{6,6,6,14}][VCl_4]$ (blue) and $[P_{6,6,6,14}]_2[VOCl_4]$ (green). (B) X-band EPR spectrum of $[P_{6,6,6,14}]_2[VOCl_4]$. Neat ionic liquids were used for all measurements and air-free. EPR data were collected at 25ºC with a microwave frequency of 9 GHz.

configuration with hyperfine splitting to a nuclear spin of I=7/2 (Figure 2.4B).[122,126] Whereas an octahedrally symmetric V^{4+} center would display an eight-line pattern, the data in Figure 2.4B show additional peaks that would arise from the axial symmetry of a vanadyl chloride anion. To distinguish between $O{=}VCl_4^{2-}$ and $O{=}VCl_3^-$ as the resulting IL anion, time-dependent density functional theory (TD-DFT) calculations were performed and compared to the experimental spectrum of the neat material (Figure A13). The additional bands at 22,000 cm^{-1} and 7,000 cm^{-1} predicted for the $O{=}VCl_3^-$ anion suggests $[P_{6,6,6,14}]_2[VOCl_4]$ as the true identity. Redox activity of $[P_{6,6,6,14}][VCl_4]$ was further explored by cyclic voltammetry. Variable scan rate data were collected air-free using MeCN solutions of $[P_{6,6,6,14}][VCl_4]$. Traces in Figure A3 display several electrochemically irreversible reduction and oxidation waves akin to data previously reported for vanadium-chloride electrolytes employed in redox flow batteries.[127,128] We tentatively assign the wave at ~ –0.3 V (vs. Ag wire) to the $V^{3+/2+}$ couple, and the waves at ~ 0.3 V and ~ 0.8 V to the

$V^{3+/4+}$ and $V^{4+/5+}$ couples, respectively. Room temperature viscosity measurements of $[P_{6,6,6,14}][VCl_4]$ and $[P_{6,6,6,14}]_2[VOCl_4]$ gave values of 5.07 Pa·s and 2.59 Pa·s respectively.

To explore the generality of redox as a post-synthetic modification technique for ILs, we revisited a prior report on the oxidation of 1-hexyl-3-methylimidazolium ($[HMIm]^+$) $[SnCl_3]^-$ ILs.[116,129] After repeating the reported air-free synthesis, ^{119}Sn NMR of neat $[HMIm][SnCl_3]$ displayed shifts of –128.9 and –138.9 ppm (Figure A4), consistent with Sn^{2+} nuclei and the previously reported values. Deliberate exposure of this ionic liquid to air produced a waxy material confirmed to be $[HMIm]_2[SnCl_6]$ by ^{1}H NMR[130] and ^{119}Sn NMR (Figure A5 and A6).[116,130] Whereas the previous study discussed the structure of the material in its crystalline form, we investigated whether oxidation involved an ionic liquid-to-ionic liquid transformation as well. Indeed, differential scanning calorimetry of neat $[HMIm]_2[SnCl_6]$ displayed a glass transition temperature (T_g) at –54.1 ˚C and a melting point (T_m) at 91.2 ˚C (Figure A7), qualifying this material as a bona fide IL, accessed through post-synthetic redox chemistry. Furthermore, the measured T_g is in good agreement with other chlorostannate ILs.[131]

Macroscopic changes accompanying the systematic modification of these perhalometalle ILs offered a convenient platform for studying the intermolecular interactions that arise from molecular composition and dictate bulk IL properties. In particular, we focused on the strong

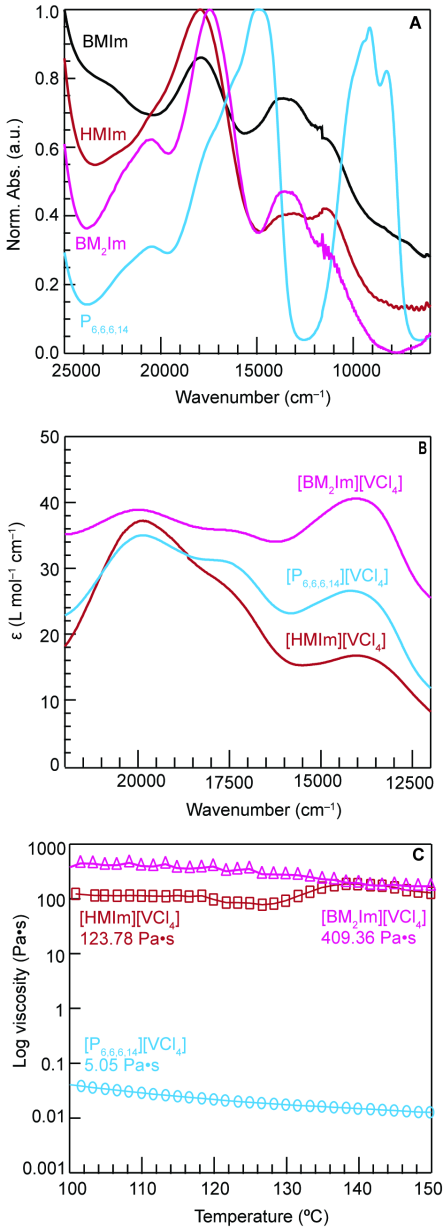

Figure 2.5: Absorption spectra and temperature-dependent viscosities of ionic liquids based on VCl_4^- with varying cation identities. (A) Absorption spectra of neat ILs. (B) Absorption spectra of IL prepared as 32-mM MeCN solutions (B). **(**C**)** Measurements were collected between 100˚C-150˚C at shear rate of 10 rad/s. 1-hexyl-3-methylimidazolium (HMIm) and 1-butyl-2metyl-3metylimidazolium (BM_2Im) were used for comparison to BMIm- and $P_{6,6,6,14}$-based VCl_4^- ionic liquids.

dependence of coloration and viscosity on the cation identity of the VCl_4^- ILs. Whereas

[BMIm][VCl_4] and [HMIm][VCl_4] appeared violet and purple, respectively, [$P_{6,6,6,14}$][VCl_4] was blue. As these colors arise from vanadium-based orbitals, any dependence of the non-coordinating cations was unexpected. UV-vis-NIR spectra of these related materials were collected on neat liquids kept air-free. Indeed, the absorption profiles are considerably different in both peak positions and overall shapes (Figure 2.5A). Motivated by reports that H-atoms at the 2-position of such imidazolium rings can interact with halides,[132] we hypothesized that weak H–Cl bonding sufficiently perturbed the V^{3+} ligand field to account for such marked spectral differences between the imidazolium and phosphonium derivatives. Therefore, to eliminate the possibility of secondary bonding interactions at the imidazolium 2-position, an analog was synthesized using 1-butyl-2,3-dimethylimidazolium ([BM_2Im]$^+$).

By removing such interactions, we expected the resulting spectrum to appear similar to the phosphonium IL. Instead, the spectrum of the resulting indigo [BM_2Im][VCl_4] material appears more similar to the other imidazolium derivatives (Figure 2.5A). To confirm that the cations were responsible for these spectral differences, we dissolved the ILs in acetonitrile, hypothesizing that dilution would eliminate cation-anion interactions through spatial separation. Indeed, UV-vis spectra of the diluted solutions shown in Figure 2.5B display absorption bands with similar peak energies and shapes, independent of cation identity, confirming that the cations, although intended as non-coordination ions, unexpectedly interact with the [VCl_4]$^-$ anions.

Altering the cation identity of the [VCl_4]$^-$ ILs also induced significant changes in viscosity that accompanied these changes in color. Whereas [$P_{6,6,6,14}$][VCl_4] appears as a free-flowing liquid at room temperature, the imidazolium derivatives exist as waxes until heated near 100 ºC. Figure 2.5C shows variable temperature viscosities, beginning at 100 ºC. These comparative data show that replacing [$P_{6,6,6,14}$]$^+$ with imidazolium cations increases viscosity by four orders of magnitude! Clearly, the intermolecular interactions causing changes in electronic absorption induces strong changes in the supramolecular ordering of the ILs. The similarity in viscosities between the [BM_2Im]$^+$ and [HMIm]$^+$ further suggests that such interactions do not involve H–Cl bonding at the imidazolium 2 position.

To explore whether perchlorometallate ILs exhibit such extreme cation dependencies in general, absorption spectra and variable temperature viscosities were measured for ILs prepared from [$CoCl_4$]$^{2-}$, [$NiCl_4$]$^{2-}$, and [$VOCl_4$]$^{2-}$ and a variety of cations. Figure A8 plots viscoelastic

data for $[CoCl_4]^{2-}$, with room temperature values ranging between 6.9–36 Pa·s, a typical range for ILs with different cations. Additionally, the UV-vis-NIR spectra show ligand field bands with similar peak positions and peak shapes. Likewise, the absorption profiles for $[NiCl_4]^{2-}$ ILs with different imidazolium or phosphonium cations appear nearly the same (Figure A9), and various derivatives of $[VOCl_4]^{2-}$ ILs display a similar range of room temperature viscosities (Figure A10). Whereas monoanionic $[VCl_4]^-$ requires only a single charge-balancing cation, however, these cobalt, nickel, and vanadyl materials require two per dianion, which we hypothesized might hinder inter-ion attractive interactions through steric crowding. By this reasoning, $[VCl_4]^-$ might ion-pair effectively with single imidazolium rings and not with bulky phosphonium cations, whereas the dianions might not pair well with any cation due to steric repulsion, leading to a lack of cation dependence. Viscosities of $[FeCl_4]^-$ ILs should, therefore, exhibit a cation dependence akin to $[VCl_4]^-$, but the data in Figure A11 show that viscosities differ by only 0.62 Pa·s between $[HMIm]^+$ and $[P_{6,6,6,14}]^+$ derivatives.

Although the cation dependence most likely results from differences in ion pairing, these results, therefore, suggest that the intermolecular interactions arise from chemistry specific to V^{3+}. The structure-induced absorption changes observed for the $[VCl_4]^-$ IL are reminiscent of high-pressure studies involving V^{3+}-doped MgO and Al_2O_3 that showed compression of metal-ligand bonds leading to increased ligand field interactions and concomitant blue shifts to absorption bands.[133] However, whereas uniform compression of all metal-ligand bonds produces simple energetic shifts in the absorption profile of metal ions, the data in Figure 2.5A show that the presence of imidazolium cations considerably distorts the shapes of the $[VCl_4]^-$ bands. The complex interplay of supramolecular interactions causing the severe cation-dependent optical and viscoelastic properties must therefore cause speciation of V^{3+} into anions that deviate from ideal tetrahedrally symmetric $[VCl_4]^-$ ions.

Given the strong covalency of V^{3+}-Cl^- bonds and the propensity of VCl_3 to form 2D covalent networks,[133] we hypothesize that the synthesis of $[VCl_4]^-$ ILs generates an equilibrium mixture of VCl_x^{y-} aggregates rather than individual $[VCl_4]^-$ monoanions. Figure 2.6 displays possible representations of the aggregates, including small vanadium dimers (Figure 2.6A) and larger oligomeric fragments of the 2D VCl_3 lattice with octahedral vanadium ions (Figure 2.6B). The size of the oligomers, we propose, depends on the ability of cations to break apart versus stabilize the large anionic clusters. On one hand, the steric bulk and electronegative alkyl groups

of $[P_{6,6,6,14}]^+$ might serve to fragment the oligomers, whereas electron-deficient imidazolium rings might better support the formation of VCl_x^{y-} aggregates and give rise to the higher viscosity. The presence of six-coordinate vanadium ions would also explain the blue-shifted absorption bands, as the higher coordination would increase the ligand field strength surrounding V^{3+}.

To investigate the plausibility of VCl_3 aggregation as an explanation for the observed cation dependence, we employed a suite of computational tools. Figure A12 shows computed electrostatic potential (ESP) maps of imidazolium rings with varying alkyl groups and $[P_{6,6,6,14}]^+$. Consistent with previous calculations,[134] and experimental reports on H- and halogen-bonding interactions of anions with imidazolium rings,[135,136] the ESP maps show pockets of electron deficiency at the imidazolium 2 position and ring center, whereas $[P_{6,6,6,14}]^+$ exhibits uniform high electron density. These results support the idea that imidazolium cations could better

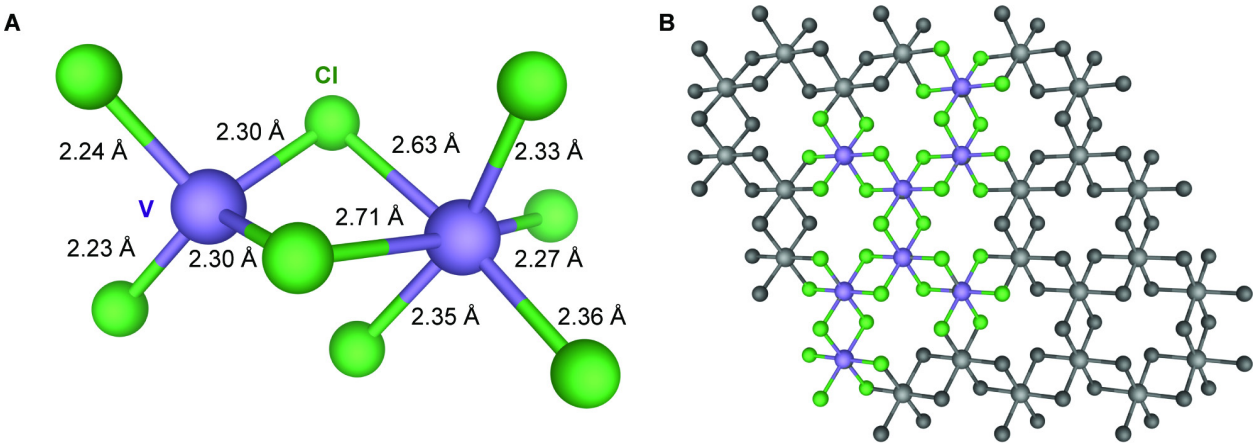

Figure 2.6: Representations of VCl_x^{y-} oligomers. (A) DFT Geometry-optimized $V_2Cl_8^{2-}$ "dimer". (B) Portion of the VCl_3 crystallographic structure.

stabilize VCl_x^{y-} aggregates electrostatically compared to $[P_{6,6,6,14}]^+$. Molecular dynamics simulations performed both with force-fields and *ab initio* methods have elucidated the presence of innumerable configurations of ion pairing in imidazolium-based ionic liquids that span a shallow potential energy surface for their respective chemistries, so we refrained from locating specific geometries of imidazolium-VCl_x^{y-} pairs.[137] Given the complex mixture of possible anion aggregates, Figure 2.7 plots TD-DFT-simulated absorption spectra in terms of simple limiting case scenarios. First, spectra were computed for VCl_6^{3-} and VCl_4^- with O_h and T_d symmetry, respectively. Clearly, the experimental traces of $[P_{6,6,6,14}][VCl_4]$ and $[BM_2Im][VCl_4]$ cannot be interpreted as a mixture of these two idealized species. Instead, we considered a hypothetical

$V_2Cl_8^{2-}$ dimer based on the hypothesis that the equilibrium mixture involves oligomers of six- and four-coordinate vanadium ions. Figure 2.6A displays the resulting geometry-optimized structure, with each vanadium center distorted considerably from either O_h and T_d symmetry and the idealized bond lengths of 2.461 Å and 2.245 Å, respectively. The corresponding simulated trace is shown in Figure 2.7. These simulations rule out certain well-defined vanadium species and suggest that the appearance of numerous absorption bands spanning a wide energy spectrum might be explained by the presence of low symmetry V^{3+} oligomers. Inspired by the apparent elongation of V-Cl bonds in the dimer model, we explored whether the experimental spectra could be understood from another simplified scenario of $[VCl_4]^-$ possessing systematically elongated V-Cl bonds resulting from $[VCl_4]^-$ anion-aggregate interactions. Figure 7 includes

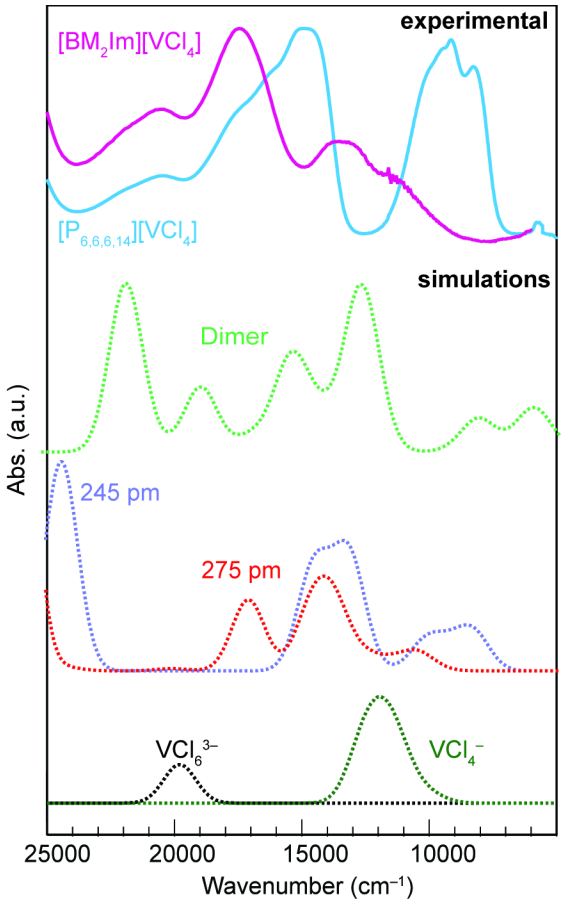

Figure 2.7: Comparison of experimental and simulated spectra of VCl_x^{y-} ILs. Experimental absorption spectra of $[BM_2Im][VCl_4]$ (pink) and $[P_{6,6,6,14}][VCl_4]$ (blue), Simulated spectra for the $V_2Cl_8^{2-}$ "dimer" (green), simulated spectra of VCl_4^- anions with single V-Cl bonds elongated to 245 (purple) and 275 ppm (red), simulated spectra of idealized VCl_6^{3-} and VCl_4^-.

simulated spectra for two possible structures where single V-Cl bonds were fixed at 275 pm and 245 pm, while the rest of the geometry was allowed to relax. Interestingly, the shorter V-Cl bond elongation of 245 pm shows better agreement with the $[P_{6,6,6,14}][VCl_4]$ experimental trace, whereas the 275 pm simulation agrees more closely with the $[BM_2Im][VCl_4]$ trace. These results are consistent with the hypothesis that imidazolium cations produce V^{3+} oligomers distorted farther from idealized tetrahedral symmetry.

Discussion

Scheme 2.3

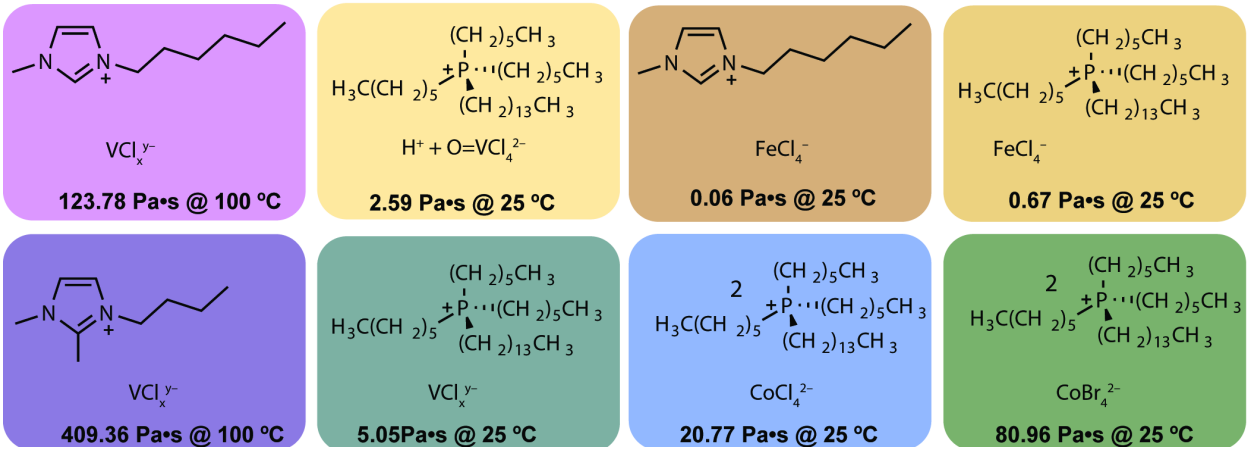

These results indicate that small changes to the coordination chemistry of ILs can yield remarkably different properties in new ILs. Scheme 2.3 summarizes key differences for some of the ILs reported here that arise in viscosity and color through systematic variation in cation and anion identities. Halide exchange to produce $[P_{6,6,6,14}]_2[CoBr_4]$ from $[P_{6,6,6,14}]_2[CoCl_4]$ caused viscosity to increase by 60.19 Pa·s, which exceeds rheological differences observed through systematic changes to conventional IL ions with more obvious structural differences. For example, the room temperature viscosity of [butylpyridinium][BF_4] differs from [1-propyl-3-methylimidazolium][BF_4] by only 0.0918 Pa·s, while switching the anion from [butylpyridinium][BF_4] to [butylpyridinium][NTf_2] causes a difference of only 0.1008 Pa·s.[138] Such a large difference from such a minor change to the overall IL composition is surprising. Although anion aggregation could account for higher viscosities and has been observed for $[CoCl_4]^{2-}$ and $[CoBr_4]^{2-}$,[139] the UV-vis spectra suggest the presence of just mononuclear species. Instead, we hypothesize that the greater molecular weight and polarizability of bromide ligands increases viscosity by enhancing halogen bonding and raising the activation energy for viscous

flow (E_a). Oxidation of $[P_{6,6,6,14}]_y[VCl_x^{y-}]$ to $[P_{6,6,6,14}]_2[VOCl_4]$ caused a far greater change to viscosity. Whereas elevated temperatures were required to perform rheological measurements on the former, room temperature viscosity of the vanadyl IL produced values of 14.22, 15.27, and 2.59 Pa·s for $[BM_2Im]$, [HMIm], and $[P_{6,6,6,14}]$, respectively.

These results help quantify the impact of intermolecular interactions on macroscopic properties. In the case of ligand exchange, enhanced secondary bonding interactions altered viscosity 10^2-10^3 times greater than changes between conventional ILs. Disrupting covalent bonding between VCl_x^{y-} oligomers through O-atom transfer, transformed an ionic liquid glass into a free-flowing liquid. Despite the power of this synthetic strategy, it bears few if any literature precedents. One of the few related examples involved anion exchange of halides loosely associated to IL polymers, rather than bound as ligands to metal centers in ILs.[140]

This work shows that conventional UV-vis spectroscopy enables deep insight into IL nanostructure that otherwise would be difficult to detect. UV-vis spectra have been used in isolated instances to confirm the presence of metal ions extracted into ionic liquids[141] and to understand conversion of metal-containing ionic liquids into coordination polymers,[142,143] whereas this work applies ligand-field analysis to confirm compositional purity and distinguish between mononuclear and polynuclear complexes. Although the solid-like nature of the VCl_4^--based ILs suggested the presence of strong intermolecular interactions, UV-vis allowed specific hypotheses about the nanostructure composition to be tested through comparison to TD-DFT simulated spectra. Perhalometallate aggregation has been detected in ILs based on Sn^{2+}, Al^{3+}, or Zn^{2+},[116,144,145] but could only be detected by subtle differences in Raman spectra. Here, iterative comparison between experimental and simulated spectra pointed to VCl_4^- forming oligomers stabilized by imidazolium ions through secondary bonding interactions.[58,146,147] Recent literature has shown the generation of coordination networks derived from ionic liquids,[148] but structural insight required an impressive suite of advanced characterization tools because the polymer

contained Zn^{2+} ions silent by UV-vis spectroscopy.[149] These results explore a range of forces spanning dispersion to covalent bonding, whereas typical reports of ionic liquids focus on manipulating just a few types of intermolecular interactions. Previous reports have shown that rigid supramolecular IL structures, *i.e.* those with stronger, localized interactions exhibit higher viscosities,[150] often showing anisotropic charge distributions within the ion components that cause high viscosities.[151] Such examples of localized and ordered charge pairs allows for enhanced intermolecular interactions through π-π interactions, hydrogen and halogen bonding, and Coulombic forces,[152] but predicting the magnitude of the impact of such interactions remains challenging. Table 2.1 shows how systematic changes to composition and types of intermolecular interactions impact viscosity and E_a. For example, as discussed above, altering halogen bond interactions in changing from $[P_{6,6,6,14}]_2[CoCl_4]$ to $[P_{6,6,6,14}]_2[CoBr_4]$ causes a minor increase of E_a by ~5 kJ/mol but large jump in viscosity by ~ 40 Pa·s. Altering electrostatic interactions, on the other hand, can be studied by comparing $[P_{6,6,6,14}]_2[CoCl_4]$ and $[P_{6,6,6,14}][FeCl_4]$; by changing from a dianion to a monoanion the electrostatic interactions

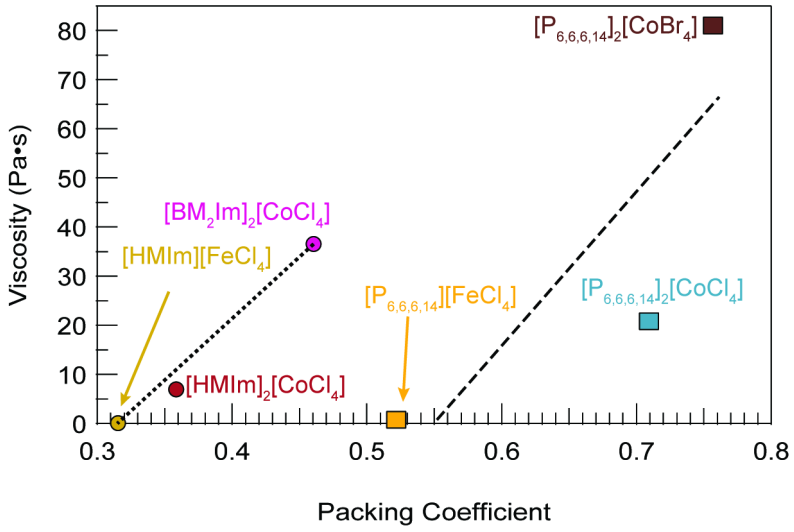

Figure 2.8: Correlation plot of IL viscosities versus packing coefficient (PC). Room temperature viscosities are reported with constant shear rates of 10 rad/s. Packing coefficients were determined from experimental molar volumes and simulated molecular volumes as detailed in the SI. The dotted and dashed lines denote linear best fits to the imidazolium- and phosphonium-based ILs, respectively.

between and the $[P_{6,6,6,14}]^+$ cation cause E_a to drop by 15 kJ/mol but viscosity drops by more than an order of magnitude. By systematically changing just the cation from a phosphonium to imidazolium, the effect of stronger intermolecular forces such as π-π interactions, hydrogen bonding, and van der Waals interactions becomes readily apparent. The viscosity of

$[HMIm]_2[CoCl_4]$ compared to $[BM_2Im]_2[CoCl_4]$ suggest the longer alkyl-chain length and altered dispersion interactions of the former decrease viscosity from ~37 to 7 Pa·s. Comparing $[P_{6,6,6,14}][FeCl_4]$ to $[HMIm][FeCl_4]$ increases viscosity by an order of magnitude, which we attribute to the enhanced halogen-binding interactions of imidazolium ions, corroborated by calculations presented here (Figure A10). In the extreme limit of intermolecular interactions, oxidation of $[P_{6,6,6,14}]_y[VCl_x^{y-}]$ to $[P_{6,6,6,14}]_2[VOCl_4]$ causes viscosity to decrease by 2.48 Pa·s, which we attribute to breaking the covalent VCl_x^{y-} networks. These results, therefore, permit changes intermolecular interactions to be correlated with approximate changes of viscosity, dispersion, halogen bonding, electrostatic, and covalent bonding giving rise to changes on the order of 10^0, 10^1, 10^1, and 10^4 Pa·s, respectively.

Lastly, Table 2.1 reveals an interesting relationship between IL rheological properties and intermolecular structure. As molecular species that produce bulk behavior, ILs have motivated intense research effort on understanding a physical connection between the intermolecular and

Table 2.1: Viscoelastic and volumetric properties of select ILs prepared here. E_a and PC denote activation energy to viscous flow and packing coefficient, respectively. Room temperature viscosities are reported.

Ionic Liquid	Viscosity (Pa·s)	E_a(kJ/mol)	Free Volume (L/mol)	PC
$[P_{6,6,6,14}]_2[CoCl_4]$	20.77	48.04	0.55	0.72
$[P_{6,6,6,14}]_2[CoBr_4]$	80.96	53.37	0.49	0.76
$[HMIm]_2[CoCl_4]$	6.91	48.67	0.48	0.36
$[BM_2Im]_2[CoCl_4]$	36.53	68.47	0.31	0.46
$[P_{6,6,6,14}][FeCl_4]$	0.670	33.38	0.47	0.52
$[HMIm][FeCl_4]$	0.058	20.68	0.35	0.32

macroscopic behavior. These studies have debated whether free volume,[138] molar volume,[153] or molecular volume[87] serve as the most accurate predictor of IL viscosity, ionic conductivity, and other properties. The data in Table 2.1 reveals, however, that while these volumetric parameters and E_a exhibit poor correlation with measured room temperature viscosities (Figures A21-A23), higher packing coefficients (PCs) correlate with increased viscosity among ILs with similar cations, i.e., imidazolium versus phosphonium ILs (Figure 2.8). Typically applied to understanding guest-host supramolecular chemistry, PC is defined as the ratio of molecular

volumes to molar volumes, such that dispersion interactions give rise to PC of ~0.55 and H-bonding and stronger interactions increase PC to 0.7 and beyond.[154] Here, we computed the molecular volumes from the electric field, the derivative of the electrostatic potential. This method has demonstrated utility in quantifying the volume and surface area of small polarized molecules,[155,156] while accounting for changes in ionic size due to formal positive and negative charges, as well as highly polarized covalent bonds (see Supporting Information). Whereas volumetric parameters fail to account for intermolecular interactions, PC treats them explicitly. While preliminary, PC appears to be a promising parameter to predict IL macroscopic behavior, such as IL viscosities and conductivities.

Conclusion

We demonstrate that ligand exchange and redox coordination chemistry serve as post-synthetic design strategies for ILs. By tailoring anion composition in a systematic fashion, these methods expand the diversity of ILs, in general, allowing greater control over structure-function relationships. For example, these results indicate that slight changes to perhalometallate coordination spheres result in surprisingly large changes to bulk rheological properties, suggesting secondary bonding interactions can dominate bulk IL interactions. By employing transition-metal-containing anions, these results also demonstrate that conventional UV-vis spectroscopy enables deep insight into the purity and speciation of the local molecular environment of ionic liquid ensembles. Complex supramolecular assemblies can be modeled by comparing experimental and simulated spectra. Systematic variation of IL compositions and intermolecular forces permits Coulomb interactions between ions, to be untangled from secondary halogen bonding between terminal chlorides and imidazolium π rings, and dispersion effects. Comparing the effect of these forces reveals the approximate orders of magnitude that each interaction exerts on bulk IL viscosity. Lastly, relating viscosity to packing coefficients shows promise as a novel approach to predicting bulk IL properties. Taken together, these results demonstrate that coordination chemistry provides powerful design and analytical techniques for investigating the fundamental connection of molecular properties to macroscopic behavior.

Chapter 3

Investigating the colloidal stability and solubility of nanosized metal-organic framework particles

Work in the chapter was published from LeRoy, M.A.; Perera, A.S.; Laminchhane, S.; Mapile, A.N.; Khaliq, F. Kadota, K.; Zhang, X.; Ha, S.; Fisher, R.; Wu, D.; Risko, C.; Brozek, C.K., *Chem. Mater.*, **2024**, *36*, 8, 3673-3682 https://doi.org/10.1021/acs.chemmater.3c03191.

Colloidal nanoparticles have reshaped materials science by combining solution processability with size-dependent behavior. Due to their large surface-to-volume ratios, colloidal nanoparticles are defined by their surface chemistry for both practical and fundamental considerations: colloidal stability,[157] particle self-assembly,[158,159] interfacial electrochemical phenomena,[160] surface plasmon resonances, photophysical dynamics, heterogeneous reactivity, and interparticle energy transfer[161] represent just a few of the fundamental areas governed by nanoparticle surfaces. Careful tuning of surface composition is also key to many practical goals: solution processibility, interfacing nanocrystal into composite materials,[162] and achieving environmental stability and biocompatibility.[163] Given that this research derives from a relatively small subset of materials—namely metals and conventional semiconductors, such as metal

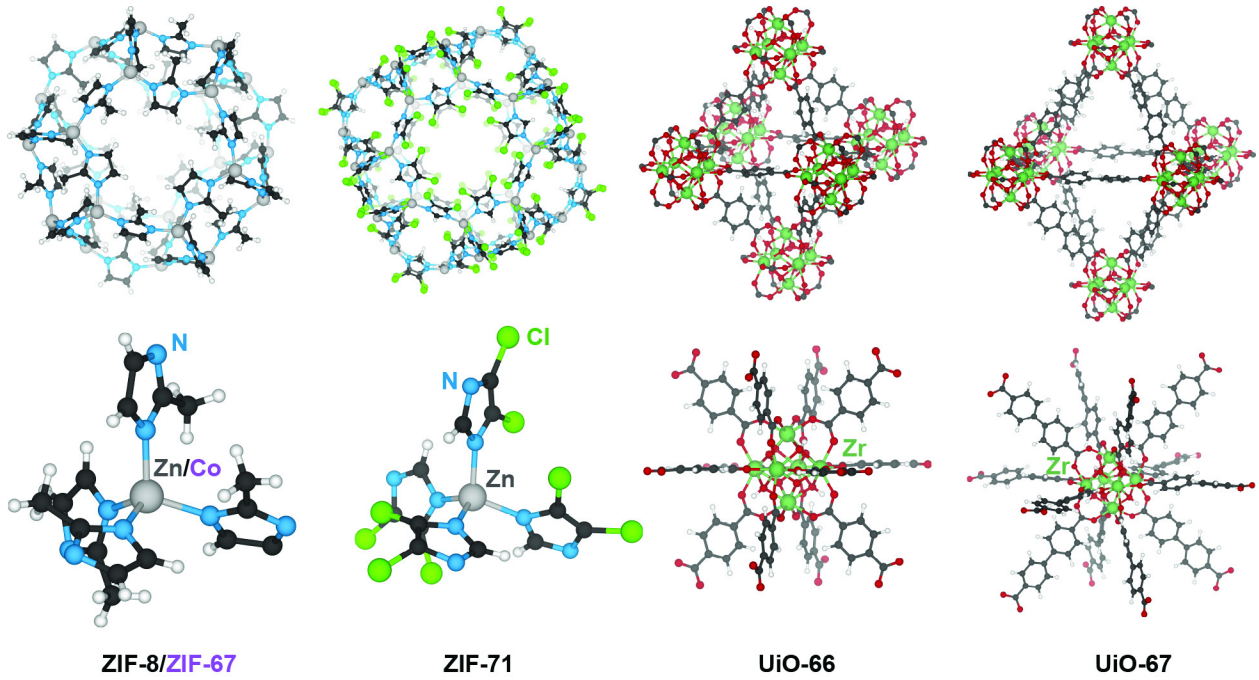

Fig. 3.1. Crystallographic images of the metal-organic framework materials investigated by solubility measurements, with representative pore apertures (top) and corresponding metal-ion environment (bottom) highlighted.

chalcogenides—a major outstanding goal is to prepare other classes of nanomaterials with intrinsically distinct behavior.

Metal-organic frameworks (MOFs) have been targeted for a wide range of fundamental questions and practical applications due to their porosity and wide synthetic tunability. Recent studies indicate their practical implementation in membrane-based applications requires the preparation of MOFs as nanoparticles rather than as bulk powder,[164,165] in part to enable control over particle size and morphology, and to enhance their biocompatibility[166] and solution processability.[167] Few MOFs have been prepared as nanoparticles, however. In the scarce existing synthetic methods, "modulators", rather than the typical surfactant ligands found in the quantum dot literature, direct the size of MOF nanoparticles (nanoMOFs).[42] Unlike surfactant ligands, evidence suggests that modulators only rarely incorporate onto the exterior or interior surfaces.[168–170] Instead, as described by the "seesaw" model reported previously, modulators influence particle sizes by affecting the metal-linker binding and linker deprotonation equilibria.[42,43] With this predictive model, we recently demonstrated a nanoparticle synthesis of the conductive MOF Fe(1,2,3-triazolate)$_2$ with diameter sizes controllable to just 6 nm—the smallest nanoMOFs to-date.[169] Size-dependent optical and charge-transport behavior emerged from this new class of semiconductor nanocrystals distinct from traditional quantum dots. Remarkably, despite the lack of surfactant additives and the absence of incorporated modulator, the particles exhibited indefinite colloidal stability in DMF under anaerobic conditions. Bare particles of nonporous[171] and porous[166,172] inorganic materials have been stabilized through electrostatic repulsion between large surface charge, in accordance with Derjaguin-Landau-Verwey-Overbeek (DLVO) theory.[173–175] Porous inorganic particles have also been stabilized through non-DLVO-type forces such as through favorable solvent interactions at the nanoparticle external surfaces.[176,177] Unlike these examples, nanoMOFs possess organic constituents with the potential for favorable solvent interactions at both the interior and exterior surfaces, akin to polymers and other soluble macromolecules. In fact, such solvent-linker interactions may resemble those responsible for the stabilization of nonporous nanoparticles coated with organic capping ligands.[178] From an applications perspective, the ability to functionalize nanoMOFs into polymer matrices will be impacted by the surface interactions underpinning this unexpected colloidal stability.[179–182] These fundamental and technological questions therefore motivate a

need to understand the structure and composition of nanoMOF surfaces and the nature of their interfacial interactions.

Here, we report the week-long colloidal stability of common nanoMOFs (**Fig. 3.1**) in the absence of conventional surface ligands. Rather than electrostatic repulsion from surface charges or steric repulsion from surface ligands, colloidal stability appears to arise from interactions between solvent and the particles. We find that the maximum amount of nanoMOFs that may be suspended (particle solubility) correlates with the solubility of the native MOF linker and the ability of solvent to access interior particle surfaces. While altering the metal ion identity leaves particle solubility unchanged, altering linker identity changes particle solubility to correlate with the linker solubility. Furthermore, calorimetry measurements indicate the immersion enthalpies of nanoMOFs resemble the solvation enthalpies of the constituent linkers and that these energies are independent of particle size. Atomistic molecular dynamics (MD) simulations reveal that solvents best at dissolving nanoMOFs are those that pack densely into the pores and interact with the linkers. Taken together, these results provide a foundation for predicting the best solvents for preparing colloidally stable nanoMOFs. On a fundamental level, these results open opportunities for exploring a fundamentally distinct type of material interface that includes both exterior and interior surfaces, where guest molecules access both and strongly influence colloidal behavior.

Experimental Section

Materials

All chemicals were used as purchased unless otherwise stated. Zinc(II) nitrate hexahydrate (99%, metal basis, crystalline, Thermo Fisher Scientific), 2-methylimidzole (99%, Acros Organics), zinc(II) acetate dihydrate (crystalline, Baker Analyzed, J.T. Baker), 4,5-dichloroimidazole (98% Beantown Chemical), benzimidazole (Aldrich), titanium(IV) butoxide (TCI Chemicals), 1,4- benzenedicarboxylic acid (terephthalic acid), biphenyl-4,4′-dicarboxylic acid (Chem Scene LLC), benzoic acid (JT Baker), copper(II) nitrate trihydrate (99%, Acros Organics), 1H-1,2,3-triazole (98%, TCI), zirconium(IV) chloride (99.5%, Strem Chemicals), zinc(II) acetate dihydrate (JT Baker), 2,5-dihydroxyterephthalic acid (98% TCI Chemicals), hydrochloric acid (certified ACS Plus, Fisher Chemical), tetrabutylammonium chloride (98% TCI Chemicals), tetrabutylammonium nitrate (98% TCI Chemicals), tetrabutylammonium hexafluorophosphate (98% TCI Chemicals), potassium hexafluorophosphate (> 95% TCI Chemicals), cobalt(II) nitrate (anhydrous, Baker Analyzed, J.T. Baker), MeOH (certified ACS, Fisher Chemical), ethanol (200

Proof, anhydrous meets UPS specs, Decon Labs Inc.), *N,N*-dimethylformamide (certified ACS, Fisher Chemical), and MilliQ Water 18.2 $M\Omega cm^{-1}$.

Synthesis of $CuTA_2$ nanoparticles

In a 20 mL scintillation vial, 0.059 g of $Cu(NO3)2 \cdot 6H2O$ was dissolved in 2 mL of DMF. To this solution was added 42.6 µL of 1H-1,2,3-triazole. The vial was capped and heated at 100°C for 2 h with stirring, followed by centrifugation and washing with DMF three times.

Synthesis of MIL-125 nanoparticles

A two-neck round bottom flask fitted with a reflux condenser and gas adapter was charged with terephthalic acid (0.352 g, 2.12 mmol) and cycled under dynamic vacuum and N_2 before being put under a steady flow of N_2. Dry DMF (5 mL) was added, then allowed to stir at 110 ºC for 30 min. After complete dissolution of the linker, 1.5 mL MeOH, benzoic acid (1.18g, 10.6 mmol), and 5-µL of DI water were added, and the solution was stirred under reflux for an additional 30 min. Ti(IV) butoxide (0.42 mL, 1.23 mmol) was then added and the reaction was stirred vigorously at 110 ºC under reflux for 14 h. The particles were then washed with cold DMF, and then MeOH three times.

Synthesis of 26-nm MOF-74 nanoparticles

5 mL of a 0.25-M solution of $Zn(OAc_2) \cdot 2H_2O$ (2.29 g, 5 mmol) in EtOH:DMF (1:1), was added to a scintillation vial and stirred. 5 mL of a 0.1-M 2,5-dihydroxyterephalic acid (0.99g, 2 mmol) was injected via syringe at a rate of 1 mL/min. After 24 h, the reaction was stopped by centrifugation and washing three with MeOH.

Synthesis of UiO-66/67 nanoparticles

A three-neck round bottom flask fitted with a reflux condenser and gas adapter was charged with terephthalic acid or biphenyl-4,4′-dicarboxylic acid (2.12 mmol) and cycled under dynamic vacuum and N_2 before being put under a steady flow of N_2. DMF (5 mL) was added, then allowed to stir at 110 ºC for 30 min. After complete dissolution of the linker, and 5 µL of DI water were added. Zr(IV) chloride (1.00 g, 1.23 mmol) was then added and the reaction was stirred vigorously at 110 ºC under reflux for 2 h. The particles are then centrifuged, and then washed with MeOH three times.

Synthesis of ZIF-8 nanoparticles

ZIF-8 nanoparticles (nanoZIF-8) were synthesized following literature procedure.[183] In general, to synthesize 36-nm nanoZIF-8, zinc nitrate hexahydrate (2.00 g, 6.72 mmol) in 136 mL

of MeOH, was poured into a 2-methylimidazole solution (2.76 g, 33.6 mmol) in 136 mL of MeOH stirring at 500 rpm and left to react for 1 h. The resulting nanoparticles were centrifuged and washed three times with MeOH by sonication and centrifugation. The particles were then dried at 100 ˚C under vacuum for 24 h. To achieve different sizes, the ratio of Zn:2Mim:MeOH was adjusted by a scale of 1:*x*:1000 with *x* = 2, 3, and 5 equivalents for large, medium, and small sizes of nanoZIF-8, respectively. SEM images of nanoZIF-8 are shown in **Figure B1**.

Synthesis of ZIF-71 nanoparticles

35-nm: Zinc acetate dihydrate $Zn(OAc_2)\cdot 2H_2O$ (0.11 g, 0.6 mmol) in 5 mL of DMF was combined with 4,5-dichloroimidazole (dcIm, 0.27 g, 2 mmol) in 5 mL of MeOH stirring at 500 rpm. The solution immediately turned a milky pink and was left to react for 45 min. The resulting solution was centrifuged and washed three times with MeOH.

54-nm: $Zn(OAc_2)\cdot 2H_2O$ (0.037 g, 0.2 mmol) in 5 mL of DMF was combined with dcIm (0.11 g, 0.8 mmol) in 10 mL of MeOH stirring at 500 rpm. The solution immediately turned a milky pink and was left to react for 30 min and left static at room temperature for 24 h. The resulting solution was centrifuged and washed three times with MeOH.

83-nm: $Zn(OAc_2)\cdot 2H_2O$ (0.037 g, 0.20 mmol) in 5 mL of DMF was combined with dcIm (0.11 g, 0.80 mmol) in 10 mL of MeOH stirring at 500 rpm. A 1-M HCl (2 μL, 0.00008 mmol) solution was added to the reaction and immediately removed from stirring and left static at room temperature for 24 h. The resulting solution was centrifuged and washed three times with MeOH.

SEM images of nanoZIF-71 are shown in **Figure B1**.

Synthesis of ZIF-11 particles

In general, to synthesize ZIF-11, a solution of $Zn(OAc_2)\cdot 2H_2O$ (0.100 g, 0.455 mmol) and 5 mL NH_4OH (5-M) were added to 5.3 mL of toluene. This solution was poured into a benzimidazole solution (0.120 g, 1.02 mmol) in 50 mL of MeOH stirring at 500 rpm and left to react for 3 h. The resulting nanoparticles were centrifuged and washed three times with MeOH by sonication and centrifugation. The resulting particles were then dried at 100 ˚C under vacuum.

Powder X-Ray Diffraction

Sample crystallinity was verified by powder X-Ray diffraction (PXRD) with a Bruker D2 Phaser benchtop diffractometer. Using the PXRD, Scherrer analysis was conducted to analyze crystallite size of the nanoMOFs and are shown in **Figure B2-B8**.

Dynamic Light Scattering (DLS) and Zeta Potential Measurements

DLS and zeta potential measurements were performed using a Zetasizer Nano from Malvern Panalytical. For the DLS experiments, three measurements were conducted per sample, and for the zeta potential, five measurements were conducted per sample. Before each measurement the sample was sonicated for ten minutes to break up any aggregates that had potentially formed.

Solubility Measurements

All samples were prepared by adding excess nanoMOF or linker to 500 μL or 1 mL of solvent respectively to create a saturated solution. The resulting mixture was then sonicated and allowed to settle for 24 h until the solid and liquid phases reached equilibrium. All solubility measurements were conducted on the supernatant.

To determine the linker solubility in each solvent, 1 mL of supernatant was transferred into a pre- weighed vial and heated under vacuum at 50 ˚C until only the solid residue remained. This procedure was done to prevent 2-methylimidazole from subliming. The mass of the vial was then weighed to determine the residual mass of the solid. This process was repeated three times to give an average value and standard deviation.

The nanoMOF solubility was determined by thermogravimetric analysis using a (TGA Q500), for each sample 20 μL of solution was added to pre-weighed aluminum TGA pan. The sample was then heated to 10 ˚C below the boiling point of the solvent to avoid bumping, starting from room temperature at 10 ˚C/min, then held isothermally for 15 minutes while being maintained under constant N_2 flow. The solubility of the nanoMOF was then determined from the residual mass of the TGA curve **Figure B13**. This process was repeated three times to give an average value and standard deviation.

Solubility after Addition of excess solvent or linker

All sample solubility values were measured as stated above with the following modification: To study the impact of extra solvent, an additional 500 μL was added to a saturated MeOH solution of 316-nm ZIF-8 particles followed by sonication and allowed to rest for 24 h to reach a new equilibrium. The excess linker measurement followed the same procedure except instead of solvent, 7 mg of 2-methylimidazole was added to solution.

Calculation of Nanoparticle Solubility

To determine MOF solubility in terms of moles of formula units per liter, based on a molecular weight for ZIF-8 of 227.58 g/mol:

$$mol\ ZIF8 = residual\ mass\ from\ TGA\ (g) \times\ 227.58 \frac{g}{mol} \tag{3.1}$$

$$Solubility\ \left(\frac{mol}{L}\right) = \frac{mol\ ZIF-8}{volume\ pipetted\ into\ pan} \tag{3.2}$$

To determine the solubility of ZIF-8 in terms of moles of particles per liter, a crystal density of 0.35 g/cm^3, molecular weight 227.58 g/mol, and a spherical diameter of 40 nm was assumed:

$$Volume\ = \frac{4\pi r^3}{3} \tag{3.3}$$

$$\begin{aligned} Particle\ M.W\ &= Volume * crystal\ density \times\ avogadro's\ number \\ &= \frac{g\ particles}{mol} \end{aligned} \tag{3.4}$$

$$mol\ particles\ = \frac{mass\ from\ TGA}{Particle\ molecular\ weight} \tag{3.5}$$

$$Solubility\ \left(\frac{mol\ particles}{L}\right) = \frac{mol\ particles}{volume\ pipetted\ for\ TGA} \tag{3.6}$$

Water Stability of ZIF-8 and ZIF-67

To test the water stability of nanoZIF-8 and ZIF-67 over the 24 hours needed to conduct the solubility measurements, a soaking test in Milli-Q water was conducted for 48 hours. All solutions were prepared in the same way as those for the solubility measurements. PXRDs were taken for both ZIF-8 and ZIF-67 as both 24 h and 48 h **Figure B10**.

Immersion Calorimetry

Near-room-temperature immersion calorimetry using a microcalorimeter (Setaram C80) was employed to determine the immersion enthalpies of three ZIF-8 samples with different particle

sizes in DMF, hexane, and MeOH. In each measurement,[184–187] a hand-pressed sample pellet (7-8 mg) was dropped into the organic solvent (8 mL) that was kept at 25 °C in the calorimetry chambers. The direct interactions between the organic solvent and the ZIF-8 sample introduced led to a calorimetric peak. Integration of the area under each calorimetric peak yielded the heat of immersion (kJ) for each ZIF-8 pellet. At least four successful measurements were performed on each sample to ensure reproducibility. The error bars were calculated as two standard deviations of the mean. The average molar formula of ZIF-8 was taken as $C_8H_{10}N_4Zn$ (227.6 g/mol). Immersion calorimetry results are shown in **Table B1**.

Molecular Dynamics Simulations

Initial Configurations

Atomistic molecular dynamics (MD) simulations were carried out to obtain an atomic-scale insights into the experimental observations with four different solvents. **(Figure B14)** A slab of periodic ZIF-8 was placed along the z-axis with the dimensions of 45×60 $Å^2$ and the solvent reservoirs were maintained around 80 Å totaling a box size of 60×60×205 $Å^3$. Structural information for ZIF-8 was extracted from crystal structures as reported in Park *et. Al*,[8] and the slab was created with VESTA.[9,10] The initial configurations of the solvent systems were generated using Packmol[11] with the aid of Molcontroller[12] and VMD[13]. All MD simulations were carried out using the GROMACS 2020 software package.[14] The OPLS-AA (optimized potential for liquid simulations – all atom)[15] forcefield parameters were obtained using the LigParGen server[16] and multiple literature sources with partial charges derived from the electrostatic potential (ESP) method.[17–23] (DFT) calculations were performed at ωB97XD/aug-cc-PVDZ level of theory using Gaussian 16 software suite.[24]

Simulation Details

MD simulations were carried out using Gromacs 2020 software package.[14] The systems were subject to energy minimization (maximum of 100000 steps) with the steepest descent method followed by 4 ns of NVT (constant number of molecules, volume, and temperature) ensemble equilibration for 500 ps with the velocity rescaling with a stochastic term with a 0.1 ps coupling constant[25] at 298.15 K. Subsequently, two NPT (constant number of molecules, pressure, and temperature) ensemble simulations were conducted: The first applied the Berendsen[26] barostat for 10 ns to stabilize the volume, while the second followed for 40 ns with Parrinello-Rahman[27] barostat with a time step of 2 fs and the same temperature controlling parameters as in the previous

step. For all ZIF-8/solvent systems, three-dimensional (xyz) periodic boundary conditions (PBC) with a compressibility of 4.5 x 10^5 bar^{-1} and a coupling time of 2.0 ps were applied with VdW and particle-mesh Ewald (PME)[28] cut-offs of 1.4 nm for long-range interactions. Bonds, angles, and dihedrals were constrained during simulations using LINear Constraint Solver (LINCS) algorithm.[29]

Results and Discussion

Recent literature has revealed preliminary evidence that nanoMOFs exhibit surprising colloidal stability in polar solvents and in the absence of common surfactant ligands,[42,169,188–190] whereas stability in nonpolar solvents requires careful surface functionalization.[190,191] To investigate the origin of this stability, nanoparticles of five common MOF materials were synthesized and studied for colloidal stability over a week-long period (**Fig. 3.2**). In certain cases (ZIF-8 and UiO-66) synthetic methods were previously reported,[183,192] while others ($CuTA_2$ and MIL-125) required novel methods in our labs. Dynamic light scattering measurements of MIL-125 ($Ti_8O_8(OH)_4$(terephthalate)$_6$), ZIF-8, UiO-66 ($Zr_6O_4(OH)_4$(terephthalate)$_6$), and $CuTA_2$ (Cu(1,2,3-triazolate)$_2$) nanoparticles suspended in MeOH exhibited constant hydrodynamic diameters (sizes) over 7 days indicating the nanoparticles avoid aggregation despite the absence of detectable surface ligands or surfactants (as determined by thermogravimetric analysis (TGA) and NMR) (**Figure 3.2a**). For comparison with ZIF-8, ZIF-71 (Zn(4,5-dichloroimidazolate)$_2$) nanoparticles were suspended in MeOH and investigated, but due to significantly larger hydrodynamic diameters, they were omitted from **Figure 3.2a** and included in **Figure B9**. In addition to hydrodynamic radii, zeta potentials of all nanoMOFs remained similarly consistent over a week (**Figure 3.2b**). The values of these zeta potentials reflect that surface potentials of ±20 mV and larger correlate with long-term colloidal stability of the particles in general.[193,194] We interpret the positive values of $CuTA_2$, ZIF-8, and UiO-66 to suggest open metal sites dominate their surfaces, while an excess of deprotonated linkers at the surface ZIF-71 and MIL-125 could explain their negative zeta potentials. The stability of these common nanoMOFs with sizes as small as 27 nm is unusual given that metal or conventional semiconductor nanocrystals of similar sizes would quickly aggregate without surface ligands.

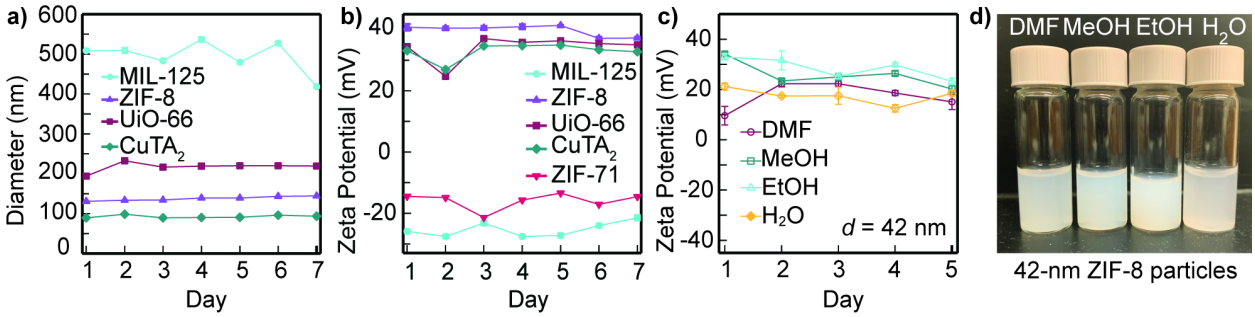

Fig. 3.2. Colloidal stability of nanoMOFs. (A) Nanoparticle hydrodynamic diameter and (B) surface zeta potential measurements of common nanoMOFs suspended in MeOH (1 mg/mL) over a 7-day period. Nanoparticle sizes by Scherrer analysis: 83, 87, 52, and 27 nm respecitivley for MIL-125, ZIF-8, UiO-66 and $CuTA_2$. (C) Zeta potential measurements of 42-nm crystalline sized nanoZIF-8 suspended in *N*-*N*-dimethylformamide (DMF), MeOH (MeOH), ethanol (EtOH), and H_2O. (D) Images of nanoZIF-8 colloids stabilized in DMF, MeOH, EtOH, and H_2O taken 1 month after initial suspension.

Among the investigated nanoMOFs, ZIF-8 nanoparticles exhibit colloidal stability in the widest range of solvents. However, as opposed to conventional quantum dot colloids that suspend in toluene or hexanes following post-synthetic treatment with surfactant molecules, ZIF-8 nanoparticles suspend indefinitely without deliberate surface functionalization in MeOH (MeOH), ethanol (EtOH), water (H_2O), and dimethylformamide (DMF), but not in hexanes, chloroform, or toluene without appropriate surfactant, as shown recently.[190] To probe whether this curious solvent stability depends on particle size, three sizes of ZIF-8 particles were synthesized and suspended in four different solvents and the corresponding zeta potentials were measured over time (**Figures 3.2c** and **B10**). Particle sizes reported here reflect the particle diameters determined from SEM images (**Figure B1**) as opposed to coherently scattering domain sizes determined by Scherrer analysis of PXRD reflections or hydrodynamic diameters in DMF from dynamic light scattering (DLS) (**Figure B18**). For all samples, SEM sizes were larger than the values determined by Scherrer and smaller than the hydrodynamic radii. This trend suggests that particle contain multiple crystallite domains. In all solvents, the nanoZIF-8 particles exhibit large and stable zeta potentials, as consistent with DLVO theory that colloids are stabilized by charged surface layers that repel neighboring particles and prevent aggregation.[195–197] Although ZIF-8 particles have been reported to degrade gradually in water, these studies also suggested a strong concentration dependence where more dilute solution degraded faster,[198] whereas the saturated solutions studied were prepared at far higher concentrations. Furthermore, these

nanoZIF-8 methanolic suspensions display visual stability for at least one-month storage, requiring only gentle sonication (~10 min.) to recover turbid suspensions (**Figure 3.2d**). In fact, particles remain stable in methanol with constant zeta potentials of 31 mV for over a year.

Interestingly, the only solvents to suspend ZIF-8 nanoparticles are also those that dissolve 2-methylimidazole (2MIm), the linker of ZIF-8. Although one would expect the solvent to etch the particles given the linker solubility, the particles sizes remain constant, as discussed above. Given that linker molecules dominate the atomic composition of ZIF-8, we further explored whether nanoZIF-8 stability arises from favorable interactions with solvent. Using standard solubility methods described in the Supporting Information, the solubility of 2MIm and nanoZIF-8 were measured in MeOH, EtOH, H_2O, and DMF. For the linker 2MIm, solubility was greatest in H_2O and lowest in DMF. By solubility, we refer to the maximum quantity of nanoparticles or linker suspended or dissolved at room temperature. **Figure 3.3a** plots the solubility of ZIF-8 formula units. These data reveal that particle solubility correlates directly with linker solubility and independent of particle size, given the similarity of solubility of three particle sizes when calculated per-formula-unit. To test whether these measurements truly probe a thermodynamically reversible dissolution-precipitation equilibrium, the solubility was redetermined after 500 μL of additional MeOH was added to methanolic solution of 316-nm ZIF-8 particles. Indeed, gravimetric concentration remained essentially unchanged from 0.4796 ± 0.1 mg/mL to 0.4160 ± 0.05 mg/mL. These results suggest precipitated particles redissolved as expected for a reversible process. To further probe the potential influence of linker-solvent

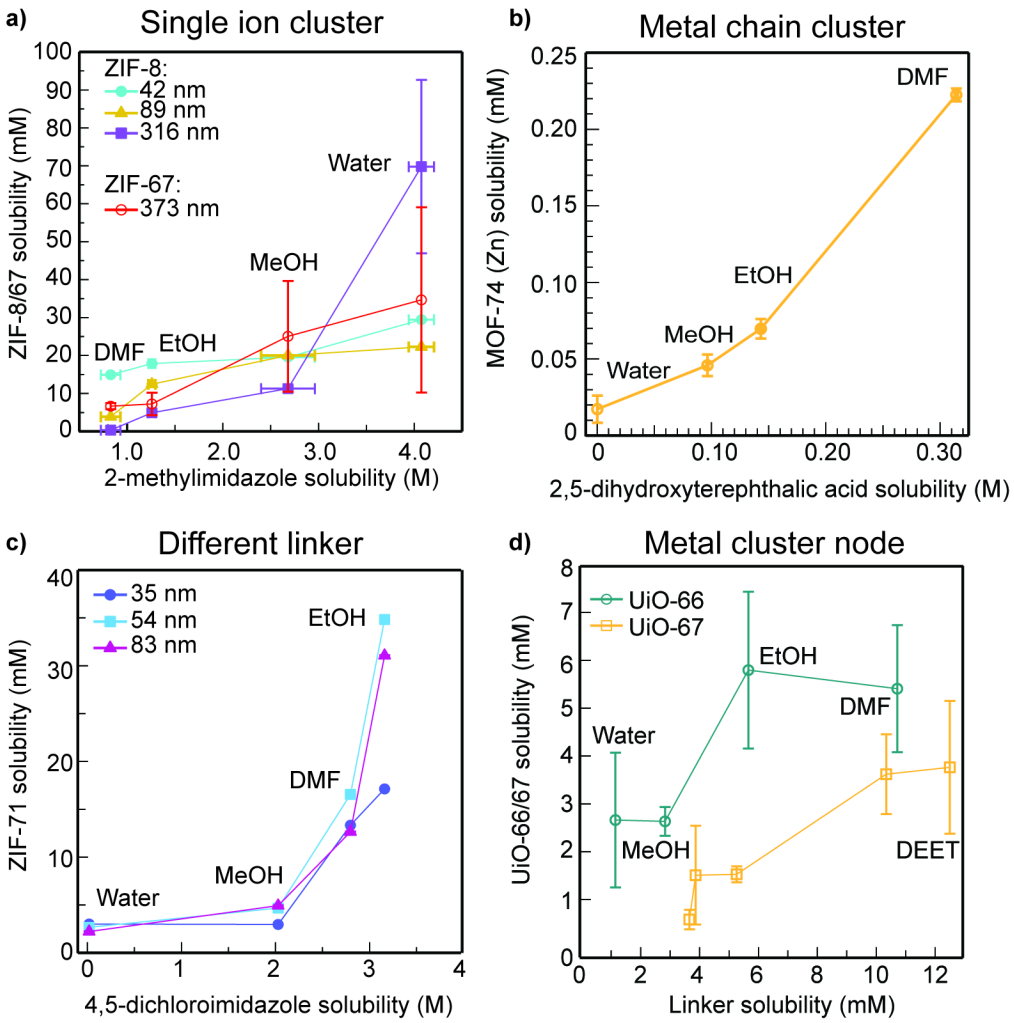

Fig. 3.3. Solvent-dependent linker and particle solubility. (a) Per-formula-unit solubility of ZIF-8 and ZIF-67 particles versus linker solubility. (b) Per-formula unit solubility of MOF-74 particles versus linker solubility. (c) Per-particle solubility of nanoZIF-71 versus linker solubility. (d) Per-formula-unit solubility of UiO-66 and UiO-67 particles versus linker solubility.

interactions on ZIF-8 nanoparticle solubility, a large excess of 2-mIm was added to a saturated solution of 316-nm particles, causing maximum solubility to raise from 1.294 ± 0.55 to 6.245 ± 0.8 mg/mL. Because solubility determination involves heating the particles well past the sublimation point of the linker, these results imply precipitated particles redissolve in the presence of excess linker.

To further investigate the origin of ZIF-8 nanoparticle solubility, we measured the solubility of related materials. **Figures 3.3a** includes the solubility of nanoZIF-67–a Co^{2+} rather than Zn^{2+} derivative of nanoZIF-8 (**Fig. 3.1**). These data show solubility sits within the uncertainty of the nanoZIF-8, suggesting solvent-metal site interactions have little impact on particle solubility. Because ZIF materials contain single-ion clusters, whereas most MOFs feature multinuclear nodes, we explored the solubility of 26-nm MOF-74 (Zn_2(2,5-dihydroxyterephthalate)) nanoparticles, which has 1-D metal-oxo chains. As shown in **Figure 3.3b**, the particles were again most soluble in solvents that best dissolved the linker. To further explore the impact of linker identity on particle solubility, we tested the solubility of nanoZIF-71—a MOF similar to ZIF-8 but composed of a different linker, 4,5-dichloroimidazolate (dcIm). Due to the more polar nature of dcIm, the overall solubility trend differed from nanoZIF-8, but the dependence of particle solubility on linker solubility still held, as shown in **Figure 3.3c**. With dcIm being now the least soluble in water and the most soluble in ethanol, the solubility of nanoZIF-71 followed the same trend as nanoZIF-8. To explore whether this relationship between particle and linker solubility held for framework materials with discrete multinuclear metal clusters, we measured the solubility of UiO-66 ($Zr_6O_4OH_4$(1,4-benzenedicarboxylate)$_6$) (**Fig. 3.1**) particles and compared against the solubility of the constituent linkers, terephthalate. Indeed, the relationship holds for solvents that dissolve the linker, whereas hexanes, toluene, and other solvents that do not dissolve terephthalic acid also fail to dissolve UiO-66 nanoparticles. Interestingly, nanoMOF per-formula unit solubility falls in the range of mM for both ZIFs and UiO-66, although the solubility and crystal density of the latter (1.237 g/cm^3) are smaller. To further explore the impact of crystal density, linker identity, and pore size, an isoreticular MOF, UiO-67 ($Zr_6O_4OH_4$(biphenyl-4,4′-dicarboxylate)$_6$) (**Fig. 3.1**) was studied. **Figure 3.3d** shows that the particle solubility correlates with the solubility of biphenyl-4,4′-dicarboxylic acid and is slightly lower than UiO-66 nanoparticle solubility. The lower solubility and crystal density (0.8872 g/cm^3) of nanoUiO-67 suggest particle solubility increases when more solvent-linker interactions are available per formula unit. The ability of *N*,*N*-diethyl-*meta*-toluamide (DEET) to solvate nanoMOFs was also explored given its chemical similarity to DMF but larger size (ca. 10 Å). Interestingly, although DEET dissolves terephthalic acid, it fails to form stable suspensions of UiO-66 (pore sizes are ca. 7.5 Å and 12 Å), whereas it dissolves both biphenyl-4,4′-dicarboxylic acid and UiO-67 (pore sizes are ca. 12 Å and 16 Å). DEET also fails to form stable

suspensions of the smaller pore nanoMOFs of ZIF-8 (3.4 and 11.6 Å), ZIF-67 (3.4 and 11.6 Å), ZIF-71 (4.2 and 16.5 Å), or $Cu(TA)_2$ (4.86 Å). Because calculating molarity depends on assuming the crystal density of the nanoMOF, which might be altered by defects such as collapsed pores or missing constituents, all solubility values for the aforementioned were also plotted simply in g/L units in **Fig. B14**, revealing the same qualitative correlations.

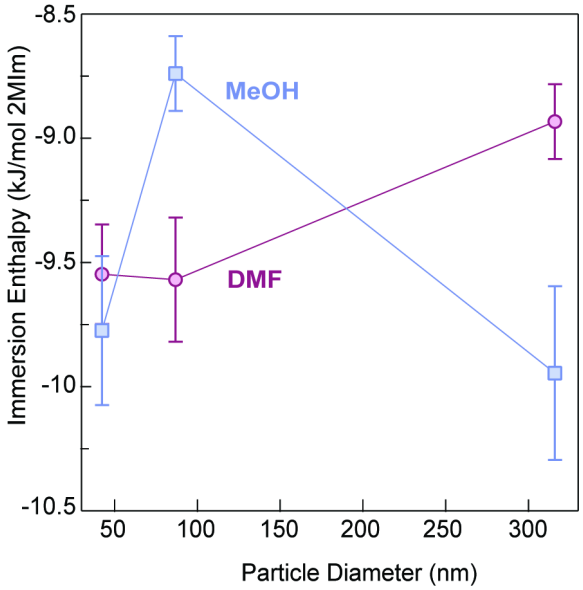

Fig. 3.4. Immersion enthalpies of ZIF-8 particles calculated per mole of 2MIm sites in MeOH or DMF versus particle diameter.

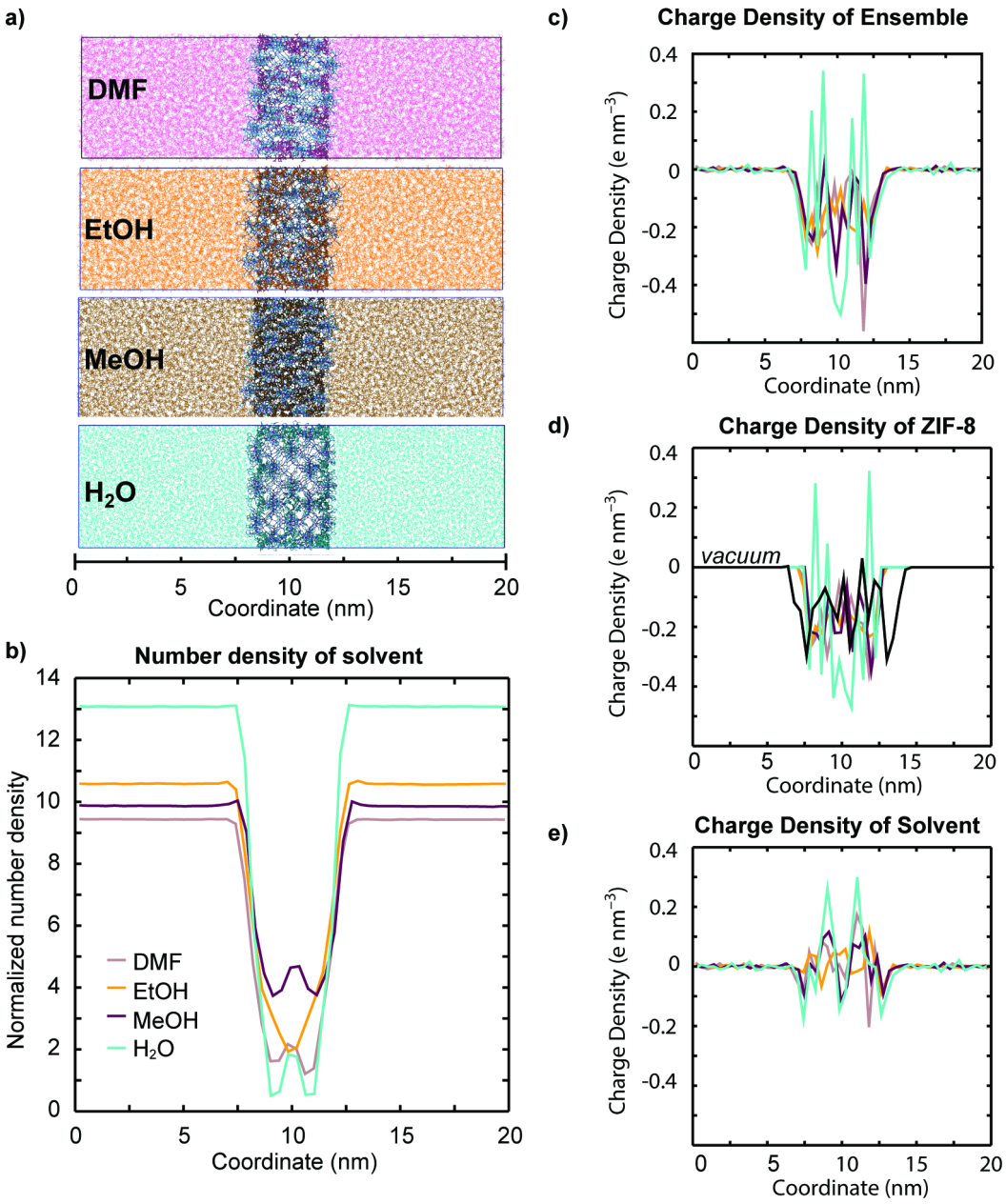

Fig. 3.5. a) A structural overview of the four different ZIF-8/solvent systems and supporting **b)** number and charge density plots of **c)** whole system, **d)** ZIF-8 slab, **e)** solvents. Number density and charge density values on y-axes represent the number of molecules and sum of partial charges respectively, per 4 (Å) wide slices along the z-axis.

Whereas nanoMOFs generally suspend only in polar solvents, industrial processing of colloidal nanocrystals requires nonpolar suspensions.[199] Therefore, to demonstrate the ability to predict nanoMOF colloidal stability from linker solubility and to achieve nonpolar dispersions of nanoMOFs, we identified ZIF-11 (Zn(benzimidazolate)$_2$) as a possible candidate due to the slight solubility of the linker in toluene (5.4 ±0.9 mM). Indeed, particles of ZIF-11 disperse in toluene

with a zeta potential of –5.3 mV. For insight into the energetics of solvent-nanoMOF interactions, immersion enthalpies of ZIF-8 nanoparticles of different sizes were measured in MeOH and DMF using near-room-temperature immersion calorimetry (**Table B1**). We report immersion enthalpies in terms of moles of 2MIm to explore the correlations discussed above between particle solubility and various solvent properties. Immersion of 86.7 nm ZIF-8 in DMF and MeOH gives enthalpies of –9.6 kJ/mol 2MIm and –8.8 kJ/mol 2MIm (**Fig. 3.4**), respectively, which resemble the molar solvation enthalpy of –12.5 ± 0.5 kJ/mol reported for 2-methylimidazole in MeOH at 298 K.[200] Put differently, the solvent environment around 2MIm in bulk solvent resembles the energetics of its environment in ZIF-8 immersed in solvent. These measurements comprise some of the only immersion enthalpies reported for nanocrystals. Immersion enthalpy does not change significantly between different sized particles, however, ranging between –9.0 kJ/mol 2MIm and –9.6 kJ/mol 2MIm of the largest and smallest particles of ZIF-8 suspended in DMF. When normalizing per mole of Zn sites, these values double to ~ –20 kJ/mol Zn, which is far lower than the ~ –80 kJ/mol Zn expected for solvation of Zn^{2+} ions in comparable solvents and the enthalpy of DMF to the open Zn^{2+} sites in MOF-5.[201] These relatively small enthalpies may also indicate that entropy plays an important role in nanoMOF colloidal stability, just as entropy dominates the solvation energetics of polymers, according to Flory-Huggins theory,[202] and the colloidal stability of proteins.[203,204] Nevertheless, the favorable enthalpy of immersion in polar solvents corroborates the existence of stabilizing solvent-based interactions that contribute to nanoZIF-8 colloidal stability. The size-independence of the values also suggests that particle solubility is not controlled exclusively by solvent interactions, for example with open metal sites, at the external particle surface. Instead, as with polymers, the energetics of MOF particle solubility depend on the sum-total of all solvent-constituent interactions. Due to the potential availability of both exterior and interior surface in MOF particles, solubility becomes most favorable when solvent gains access to the entire MOF particle, just as how polymer solubility increases when all monomer components are accessible to solvent. However, based on this interpretation, MOF particles may still be soluble if solvent only accesses exterior surfaces, but not as soluble as if interior components could be accessed as well.

For atomic-scale insight into these favorable solvent-MOF interactions, a computational model system was investigated that simulated bulk solvent interfaced with a well-defined “slab”

of ZIF-8, as detailed in **Figure B14**. Atomistic MD simulations were performed using DMF, EtOH, MeOH, and H_2O and analyzed in terms of the trajectories of the solvent into the slab, the packing density and geometric ordering of solvent within the MOF pores, and the interactions between solvent and ZIF-8 linkers. **Figure 3.5a** shows a snapshot of each system after a 50 ns simulation period. Visual inspection indicates that while solvent diffuses into ZIF-8 in all cases, packing density is lower for DMF and H_2O. **Figure 3.5b** depicts this result quantitatively as normalized (dividing by the density of the respective solvent) number density projected along the *z*-axis of the simulation box, showing H_2O and DMF to have the lowest densities within the ZIF-8 slab and MeOH the highest. With the exception of H_2O, this result suggests the solubility of ZIF-8 depends on the ability of solvent to densely pack inside the pores, which corroborates the solubility versus solvent density trend plotted in **Figure 3.5b**. The low packing density of H_2O is expected given its high polarity and the hydrophobic nature of ZIF-8 pores. Although H_2O intercalates the least, charge density analysis suggests it interacts the strongest with the MOF interior (**Figures 3.5c-3.5e**). A net-zero charge density arises from an isotropic distribution of molecules, as expected for a disordered system such as bulk solvent. The non-zero charge densities shown for the total solvent-ZIF-8 system (**Figure 3.5c**), only ZIF-8 (**Figure 3.5d**), and only solvent (**Figure 3.5e**) indicate that the presence of solvent inside ZIF-8 causes of net reordering of both the MOF and solvent within the pores. Interestingly, the charge density amplitudes are greatest for H_2O. This result suggests that the strong solvating strength of H_2O arises from enthalpically favorable interactions with 2MIm that also contribute to the high solubility of 2MIm in H_2O. Plotted differently as radial distribution distances of solvent with respect to the Zn or N atoms within ZIF-8, **Figure B15** reveals that solvent molecules order within the pores as clusters, seen as well-defined peaks and valleys. Regardless of solvent type, the radial distributions show solvent ordering closer to 2MIm than to the metal sites, further supporting experimental evidence of strong solvent-linker interactions.

For insight into how solvents interact differently with 2MIm, we inspected the dynamics of the 2MIm linkers over the course of the simulation. To explain the non-zero charge density of ZIF-8, we suspected solvent induced the "gate-opening" phenomena observed for ZIF-8 and other MOFs with linkers that freely rotate.[205–211] **Figure 3.6** plots the average angle change in the imidazole ring plane over the course of the simulation period.[212] While linker rotation dynamics are observed for all solvents, the presence of H_2O causes the clearest evidence of net ordering of 2MIm. This result explains the origin of non-zero charge density and provides a rationale for the high solubility of ZIF-8 particles in H_2O despite its low density within the pores.

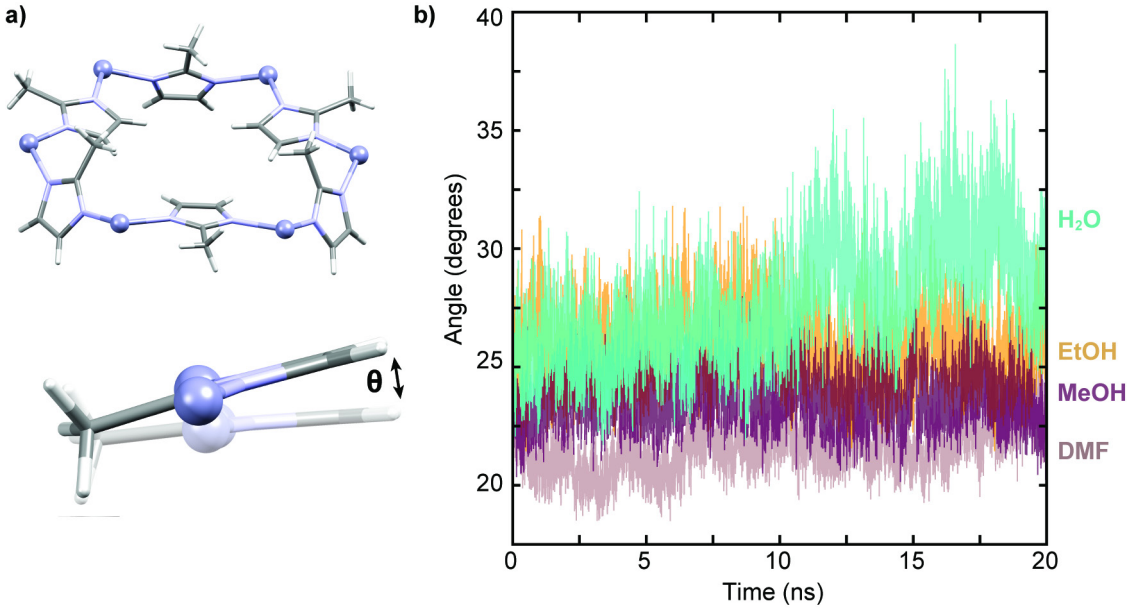

Fig. 3.6. Average angle (θ) in the imidazole ring plane to its initial geometrical position as a function of time. **a)** Three-dimensional structure of the aperture of the ZIF-8 molecular pore and angle (θ) between initial and current geometrical position. **b)** Change in angle with respect to time sampled over the last 20 ns of NPT simulation.

Conclusion

These combined experimental-computational results portray a mechanism of colloidal stability with nanoMOF particles that more closely resembles the solubility of large macromolecules, dictated by exothermic interactions between solvent and the MOF interiors and exteriors. Solubility measurements with varying particle size and composition and immersion calorimetry suggest the solvent-linker energetics dominate these favorable interactions. Although smaller particles have more exposed exterior surface sites, the independence of solubility from particle size suggests that solvent access to the entire particle, including the interior, dominates

overall solubility. These results also suggest a positive correlation between the solubility of MOF particles and the solubility of the constituent linker molecules, due to solvent-linker interactions dictating overall particle solubility. Atomistic MD simulations of ZIF-8 interfaced with various solvents suggest that solvents better at packing into the MOF pores lead to greater nanoMOF solubility, further improved by strong solvent-linker interactions. Because solvent can penetrate the interior cavities and interact with the external surfaces, these results challenge conventional notions of colloidal stability rooted in electrostatic repulsion and surface capping ligands, and concepts of solubility reserved for much smaller species. More broadly, these results will improve the solution processability of MOF materials into membranes and thin films for industrial applications.

Chapter IV

Future Directions

In this dissertation, the impact of intermolecular interactions on two classes of metal based soft materials has been discussed perhalometallate ILs and nanoMOFs by use of molecular chemistry. Both classes of materials are advantageous material for research due to their high synthetic tunability, unique structures, and varying intermolecular interactions. In Chapter II, we demonstrated that ILs can undergo post-synthetic modification through the use of ligand exchange and redox coordination chemistries. By choosing to focus on perhalometallate anions, the diversity of ILs can be expanded, allowing a greater fundamental understanding of structure-property relationships. This can be understood by inducing slight changes in the anion coordination sphere that significantly impacts the rheological properties of the material. This is due to changes in the secondary bonding interactions that occur between the cation and anion species. The use of transition-metal containing anions, allows for the use of UV-Vis spectroscopy as a unique tool for the determination of the ionic liquids purity, speciation, and local molecular environment. Furthermore, by selectively choosing cations and anions for IL compositions, we can also influence and understand the intermolecular interactions occurring between the two. This allows for a better understanding of how systematic changes in IL structure impacts parameters such as viscosity, and show how coordination chemistry can be an important tool designing ILs for specific design applications.

In Chapter III we focused on elucidating the mechanism of colloidal stability with nanoMOF particles by using a combination of experimental and computational experiments. By employing solubility measurements in conjunction with calorimetry, we are able to suggest that the energetics of solvent-linker interactions are favorable for stability. This is due to the solvent being able to interact with the interior and exterior of the MOF pores, which is akin, to that of large macromolecules such as polymers and proteins. The solubility data was able to show a size independence when comparing smaller to larger particles. One would assume that with the higher surface to volume ratio with decreasing size there would be a strong dependence for solubility. However, it appears that the ability of solvent to access all of the MOF surface, ie interior and exterior, is the main driving force for solubility and stability, which is in positive correlation with favorable solvent-linker interactions. This is further corroborated by Atomistic Molecular Dynamic simulations which imply that the ability of solvents to pack into the MOF

pores leads to greater nanoMOF solubility and strong-solvent linker interactions. These results overall showcase a unique view of colloidal nanoparticle solubility and stability. Furthermore, these results highlight an improved method for understanding solution processability of MOFs in membranes for applied applications.

Though both distinct types of soft materials, both have been incorporated into mixed-matrix membranes (MMMs) for use primarily in the field of gas separations. Gas separation through the use of membranes is an important field of research and highly industrially relevant, it's important to understand how to best improve this technology. Though much work has been done to study the interactions in MMMs as whole, it's still important to understand the interactions of the individual components. In this dissertation, the intermolecular interactions that give rise to macroscopic properties of both ionic liquids and nanoMOFs have been investigated. By varying the compositional structure of the ionic liquids we were able to see systematic changes in the rheological properties, and were able to determine the purity and composition through judicious use of perhalometallate based anions by use of UV-Vis spectroscopy. This combination also allowed for a more fundamental understanding of the intermolecular interactions that governed these macroscopic properties, as a sum and individual components. The work that investigated nanoMOF colloidal solubility and stability highlighted the importance of strong solvent-linker interactions as well as solvent accessibility to both the interior and exterior of the MOF crystal. By combining experimental and computational methods the understanding of solvent-linker interactions in nanoMOF solubility, showcases the fundamental understanding that can help improve solution state processability for nanoMOFs.

Though this work has shown how important intermolecular interactions play an important role in understanding soft materials macroscopic properties, work is still needed to be done to understand the interactions when these materials are used in composite materials. One of the most important challenges in MMM is strong interactions between materials to reduce voids in the membrane. By specific tailoring of the intermolecular interactions between MMM components, increased cohesion can be attained thus potentially improving membrane performance. A second challenge is to choose materials whose individual macroscopic properties when combined increase that of the overall material such as membrane stability and durability. A final challenge is to identify how to combine individual components in the ideal ratios to maximize membrane fabrication and industrialization. One method to improve the strength of the

interfacial interactions is to design materials that have favorable interactions. An example would be functionalizing an imidazolium based ionic liquid with a carboxylate, sulfate, or phosphate end group that could promote binding with the surface of a nanoMOF particle. The bonding interaction has the potential to bind with the open metal sites or linker located at the surface of the nanoparticle. The advantage of choosing to use an end group such as a carboxylate or phosphate is that they allow for the use of the molecular chemistry previously discussed to understand the changes in the intermolecular structure by monitoring potential differences in IR and UV-Vis and how they relate to changes in the macroscopic properties such as viscosity.

Though the previous methods have allowed for understanding of simple interfaces for both ionic liquids and nanoMOFs, the understanding of the interface for polymer nanocomposites (PNCs) has remained a challenge, especially as it relates to macroscopic properties. The complexity of understanding polymer nanocomposite interface is a result of the changes in the overall molecular motion of the polymer when compared to that of the neat polymer itself. The impact on molecular motion of the polymer nanocomposite material can be related to changes seen in the macroscopic properties of density, mechanical modulus, or glass-transition temperature (T_g).[213] As mentioned before one significant challenge of creating PNCs is in the dispersibility of the nanoparticle material in the polymer matrix. This challenge relates to the intermolecular interactions between polymer and nanoparticles at the molecular level. This specific challenge is further enhanced when factoring in the processing conditions used to form the final PNC material. The most common factor to consider is the solvent being used to cast the PNC which impacts the equilibrium states of the polymer and nanoparticle as they form the PNC.[214,215] Solvent identity plays an important role due to the differences in intermolecular interactions, casting methods, and overall processability for a desired PNC application.

In order to better understand the intermolecular interactions in PNCs we can turn to broadband dielectric spectroscopy (BDS) a laboratory technique that allows for the study of the relaxation dynamics ie molecular changes of both the neat polymer and PNCs over a broad frequency range (10^{-2} to 10^{-7} Hz) and with high accuracy.[216] An advantage of BDS is the ability to analyze multiple relaxation processes at the same temperature ie α- and β-relaxations, small sample amounts, and can be run over a wide temperature range.[217] Use of BDS allows for correlation with other techniques that probe both the relaxation dynamics and macroscopic mechanical properties of PNCs such as small-angle X-ray scattering (SAXS), dynamic light

scattering (DLS), dynamic mechanical analysis (DMA), differential scanning calorimetry (DSC), and rheological measurements.[218] By combining these techniques a more fundamental understanding of how intermolecular interactions in PNCs impact the macrostructural properties can be understood.

Considering our new knowledge of the importance of intermolecular interactions in both ionic liquids and nanoMOFs we aim to leverage that to better understand how to construct mixed-matrix membranes through controlled assembly of nanoparticles in a polymer matrix. Specifically, we have chosen to focus on moieties consisting of ionic liquids, oligomers, and polymers that are terminated by carboxylic acids as seen in Scheme 4.1. The hypothesis being

Scheme 4.1

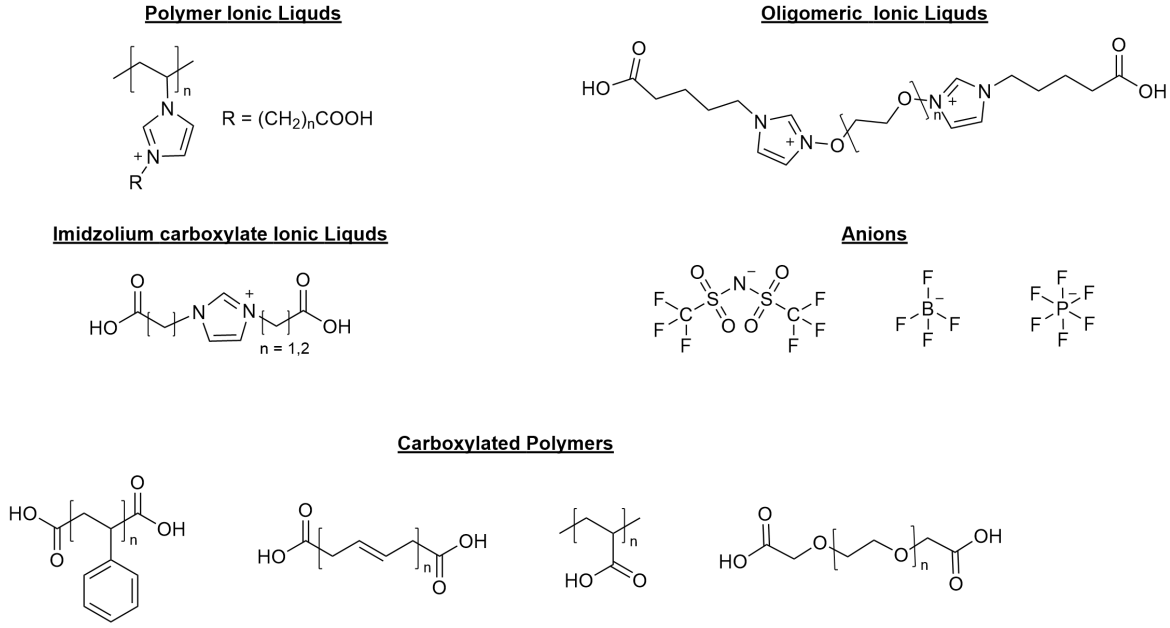

that having a carboxylic acid terminated species will allow for strong covalent binding of the carboxylate with the surface of a nanoparticle or the promotion of hydrogen bonding between species, whether that be polymer or surface linker. The use of carboxylic acid terminated capping ligands we also hypothesize, will aid in creating a homogeneous dispersion of nanoparticles within the polymer matrix, which will potentially allow for determination of the maximum number of binding sites at the surface for a given nanoparticle size. By understanding the binding environment, we can have precise control over how the nanoparticles self-assembly and can then measure how systematic changes in such as molecular weight in oligomers or polymers, changes in hydrogen bonding, or anion identity in ionic and polyionic liquids impacts the overall

composite material properties. Precise control of the materials properties is important when considering applications such as melt electrowriting, where 3D materials are made from continuous polymeric microfibers by the electrohydrodynamic effect.[219] Such precise control of the binding environment could be used to determine the impact of temperature on transition metal-based nanoparticles during the electrowriting process. Processing factors including solvent identity, additional filler, and loading percents can be used as metrics to determine ideal conditions. In combination with the techniques mentioned above, these ideal processing conditions could ideally be related back to our understanding of the intermolecular interactions that then give rise to macroscopic properties, and then selectively tuned for a given process or application. Moving forward using molecular chemistry as a diagnostic handle to understand intermolecular interactions can be added to the toolbox for better materials design and processing for a membrane based technologies.

APPENDIX A: SUPPLEMENTARY FOR CHAPTER 2

Experimental Methods

Synthesis

Imidazolium derivatives

[BMIm]$_2$[CoCl$_4$] (1). In a 10-mL Schlenk flask 260 mg (2 mmol) $CoCl_2$ and 700 mg (4 mmol) 1-butyl-3-methylimidazolium (BMIm) chloride were combined under an inert atmosphere. The reaction mixture was then heated at 115˚C for 2 hours with stirring. The resulting dark blue ionic liquid was stored under N_2.

Compounds **(2)** [BMIm]$_2$[NiCl$_4$], a dark blue liquid, **(3)** [BMIm]$_2$[CuCl$_4$], a light orange liquid, and **(4)** [BMIm]$_2$[MnCl$_4$], a pale yellow liquid, were prepared in a similar fashion. Compounds **(5)** [BMIm][CrCl$_4$], a dark purple liquid, and **(6)** [BMIm][FeCl$_4$], an orange liquid, were similarly synthesized but by using a 1:1 mixture of the precursors.

[HMIm]$_2$[CoCl$_4$] (7). In a 10-mL Schlenk flask 260 mg (2 mmol) $CoCl_2$ and 810.88 mg (4 mmol) 1-n-hexyl-3-methylimidazolium (HMIm) chloride were combined under inert an atmosphere. The reaction mixture was then heated at 115˚C for 2 hours with stirring. The resulting blue ionic liquid was stored under N_2.

Compounds **(8)** [HMIm]$_2$[NiCl$_4$], a dark blue liquid, and **(9)** [HMIm]$_2$[SnCl$_6$], a light-yellow liquid, were prepared in a similar fashion. Compounds **(10)** [HMIm][SnCl$_3$], a light yellow liquid, **(11)** [HMIm][VCl$_4$], a purple liquid, and **(12)** [HMIm][FeCl$_4$], an orange liquid, were also similarly synthesized but by using a 1:1 mixture of the precursors.

[BM$_2$Im]$_2$[CoCl$_4$] (13). In a 10-mL Schlenk flask 260 mg (2 mmol) $CoCl_2$ and 754.7 mg (4 mmol) 1-butyl-2,3-dimethylimidazolium (BM$_2$Im) chloride were combined under an inert atmosphere. The reaction mixture was then heated at 115˚C for 2 hours with stirring. The resulting blue ionic liquid was stored under N_2.

Compound **(14)** [BM$_2$Im]$_2$[NiCl$_4$], a blue liquid, was prepared in a similar fashion, whereas for compound **(15)** [BM$_2$Im][VCl$_4$], a indigo liquid, a 1:1 mixture of the precursors was used.

Phosphonium derivatives

[P$_{6,6,6,14}$]$_2$[CoCl$_4$] (16). In a 10-mL Schlenk flask 260 mg (2 mmol) $CoCl_2$ and 2.07 g (4 mmol) trihexyltetradecylphosphonium (P$_{6,6,6,14}$) chloride were combined under an inert atmosphere. The reaction mixture was then heated at 115˚C for 2 hours with stirring. The resulting blue ionic liquid was stored under N_2.

Compound **(17)** $[P_{6,6,6,14}]_2[NiCl_4]$, a blue liquid, was prepared in a similar fashion, whereas compounds **(18)** $[P_{6,6,6,14}][VCl_4]$, a blue liquid, **(19)** $[P_{6,6,6,14}][VBr_4]$, a green liquid, **(20)** $[P_{6,6,6,14}]_2[CoBr_4]$, a blue liquid, and **(21)** $[P_{6,6,6,14}]FeCl_4]$, an orange liquid, were prepared by combing precurors in a 1:1 mixture.

Ligand Exchange of Perchlorocobaltate to Perbromocobaltate ILs

Ligand exchange was performed by first chilling 2.7 g (2.32 mmol) of **(16)** $[P_{6,6,6,14}]_2[CoCl_4]$ at 4 ˚C and 21.5 mL of 1M HBr to –20 ˚C for 4 hours. The HBr solution was added dropwise to the ionic liquid causing a gradual color change from dark blue to dark red. After addition was completed the solution was stirred for 12 hours with intermediate shaking. The mixture was left to settle forming two layers. The final ionic liquid was extracted from the organic layer with methylene chloride and dried under vacuum.

Oxidation of Vanadium ILs

Vanadium ILs **(11)** [HMIm][VCl_4], **(15)** [BM_2Im][VCl_4], and **(18)** $[P_{6,6,6,14}][VCl_4]$ were oxidized by exposure to air and followed by heating at 150˚C for two days. Solution-phase ILs in MeCN were oxidized by exposure to air.

TD-DFT Calculations

The ORCA 4.0.1.2 software package[220] was used for simulating electronic absorption spectra. The all-electron def2-TZVPD basis sets Gaussian basis sets developed by the Ahlrichs group were employed in all calculations,[221,222] with the def2/J auxiliary basis.[223] Calculations were performed at the spin-unrestricted level using the M06-L functional.[224] Geometry optimizations began from crystallographically determined structures. In calculations that fixed individual V-Cl bond distances, all other atomic positions were optimized. Otherwise, all positions were optimized. All calculations were performed with and without the Control of the Conductor-like Polarizable Continuum Model (CPCM)[225] using ethanol to model the ionic liquid medium, as has been performed.[226]

Packing Coefficient Calculations

Density functional theory (DFT) was used to perform geometry optimizations for the individual cations and anions of interest, as implemented in Gaussian09.[227] Optimizations were performed using a RMS force convergence of 10^{-5} hartree, except for trihexyltetradecylphosphonium which required 10^{-4} hartree convergence due to the shallow potential energy surface for the *n*-aliphatic

carbon chains. The electronic wavefunction was obtained with the GGA functional M06L, [224,228] with a triple zeta basis set, including polarization and diffuse functions on all atoms.[229]

Packing coefficients were calculated using the formulation previously presented by Mecozzi *et al,*[154] where the packing coefficient is taken as the ratio between the sum of the anion and cation molecular volumes (V_m) and the occupied volume (V_O).

$$Packing\ Coeffient = \frac{\sum V_m}{V_O}$$

The occupied volume is derived using the experimental concentration. The molecular volumes are calculated using a previously reported method,[155,156] using the electrostatic potential returned by DFT.

Supplementary Figures:

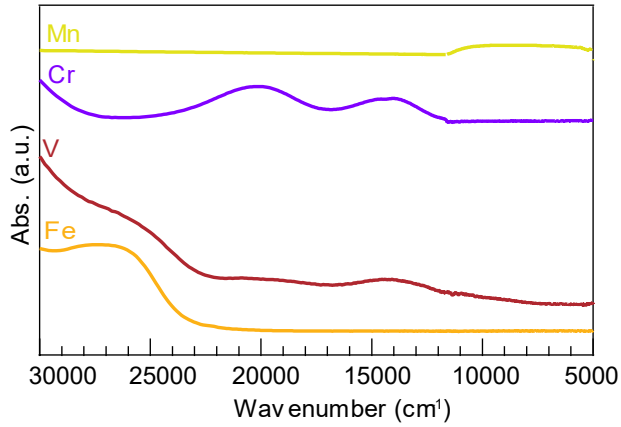

Figure A1. Electronic absorption spectra of neat ionic liquids 1-butyl-3-methylmidazolium (BMIm) perchlorometallate ions. $[BMIm]_2[MnCl_4]$ in yellow, $[BMIm]_2[CrCl_4]$ in purple, and $[BMIm]_2[VOCl_4]$ in red, and $[BMIm][FeCl_4]$ in orange.

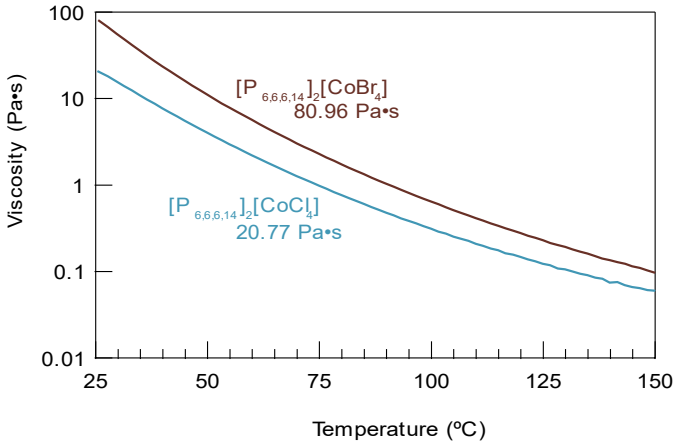

Figure A2. Temperature-dependent viscosities of $[CoCl_4]^{2-}$ and $[CoBr_4]^{2-}$ ionic liquids. Measurements collected between 25-200˚C at 10 rad/s.

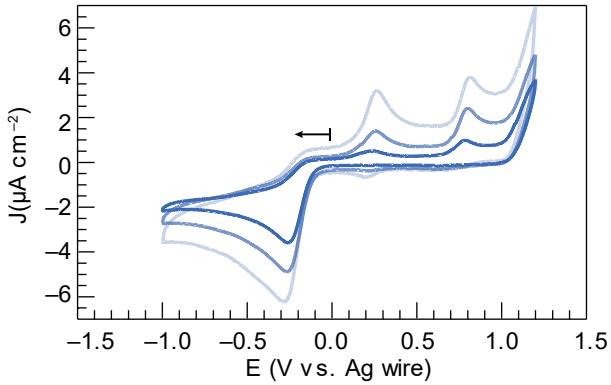

Figure A3. Cyclic voltammogram traces of mM $[P_{6,6,6,14}][VCl_4]$ in acetonitrile. Scan rates were conducted at 25, 50 and 100 mV/s with a Pt wire W.E. and Ag wire C.E/R.E.

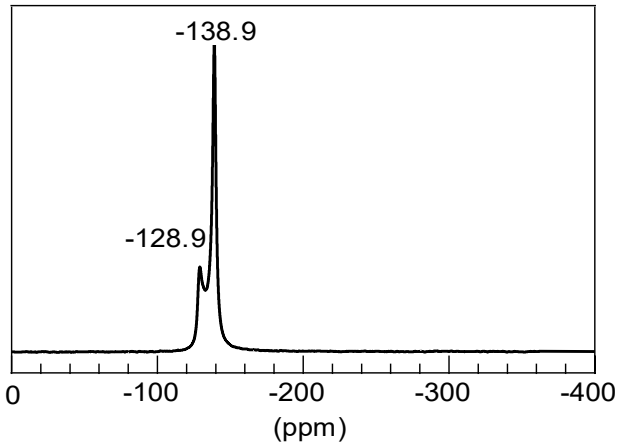

Figure A4. ^{119}Sn NMR spectrum of neat Sn^{2+}-based $[HMIm][SnCl_3]$ ionic liquid.

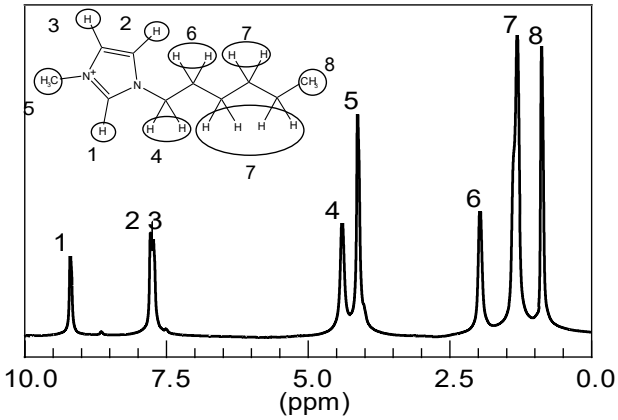

Figure A5. ^{1}H NMR spectrum of neat Sn^{4+}-based $[HMIm]_2[SnCl_6]$ with assigned peaks.

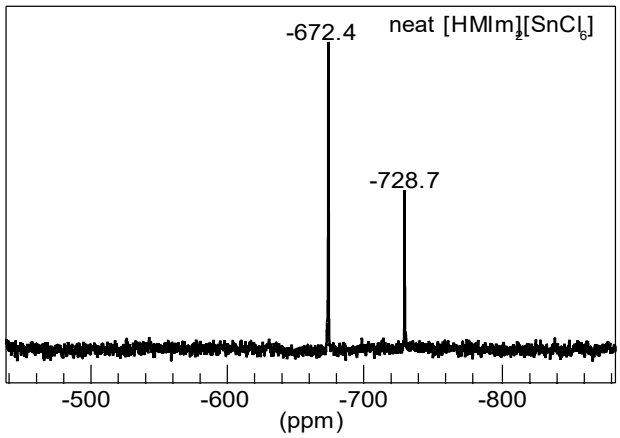

Figure A6. ^{119}Sn NMR spectrum of Sn^{4+}-based $[HMIm]_2[SnCl_6]$.

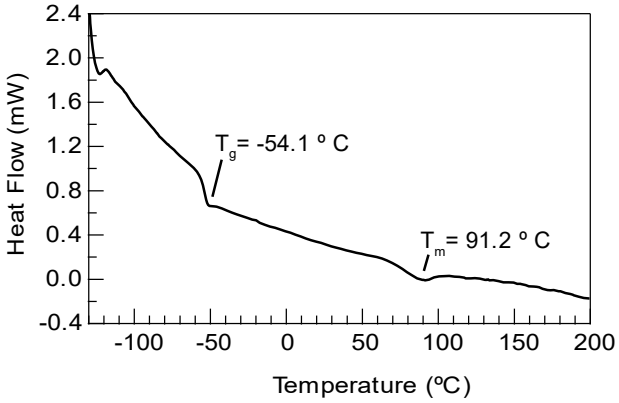

Figure A7. Differential scanning calorimetry scan (heating only, plotted with exothermic values as positive) of neat Sn^{4+}-based $[HMIm]_2[SnCl_6]$ ionic liquid. Data shows a T_g at –54.1 °C and T_m at 91.2 °C.

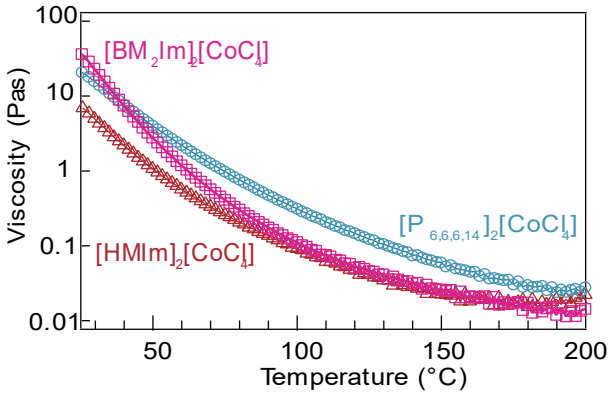

Figure A8: Temperature-dependent viscosities of $[CoCl_4]^{2-}$ ionic liquids containing imidazolium (HMIm or BM_2Im) or $P_{6,6,6,14}$ cations. Measurements were collected between 25˚C-200˚C at shear rate of 10 rad/s.

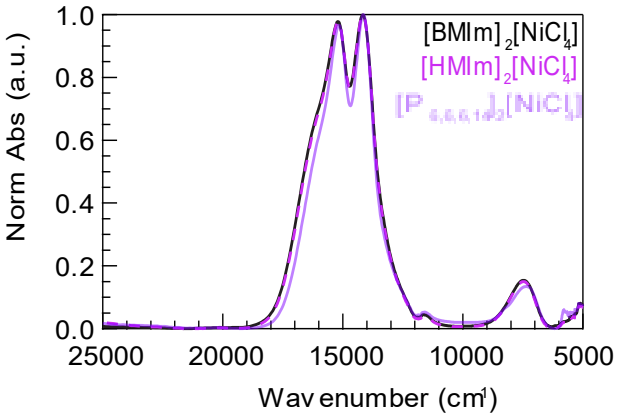

Figure A9: Absorption spectra of $[NiCl_4]^{2-}$ ionic liquids with different imidazolium (HMIm and BMIm) and $P_{6,6,6,14}$ cations.

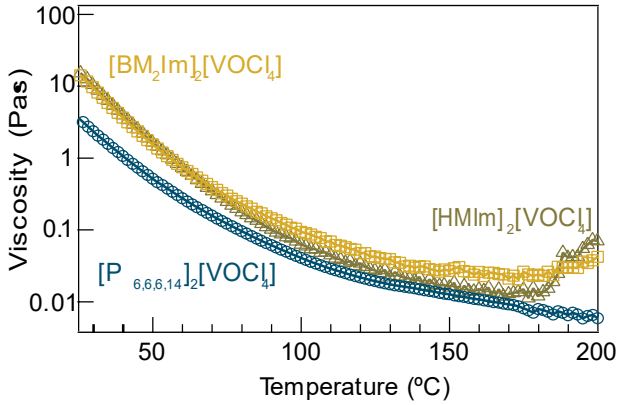

Figure A10: Temperature-dependent viscosities of $[VOCl_4]^{2-}$ ionic liquids containing imidazolium (HMIm or BM_2Im) or $P_{6,6,6,14}$ cations. Measurements were collected between 25˚C-200˚C at shear rate of 10 rad/s.

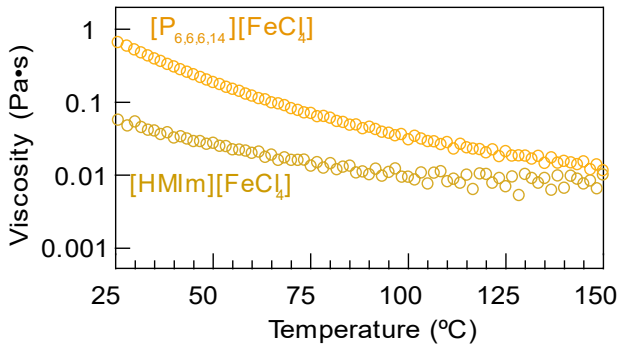

Figure A11. Temperature dependent viscosities of $[FeCl_4]^-$ ionic liquids containing HMIm and $P_{6,6,6,14}$ cations. Measurements collected between 25-150˚C at 10 rad/s.

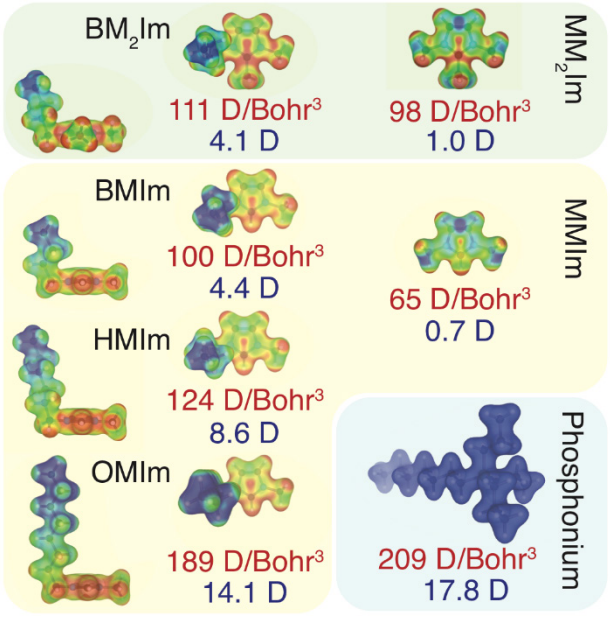

Figure A12. Electrostatic potential maps constructed for each cation explored herein and the methyl substituted imidazolium rings to illustrate the impact of electron-withdrawing alkyl substituents. Polarizabilities are presented in red text and dipole moments are shown in blue; within the maps, red corresponds to regions of relative positivity and blue, negativity. Increasing the length of the alky chain enhances the molecular polarizability and net dipole moment; it can also be seen that the proton in the 2 position increases in electrophilicity as the alkyl chain increases in length and that the 2,3-dimethyl variants show their greatest electrophilicity on the face of the ring, rather than in front.

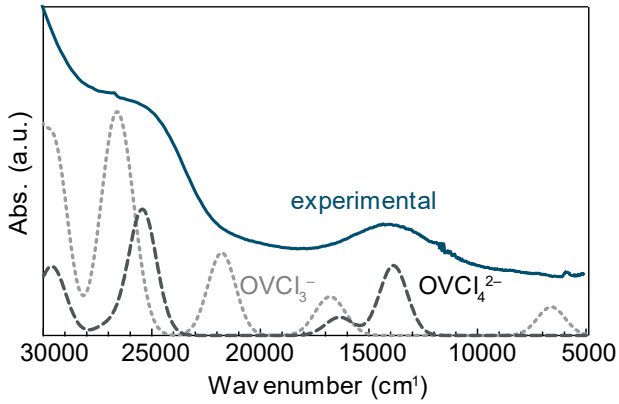

Figure A13. TD-DFT of simulated $[OVCl_3]^-$ and $[OVCl_4]^{2-}$ anions and experimental $[OVCl_x]^{y-}$ spectra.

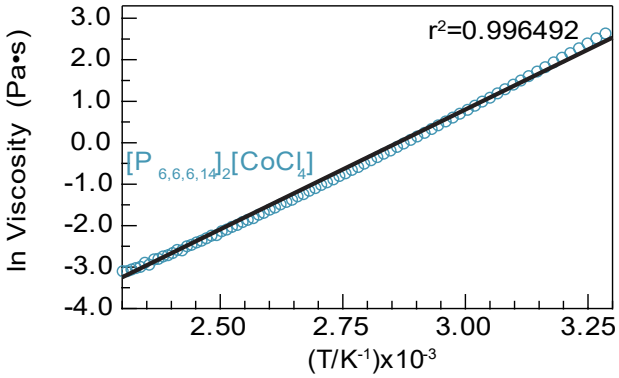

Figure A14. Arrhenius plot of $[P_{6,6,6,14}]_2[CoCl_4]$ (r^2=0.996).

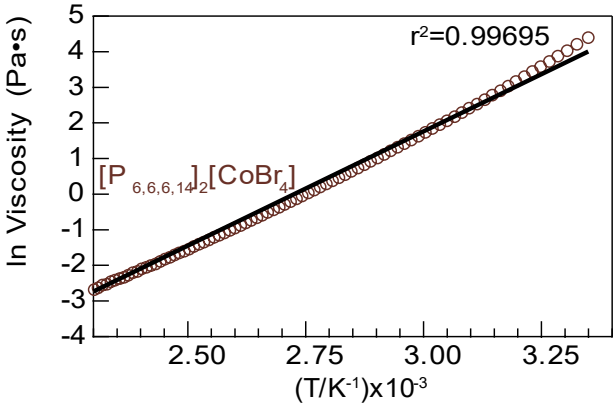

Figure A15. Arrhenius plot of $[P_{6,6,6,14}]_2[CoBr_4]$ (r^2=0.996).

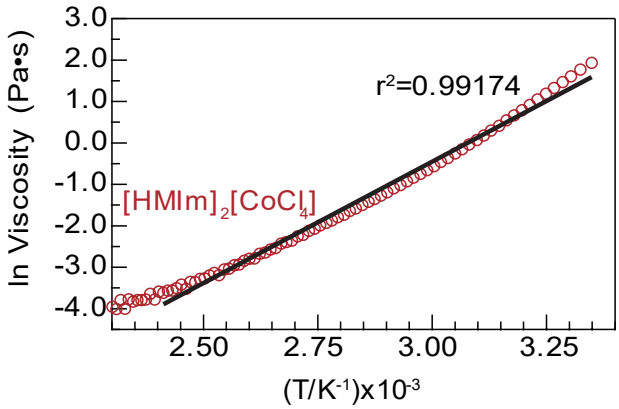

Figure A16. Arrhenius plot of $[HMIm]_2[CoCl_4]$ (r^2=0.991).

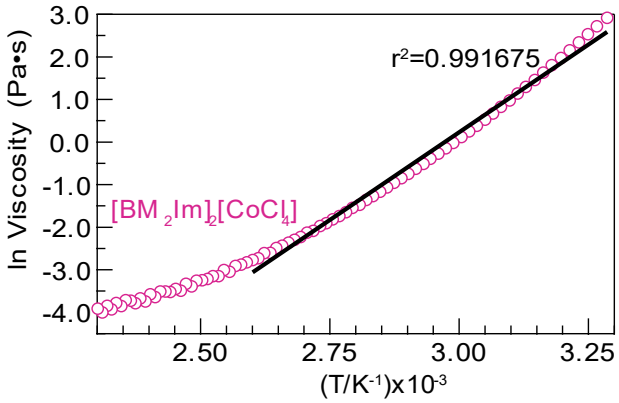

Figure A17. Arrhenius plot of $[BM_2Im]_2[CoCl_4]$ (r^2=0.991).

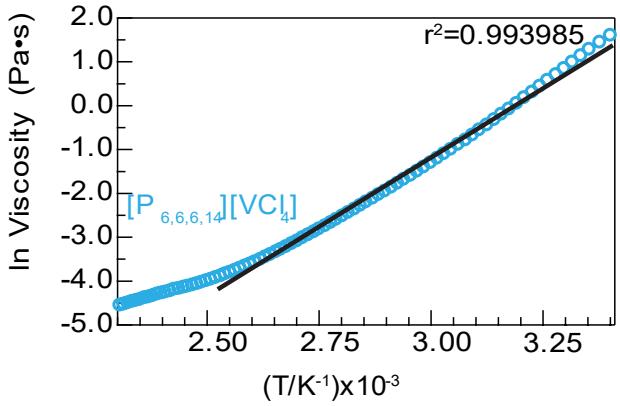

Figure A18. Arrhenius plot of $[P_{6,6,6,14}][VCl_4]$ (r^2=0.993).

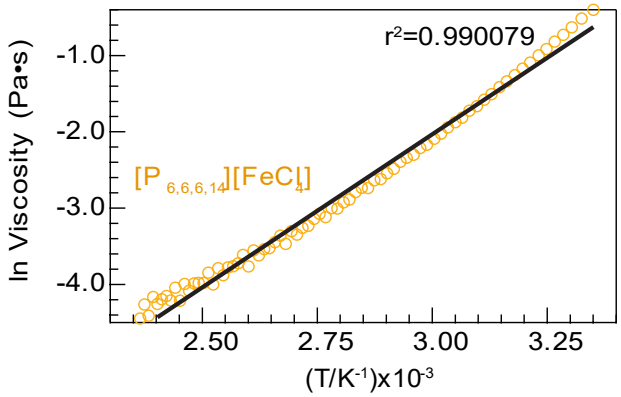

Figure A19. Arrhenius plot of $[P_{6,6,6,14}][FeCl_4]$ (r^2=0.990).

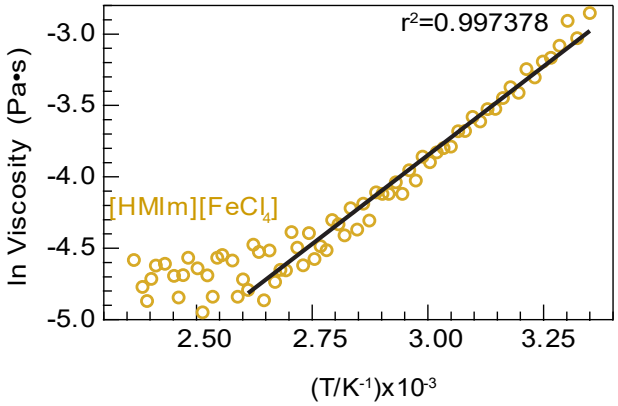

Figure A20. Arrhenius plot of [HMIm][$FeCl_4$] (r^2=0.997).

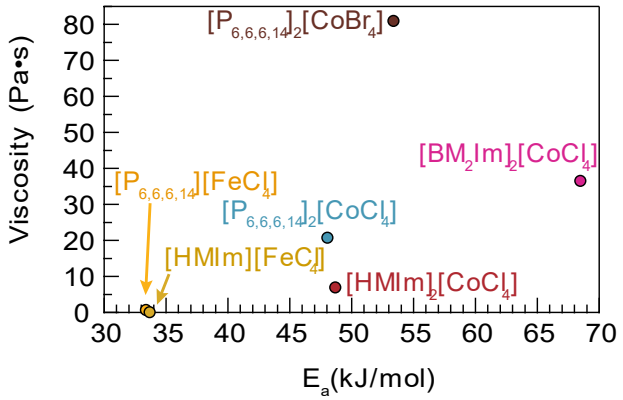

Figure A21. Viscosity vs E_a plot for various ILs reported here.

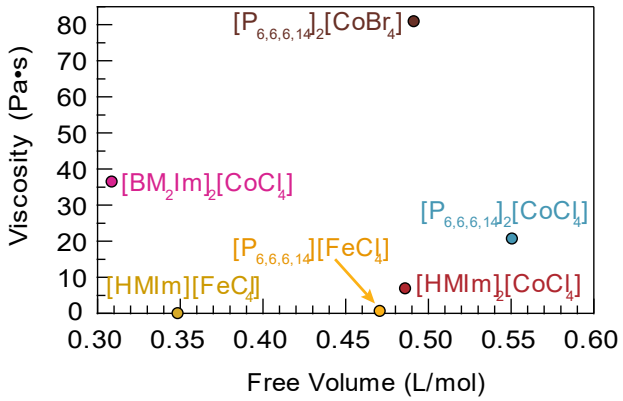

Figure A22. Viscosity vs Free volume plot for various ILs reported here.

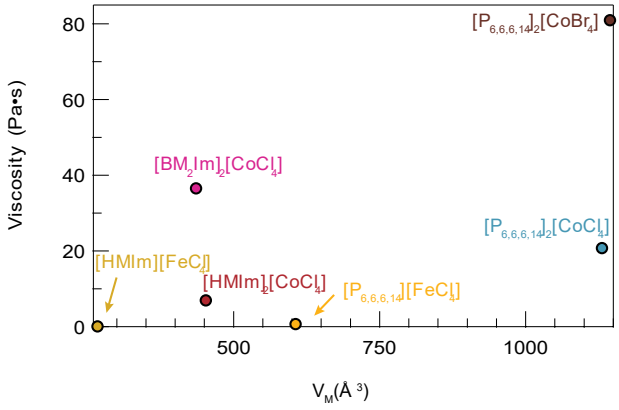

Figure A23. Viscosity vs Molecular volume plot for various ILs reported here.

Table A1. Cartesian coordinates of the geometry-optimized $VOCl_3^-$, $VOCl_4^{2-}$, VCl_4^-, VCl_6^{3-}, elongated V-Cl bond lengths, and dimer of VCl_6-VCl_3.

$VOCl_3$	x	y	z
V	-6.54395396670483	-0.29232762795535	0.13184713553779
Cl	-4.30396504074253	-0.11286832297413	-0.10238102334569
Cl	-7.23366461651539	0.73328938622419	-1.79069871721589
Cl	-7.36885566219071	1.14310590690421	1.66904573937769
O	-7.16266071384653	-1.75805934219890	0.09218686564611
$VOCl_4$	x	y	z
V	-6.77774206956111	-0.32267787042807	-0.09851996408668
Cl	-4.89066532554752	-0.95593506088053	1.24665349193267
Cl	-7.97581116882425	1.03030690377371	-1.68451249998524
Cl	-6.98694572187346	1.52266865101555	1.36158473423461
Cl	-5.48455985195872	-1.03532081020180	-1.94084159946864
O	-7.84948586223495	-1.43877181327886	0.27334583737328
VCl_4	x	y	z
V	-6.52030464311140	-0.05616575429708	-0.00320320170501
Cl	-4.27513726523367	-0.05913984233518	0.00671431729897
Cl	-7.27818443044818	0.82638884085433	-1.92263550953603
Cl	-7.26880567133938	1.16269435152964	1.72477074071618
Cl	-7.27066798986735	-2.16062759575171	0.19435365322590
VCl_6	x	y	z
V	-2.04827040285955	0.61559165990641	-0.00824454676758
Cl	-1.98505709364099	3.02199997188484	0.02765505294522
Cl	0.35125088724121	0.55196150754853	0.08208263580656
Cl	-2.11088756505193	-1.79076546605242	-0.04477317837910
Cl	-4.44827280465886	0.68004376450511	-0.09791734600515
Cl	-1.95109847850913	0.65116468755874	-2.46641657783130
Cl	-2.14766454252075	0.57938387464879	2.45056396023135

V-Cl Bond Length 230 ppm

	X	Y	Z
V	-6.55789964977586	-0.00827422937702	-0.10046531344177
Cl	-4.31920704773071	0.00849748862575	-0.13142508719586
Cl	-7.32487137893691	0.90232275212788	-2.06834933155979
Cl	-7.32305357655084	1.23222344743809	1.59741948347180
Cl	-7.33057834700569	-2.10261945881471	0.05219024872562

V-Cl Bond Length 240 ppm

	X	Y	Z
V	-6.52833381715816	-0.04657308607269	-0.01888738670304
Cl	-4.30324490329034	0.02246393583263	-0.16526161033795
Cl	-7.32676544947378	0.90718513159555	-2.07141075737732
Cl	-7.34613698007190	1.26993228123850	1.58578980987496
Cl	-7.35112885000581	-2.12085826259398	0.01913994454335

V-Cl Bond Length 245 ppm

	X	Y	Z
V	-6.50757463363672	-0.06937119000275	0.03144229256899
Cl	-4.29299031998065	0.03231275962039	-0.18993753503235
Cl	-7.32532621015501	0.90366223683106	-2.06307156851530
Cl	-7.36339700696933	1.29071508995106	1.57469018479710
Cl	-7.36632182925828	-2.12516889639976	-0.00375337381843

V-Cl Bond Length 260 ppm

	X	Y	Z
V	-6.47689731842737	-0.10708148137169	0.10769460935215
Cl	-4.28194073844320	0.04003428220193	-0.20558527361019
Cl	-7.34252320012089	0.93168046264819	-2.11304073317845
Cl	-7.37578764409360	1.30171298148820	1.57014499707245
Cl	-7.37846109891493	-2.13419624496663	-0.00984359963596

V-Cl Bond Length 275 ppm

	x	y	z
V	-6.45294780461319	-0.13549553655009	0.17189449288147
Cl	-4.27530519260705	0.04180868750040	-0.20411194058639
Cl	-7.36856901468163	0.95728298177204	-2.17969495142264
Cl	-7.37582047862366	1.30780206857354	1.57721415666044
Cl	-7.38296750947447	-2.13924820129588	-0.01593175753289

V-Cl Bond Length 300 ppm

	x	y	z
V	-6.41823680941886	-0.17415210552639	0.26611334320177
Cl	-4.26724913882586	0.03733815373071	-0.19321904489178
Cl	-7.41697229529935	1.00286368644475	-2.30627100776400
Cl	-7.37119566125940	1.30791372188408	1.59967371680589
Cl	-7.38195609519653	-2.14181345653315	-0.01692700735188

Dimer	x	y	z
V	3.22531	1.67175	17.34155
Cl	5.24275	1.91686	18.47855
Cl	3.80113	3.30304	15.73472
Cl	1.94261	3.04414	18.62522
Cl	1.52535	0.68638	16.04624
Cl	2.72630	-0.41616	18.86678
Cl	4.60530	-0.22168	15.97779
V	3.11477	-1.66213	16.96931
Cl	4.46817	-3.29354	17.69622
Cl	1.55936	-2.73064	15.77998

Table A2. Viscoelastic and volumetric properties of selected ILs. V_0: occupied volume. V_M: molecular volume.

Ionic Liquid	M.W. (g/mol)	Density (g/L)	Molarity (mol/L)	V_0(L/mol)	V_M(Å^3)
$[P_{6,6,6,14}]_2[CoCl_4]$	1168.46	1218	1.04	0.96	1130.50
$[P_{6,6,6,14}]_2[CoBr_4]$	1346.26	1478	1.10	0.91	1144.28
$[HMIm]_2[CoCl_4]$	535.28	714	1.33	0.75	452.59
$[BM_2Im]_2[CoCl_4]$	507.22	896	1.76	0.57	435.84
$[P_{6,6,6,14}][FeCl_4]$	790.26	1016	1.42	0.70	606.07
$[HMIm][FeCl_4]$	473.67	931	1.95	0.51	267.11

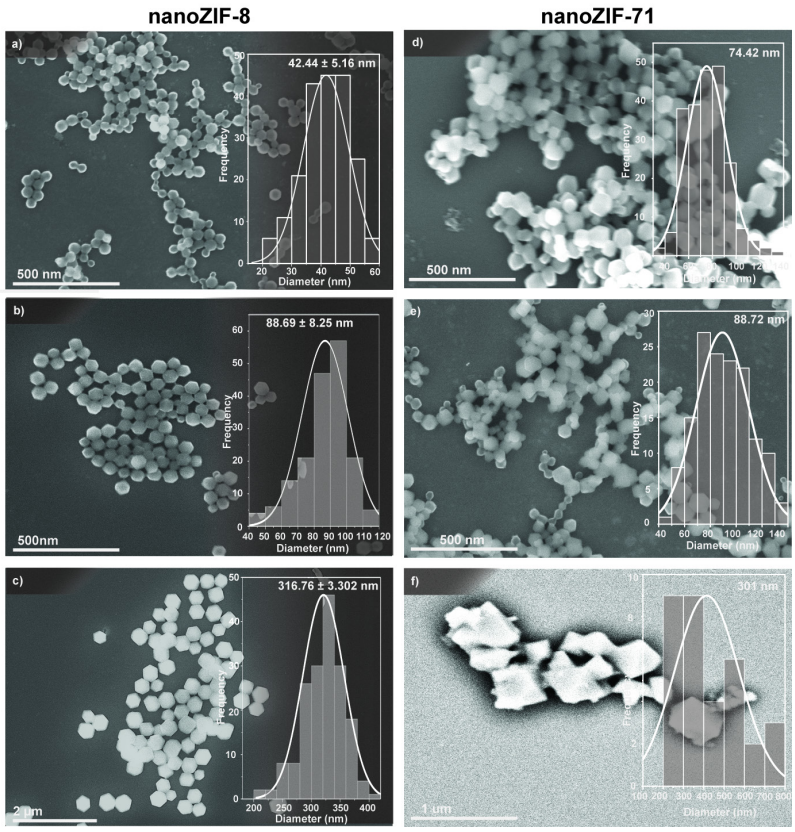

Figure B1. SEM images of (a-c) ZIF-8 nanoparticles and (d-f) ZIF-71 nanoparticles synthesized to produce different sizes.

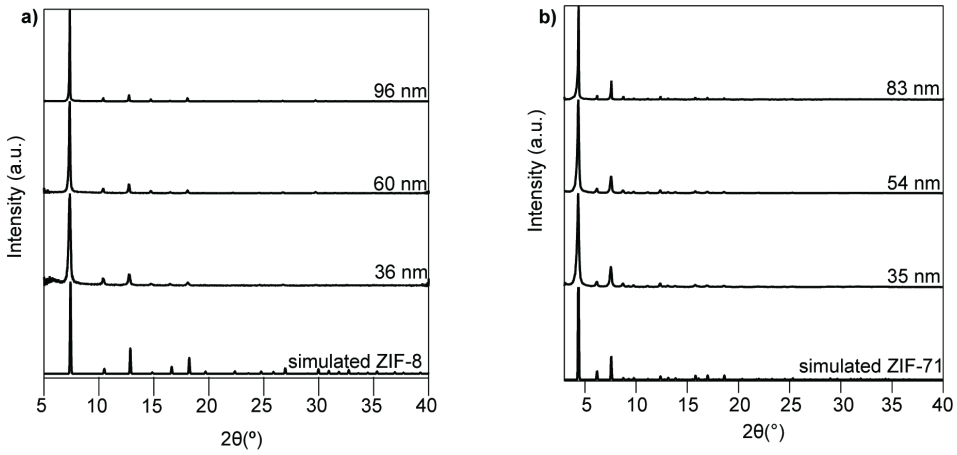

Figure B2. PXRD patterns of powder **A)** nanoZIF-8 and **B)** nanoZIF-71 synthesized for three different sizes. Expected reflections are shown as the bottom trace. Sizes are determined by Scherrer analysis.

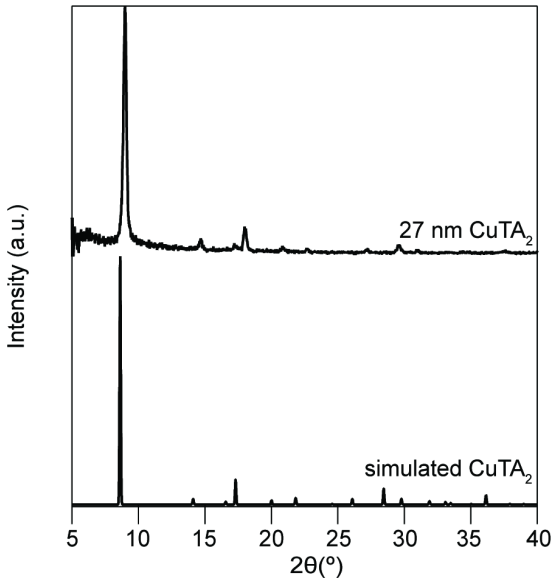

Figure B3. PXRD pattern of powder CuTA2.

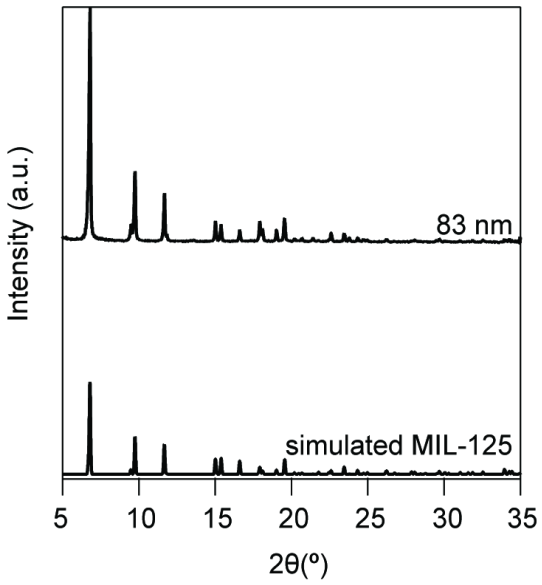

Figure B4. PXRD pattern of powder MIL-125.

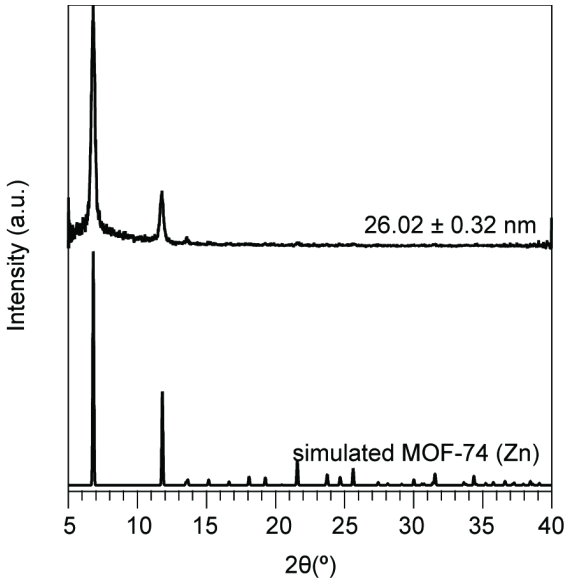

Figure B5. PXRD pattern of MOF-74 (Zn).

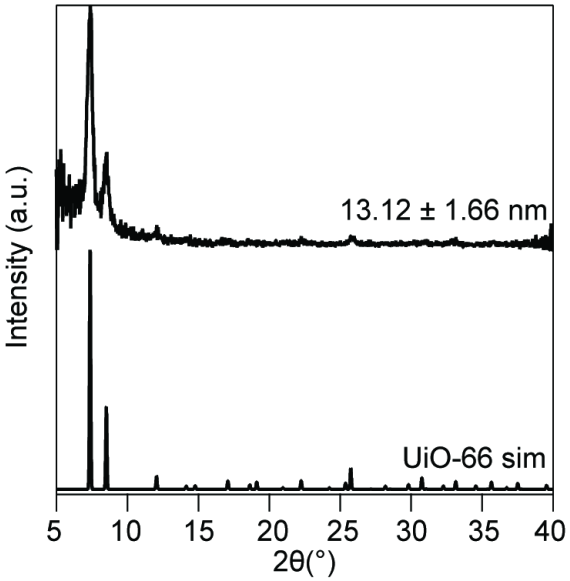

Figure B6. PXRD patterns of powder UiO-66.

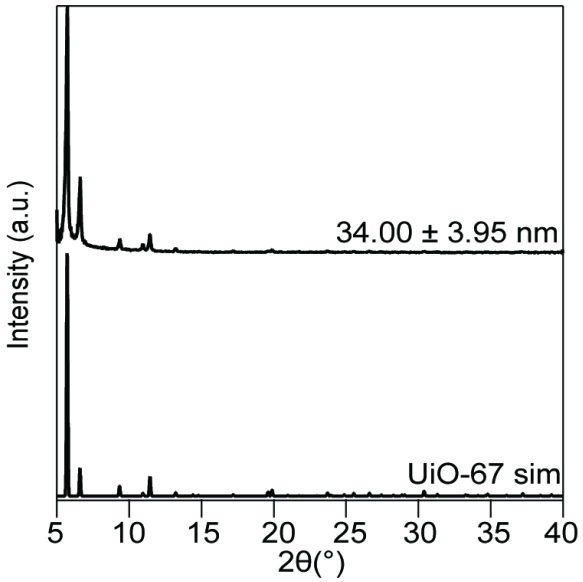

Figure B7. PXRD patterns of powder UiO-67.

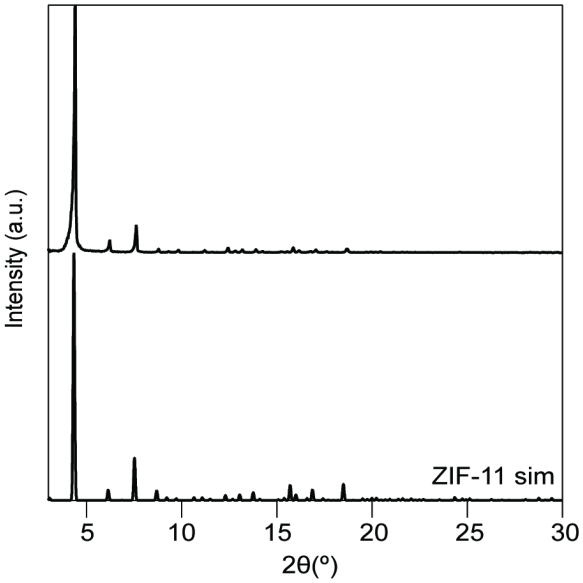

Figure B8. PXRD pattern of powder ZIF-11.

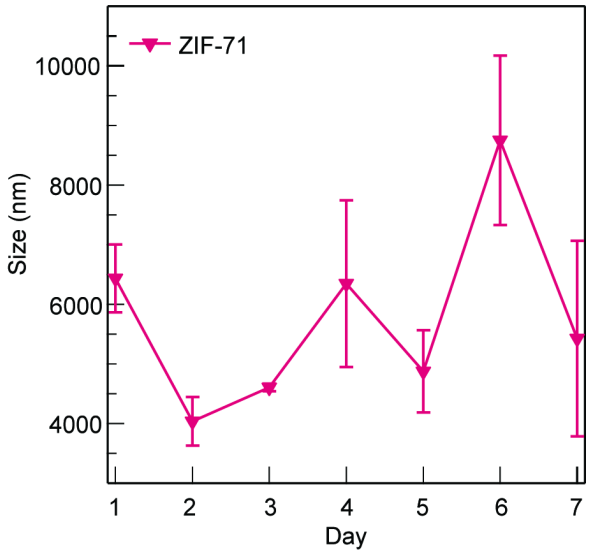

Figure B9. Size stability of nanoZIF-71 over seven days measured by dynamic light scattering.

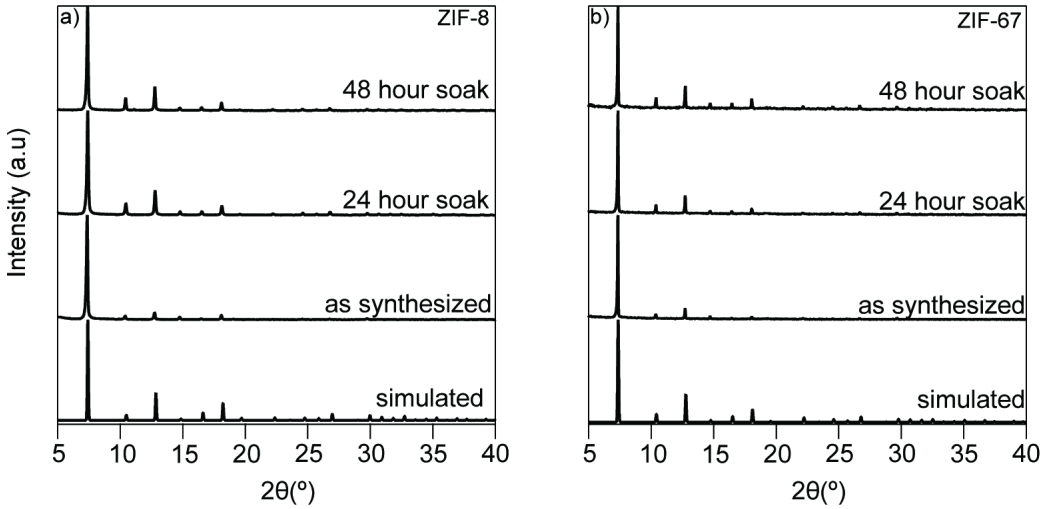

Figure B10. PXRD patters of nanoZIF-8 and ZIF-67 exposed to 18.2 MΩ H_2O over 48 hours.

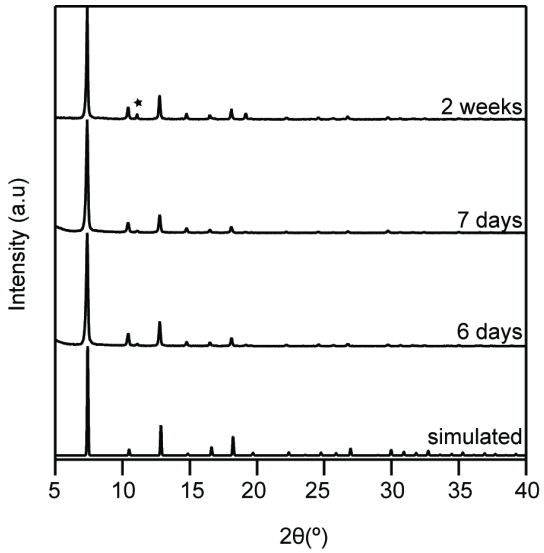

Figure B11. PXRD patterns of ZIF-8 aliquots immersed in 18.2 MΩ H_2O over two weeks. The star denotes formation of new crystalline phase from degradation.

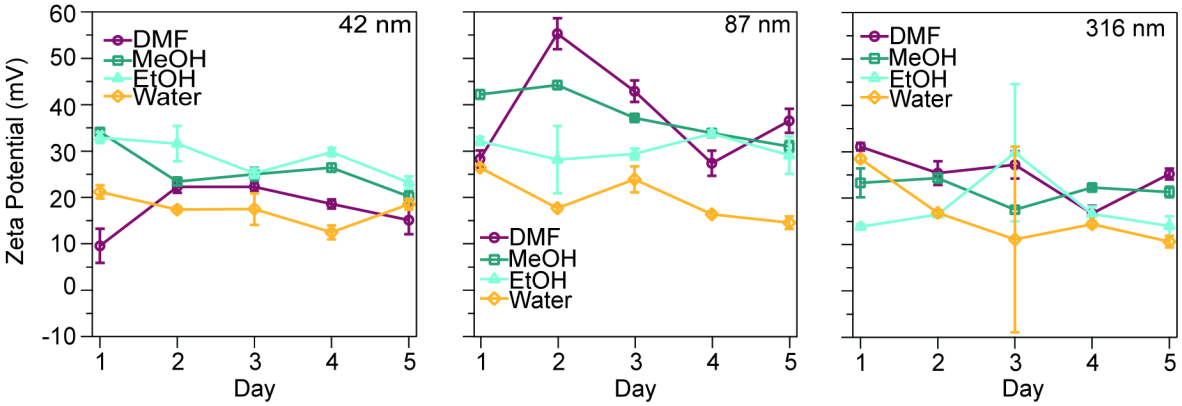

Figure B12. Zeta potentials of 42-nm (left), 87-nm (middle), and 316-nm (right) diameter nanoZIF-8 particles measured over a 5-day period in dimethylformamide (DMF), methanol (MeOH), ethanol (EtOH), and water

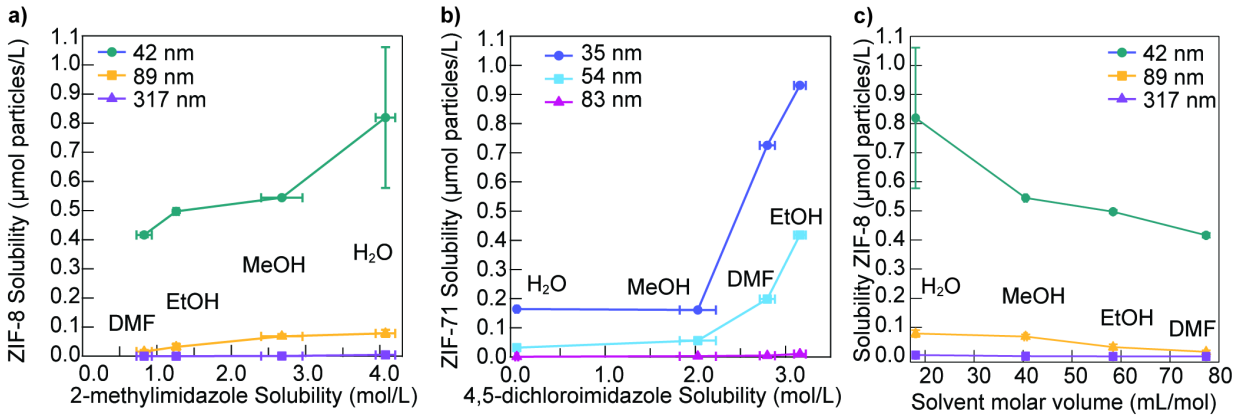

Figure B13. a) Particle solubility of nanoZIF-8 versus linker solubility. b) Particle solubility ZIF- 71 versus linker solubility. c) Particle solubility nanoZIF-8 versus molar volume.

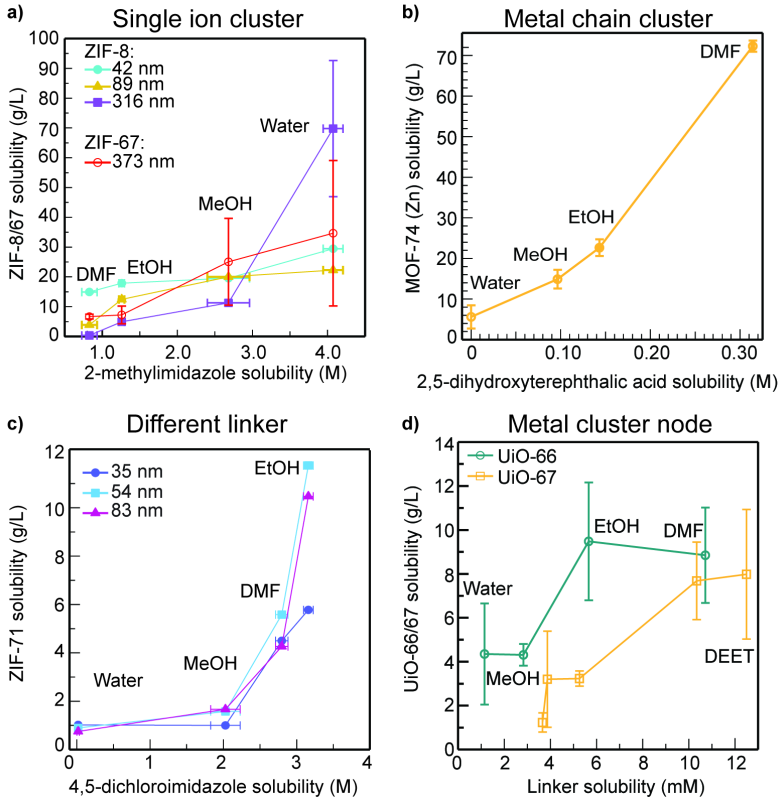

Figure B14. a) Solubility of nanoZIF-8 (g/L) versus linker solubility. b) Particle solubility Zn-MOF-74 (g/L) versus linker solubility. c) Particle solubility nanoZIF-71 (g/L) versus linker solubility. d) Solubility UiO-66/67 (g/L) versus linker solubility.

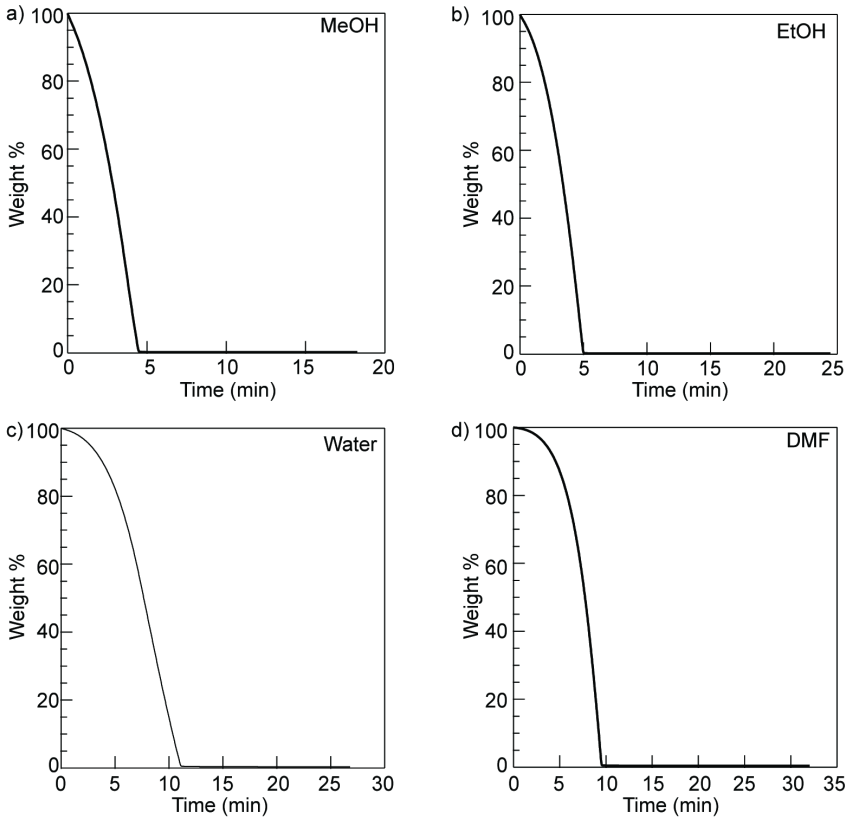

Figure B15. Representative TGA traces of nanoZIF-8 evaporated from: a) methanol b) ethanol c) water d) *N*,*N*-dimethylformamide.

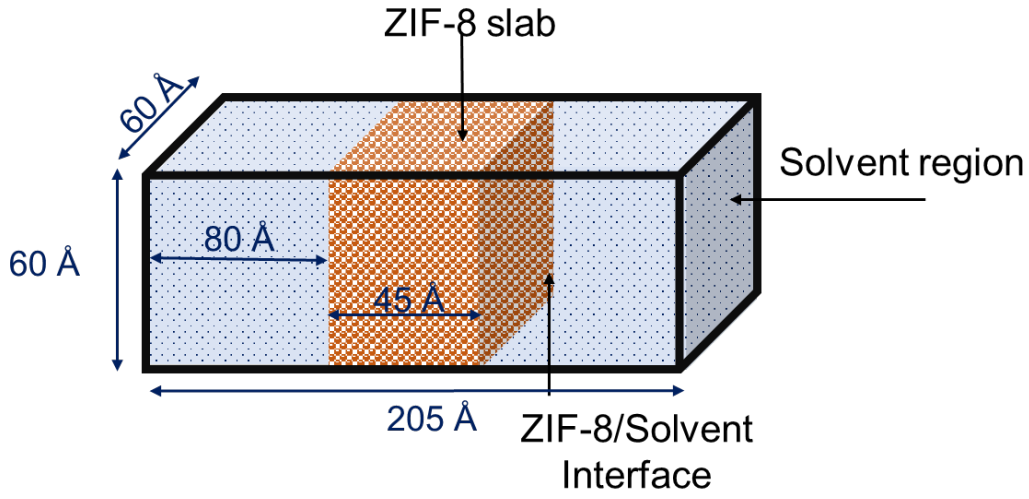

Figure B16. Schematic of model the ZIF-8/solvent systems used in the simulations.

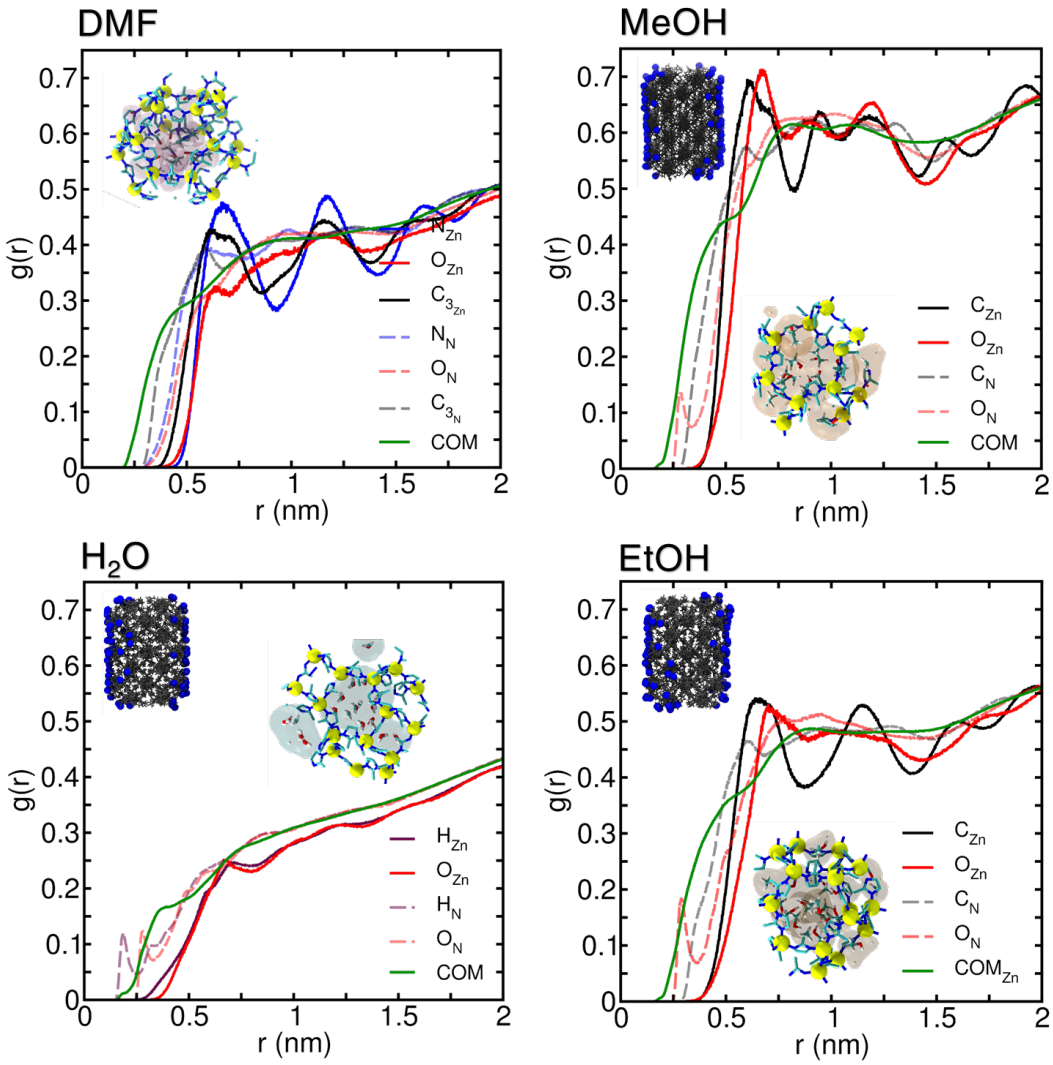

Figure B17. Solvent radial distributions functions for **(a)** DMF, **(b)** MeOH, **(c)** H_2O, and **(d)** EtOH with respect to Zn (yellow) and N atoms of ZIF-8. COM: center of mass. Subscripts denote the reference atom. Insets: (i) Nitrogen atoms with short-contacts of ZIF-8 linker at the ZIF-8/solvent interface indicated by blue spheres, (ii) local environment of large pore in the respective solvent.

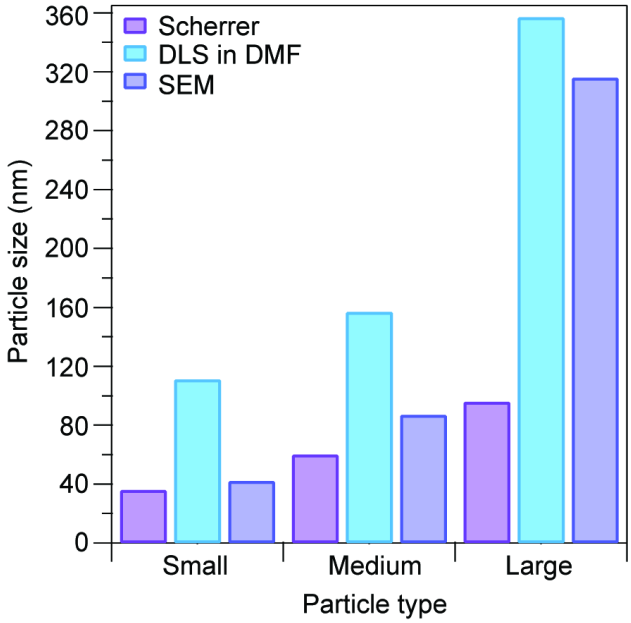

Figure B18. Size analysis of ZIF-8 nanoparticles by three sizing methods.

Table B1. Immersion enthalpies of ZIF-8-A, B and C in DMF and methanol.

Sample	**Particle Size (nm)**	**Enthalpy of Immersion *DMF***		**Enthalpy of Immersion *Methanol***	
		J/g Zn	*kJ/mol Zn*	*J/g Zn*	*kJ/mol Zn*
ZIF-8-A	42 ± 5.2	– 83.9 ± 1.9	– 19.1 ± 0.4	– 85.9 ± 2.8	– 19.5 ± 0.6
ZIF-8-B	89 ± 8.3	– 84.1 ± 2.2	– 19.1 ± 0.5	– 76.8 ± 1.5	– 17.5 ± 0.3
ZIF-8-C	316.0 ± 23.7	– 78.5 ± 1.4	– 17.9 ± 0.3	– 87.4 ± 2.5	– 19.9 ± 0.7

References

(1) Creton, C.; Ciccotti, M. Fracture and Adhesion of Soft Materials: A Review. *Rep. Prog. Phys.* **2016**, *79* (4), 046601. https://doi.org/10.1088/0034-4885/79/4/046601.

(2) Nagel, S. R. Experimental Soft-Matter Science. *Rev. Mod. Phys.* **2017**, *89* (2), 025002. https://doi.org/10.1103/RevModPhys.89.025002.

(3) Whitesides, G. M.; Lipomi, D. J. Soft Nanotechnology: "Structure"vs."Function." *Faraday Discuss.* **2009**, *143*, 373. https://doi.org/10.1039/b917540g.

(4) Hamley, I. W. Nanotechnology with Soft Materials. *Angew. Chem. Int. Ed.* **2003**, *42* (15), 1692–1712. https://doi.org/10.1002/anie.200200546.

(5) Mezzenga, R. Grand Challenges in Soft Matter. *Front. Soft Matter* **2021**, *1*, 811842. https://doi.org/10.3389/frsfm.2021.811842.

(6) Likos, C. N. Soft Matter with Soft Particles. *Soft Matter* **2006**, *2* (6), 478. https://doi.org/10.1039/b601916c.

(7) Kruse, J.; Langer, M.; Romanenko, I.; Trentin, I.; Hernández-Castillo, D.; González, L.; Schacher, F. H.; Streb, C. Polyoxometalate-Soft Matter Composite Materials: Design Strategies, Applications, and Future Directions. *Adv. Funct. Mater.* **2022**, *32* (51), 2208428. https://doi.org/10.1002/adfm.202208428.

(8) Löwen, H. Colloidal Soft Matter under External Control. *J. Phys. Condens. Matter* **2001**, *13* (24), R415–R432. https://doi.org/10.1088/0953-8984/13/24/201.

(9) Kempaiah, R.; Nie, Z. From Nature to Synthetic Systems: Shape Transformation in Soft Materials. *J Mater Chem B* **2014**, *2* (17), 2357–2368. https://doi.org/10.1039/C3TB21462A.

(10) Yang, X.; Cao, H.; Li, X. Fabricated Soft Materials for Cell Biology and Tissue Engineering Applications: A Review. *Mater. Today Commun.* **2024**, *38*, 108563. https://doi.org/10.1016/j.mtcomm.2024.108563.

(11) Zhao, X.; Chen, X.; Yuk, H.; Lin, S.; Liu, X.; Parada, G. Soft Materials by Design: Unconventional Polymer Networks Give Extreme Properties. *Chem. Rev.* **2021**, *121* (8), 4309–4372. https://doi.org/10.1021/acs.chemrev.0c01088.

(12) Hu, H.; Gopinadhan, M.; Osuji, C. O. Directed Self-Assembly of Block Copolymers: A Tutorial Review of Strategies for Enabling Nanotechnology with Soft Matter. *Soft Matter* **2014**, *10* (22), 3867. https://doi.org/10.1039/c3sm52607k.

(13) Shimomura, M.; Sawadaishi, T. Bottom-up Strategy of Materials Fabrication: A New Trend in Nanotechnology of Soft Materials. *Curr. Opin. Colloid Interface Sci.* **2001**, *6* (1), 11–16. https://doi.org/10.1016/S1359-0294(00)00081-9.

(14) Nicole, L.; Rozes, L.; Sanchez, C. Integrative Approaches to Hybrid Multifunctional Materials: From Multidisciplinary Research to Applied Technologies. *Adv. Mater.* **2010**, *22* (29), 3208–3214. https://doi.org/10.1002/adma.201000231.

(15) Kitazawa, Y.; Ueno, K.; Watanabe, M. Advanced Materials Based on Polymers and Ionic Liquids. *Chem. Rec.* **2018**, *18* (4), 391–409. https://doi.org/10.1002/tcr.201700041.

(16) Lodge, T. P. A Unique Platform for Materials Design. *Science* **2008**, *321* (5885), 50–51. https://doi.org/10.1126/science.1159652.

(17) Lei, Z.; Chen, B.; Koo, Y.-M.; Macfarlane, D. R. Introduction: Ionic Liquids. *ACS Chem Rev* **2017**. https://doi.org/10.1021/acs.chemrev.7b00246.

(18) Zhang, X.; Huo, F.; Liu, X.; Dong, K.; He, H.; Yao, X.; Zhang, S. Influence of Microstructure and Interaction on Viscosity of Ionic Liquids. *Ind. Eng. Chem. Res.* **2015**, *54* (13), 3505–3514. https://doi.org/10.1021/acs.iecr.5b00415.
(19) Thompson, M. W.; Matsumoto, R.; Sacci, R. L.; Sanders, N. C.; Cummings, P. T. Scalable Screening of Soft Matter: A Case Study of Mixtures of Ionic Liquids and Organic Solvents. *J. Phys. Chem. B* **2019**, *123* (6), 1340–1347. https://doi.org/10.1021/acs.jpcb.8b11527.
(20) Ueki, T.; Watanabe, M. Macromolecules in Ionic Liquids: Progress, Challenges, and Opportunities. *Macromolecules* **2008**, *41* (11), 3739–3749. https://doi.org/10.1021/ma800171k.
(21) Torimoto, T.; Tsuda, T.; Okazaki, K.; Kuwabata, S. New Frontiers in Materials Science Opened by Ionic Liquids. *Adv. Mater.* **2010**, *22* (11), 1196–1221. https://doi.org/10.1002/adma.200902184.
(22) Wang, Y.-L.; Zhu, Y.-L.; Lu, Z.-Y.; Laaksonen, A. Electrostatic Interactions in Soft Particle Systems: Mesoscale Simulations of Ionic Liquids. *Soft Matter* **2018**, *14* (21), 4252–4267. https://doi.org/10.1039/C8SM00387D.
(23) Pei, Y.; Zhang, Y.; Ma, J.; Fan, M.; Zhang, S.; Wang, J. Ionic Liquids for Advanced Materials. *Mater. Today Nano* **2022**, *17*, 100159. https://doi.org/10.1016/j.mtnano.2021.100159.
(24) Ueno, K. Soft Materials Based on Colloidal Self-Assembly in Ionic Liquids. *Polym. J.* **2018**, *50* (10), 951–958. https://doi.org/10.1038/s41428-018-0083-1.
(25) He, Z.; Alexandridis, P. Nanoparticles in Ionic Liquids: Interactions and Organization. *Phys. Chem. Chem. Phys.* **2015**, *17* (28), 18238–18261. https://doi.org/10.1039/C5CP01620G.
(26) Ueno, K.; Watanabe, M. From Colloidal Stability in Ionic Liquids to Advanced Soft Materials Using Unique Media. *Langmuir* **2011**, *27* (15), 9105–9115. https://doi.org/10.1021/la103942f.
(27) Matsumoto, A.; Shen, A. Q. Rheological Scaling of Ionic-Liquid-Based Polyelectrolytes in Ionic Liquid Solutions: The Effect of the Ion Diameter of Ionic Liquids. *Soft Matter* **2022**, *18* (21), 4197–4204. https://doi.org/10.1039/D2SM00484D.
(28) Nakamura, I.; Shock, C. J.; Eggart, L.; Gao, T. Theoretical Aspects of Ionic Liquids for Soft-Matter Sciences. *Isr. J. Chem.* **2019**, *59* (9), 813–823. https://doi.org/10.1002/ijch.201800143.
(29) D'Anna, F.; Rizzo, C.; Vitale, P.; Lazzara, G.; Noto, R. Dicationic Organic Salts: Gelators for Ionic Liquids. *Soft Matter* **2014**, *10* (46), 9281–9292. https://doi.org/10.1039/C4SM01360C.
(30) Ueno, K.; Fukai, T.; Nagatsuka, T.; Yasuda, T.; Watanabe, M. Solubility of Poly(Methyl Methacrylate) in Ionic Liquids in Relation to Solvent Parameters. *Langmuir* **2014**, *30* (11), 3228–3235. https://doi.org/10.1021/la404797g.
(31) Li, Q.; Yan, F.; Texter, J. Polymerized and Colloidal Ionic Liquids–Syntheses and Applications. *Chem. Rev.* **2024**, *124* (7), 3813–3931. https://doi.org/10.1021/acs.chemrev.3c00429.
(32) Nabais, A. R.; Neves, L. A.; Tomé, L. C. Mixed-Matrix Ion Gel Membranes for Gas Separation. *ACS Appl. Polym. Mater.* **2022**, *4* (5), 3098–3119. https://doi.org/10.1021/acsapm.1c01737.

(33) Rijnaarts, T.; Mejia-Ariza, R.; Egberink, R. J. M.; van Roosmalen, W.; Huskens, J. Metal–Organic Frameworks (MOFs) as Multivalent Materials: Size Control and Surface Functionalization by Monovalent Capping Ligands. *Chem. – Eur. J.* **2015**, *21* (29), 10296–10301. https://doi.org/10.1002/chem.201501974.
(34) Avci, C.; Imaz, I.; Carné-Sánchez, A.; Pariente, J. A.; Tasios, N.; Pérez-Carvajal, J.; Alonso, M. I.; Blanco, A.; Dijkstra, M.; López, C.; Maspoch, D. Self-Assembly of Polyhedral Metal–Organic Framework Particles into Three-Dimensional Ordered Superstructures. *Nat. Chem.* **2018**, *10* (1), 78–84. https://doi.org/10.1038/nchem.2875.
(35) Pan, Y.; Liu, Y.; Zeng, G.; Zhao, L.; Lai, Z. Rapid Synthesis of Zeolitic Imidazolate Framework-8 (ZIF-8) Nanocrystals in an Aqueous System. *Chem. Commun.* **2011**, *47* (7), 2071. https://doi.org/10.1039/c0cc05002d.
(36) Díaz-García, M.; Mayoral, Á.; Díaz, I.; Sánchez-Sánchez, M. Nanoscaled M-MOF-74 Materials Prepared at Room Temperature. *Cryst. Growth Des.* **2014**, *14* (5), 2479–2487. https://doi.org/10.1021/cg500190h.
(37) Hu, S.; Liu, M.; Guo, X.; Li, K.; Han, Y.; Song, C.; Zhang, G. Effects of Monocarboxylic Acid Additives on Synthesizing Metal–Organic Framework NH_2-MIL-125 with Controllable Size and Morphology. *Cryst. Growth Des.* **2017**, *17* (12), 6586–6595. https://doi.org/10.1021/acs.cgd.7b01250.
(38) Hareesha, N.; Manjunatha, J. G. A Simple and Low-Cost Poly (Dl-Phenylalanine) Modified Carbon Sensor for the Improved Electrochemical Analysis of Riboflavin. *J. Sci. Adv. Mater. Devices* **2020**, *5* (4), 502–511. https://doi.org/10.1016/j.jsamd.2020.08.005.
(39) Mandal, S.; Natarajan, S.; Mani, P.; Pankajakshan, A. Post-Synthetic Modification of Metal–Organic Frameworks Toward Applications. *Adv. Funct. Mater.* **2021**, *31* (4), 2006291. https://doi.org/10.1002/adfm.202006291.
(40) Rojas, S.; Guillou, N.; Horcajada, P. Ti-Based nanoMOF as an Efficient Oral Therapeutic Agent. *ACS Appl. Mater. Interfaces* **2019**, *11* (25), 22188–22193. https://doi.org/10.1021/acsami.9b06472.
(41) Wu, W.; Liu, J.; Li, Z.; Zhao, X.; Liu, G.; Liu, S.; Ma, S.; Li, W.; Liu, W. Surface-Functionalized nanoMOFs in Oil for Friction and Wear Reduction and Antioxidation. *Chem. Eng. J.* **2021**, *410*, 128306. https://doi.org/10.1016/j.cej.2020.128306.
(42) Marshall, C. R.; Staudhammer, S. A.; Brozek, C. K. Size Control over Metal–Organic Framework Porous Nanocrystals. *Chem. Sci.* **2019**, *10* (41), 9396–9408. https://doi.org/10.1039/C9SC03802G.
(43) Marshall, C. R.; Timmel, E. E.; Staudhammer, S. A.; Brozek, C. K. Experimental Evidence for a General Model of Modulated MOF Nanoparticle Growth. *Chem. Sci.* **2020**, *11* (42), 11539–11547. https://doi.org/10.1039/d0sc04845c.
(44) Marshall, C. R.; Dvorak, J. P.; Twight, L. P.; Chen, L.; Kadota, K.; Andreeva, A. B.; Overland, A. E.; Ericson, T.; Cozzolino, A. F.; Brozek, C. K. Size-Dependent Properties of Solution-Processable Conductive MOF Nanocrystals. *J Am Chem Soc* **2022**.
(45) Cheng, Y.; Wang, Z.; Zhao, D. Mixed Matrix Membranes for Natural Gas Upgrading: Current Status and Opportunities. *Ind. Eng. Chem. Res.* **2018**, *57* (12), 4139–4169. https://doi.org/10.1021/acs.iecr.7b04796.

(46) Mondal, P.; Cohen, S. M. Self-Healing Mixed Matrix Membranes Containing Metal–Organic Frameworks. *Chem. Sci.* **2022**, *13* (41), 12127–12135. https://doi.org/10.1039/D2SC04345A.
(47) Moreton, J. C.; Denny, M. S.; Cohen, S. M. High MOF Loading in Mixed-Matrix Membranes Utilizing Styrene/Butadiene Copolymers. *Chem. Commun.* **2016**, *52* (100), 14376–14379. https://doi.org/10.1039/C6CC07329H.
(48) Seoane, B.; Coronas, J.; Gascon, I.; Benavides, M. E.; Karvan, O.; Caro, J.; Kapteijn, F.; Gascon, J. Metal–Organic Framework Based Mixed Matrix Membranes: A Solution for Highly Efficient CO_2 Capture? *Chem. Soc. Rev.* **2015**, *44* (8), 2421–2454. https://doi.org/10.1039/C4CS00437J.
(49) Qian, Q.; Asinger, P. A.; Lee, M. J.; Han, G.; Mizrahi Rodriguez, K.; Lin, S.; Benedetti, F. M.; Wu, A. X.; Chi, W. S.; Smith, Z. P. MOF-Based Membranes for Gas Separations. *Chem. Rev.* **2020**, *120* (16), 8161–8266. https://doi.org/10.1021/acs.chemrev.0c00119.
(50) Ren, Y.; Liang, X.; Dou, H.; Ye, C.; Guo, Z.; Wang, J.; Pan, Y.; Wu, H.; Guiver, M. D.; Jiang, Z. Membrane-Based Olefin/Paraffin Separations. *Adv. Sci.* **2020**, *7* (19), 2001398. https://doi.org/10.1002/advs.202001398.
(51) Sanders, D. F.; Smith, Z. P.; Guo, R.; Robeson, L. M.; McGrath, J. E.; Paul, D. R.; Freeman, B. D. Energy-Efficient Polymeric Gas Separation Membranes for a Sustainable Future: A Review. *Polymer* **2013**, *54* (18), 4729–4761. https://doi.org/10.1016/j.polymer.2013.05.075.
(52) Monsanto Unveils New Separation Technology. *Chem. Eng. News Arch.* **1979**, *57* (47), 6–7. https://doi.org/10.1021/cen-v057n047.p006a.
(53) Bernardo, P.; Drioli, E.; Golemme, G. Membrane Gas Separation: A Review/State of the Art. *Ind. Eng. Chem. Res.* **2009**, *48* (10), 4638–4663. https://doi.org/10.1021/ie8019032.
(54) Robeson, L. M. Correlation of Separation Factor versus Permeability for Polymeric Membranes. *J. Membr. Sci.* **1991**, *62* (2), 165–185. https://doi.org/10.1016/0376-7388(91)80060-J.
(55) Tanh Jeazet, H. B.; Staudt, C.; Janiak, C. Metal–Organic Frameworks in Mixed-Matrix Membranes for Gas Separation. *Dalton Trans.* **2012**, *41* (46), 14003. https://doi.org/10.1039/c2dt31550e.
(56) Yu, S.; Li, C.; Zhao, S.; Chai, M.; Hou, J.; Lin, R. Recent Advances in the Interfacial Engineering of MOF-Based Mixed Matrix Membranes for Gas Separation. *Nanoscale* **2024**, 10.1039.D4NR00096J. https://doi.org/10.1039/D4NR00096J.
(57) Cowan, M. G.; Gin, D. L.; Noble, R. D. Poly(Ionic Liquid)/Ionic Liquid Ion-Gels with High "Free" Ionic Liquid Content: Platform Membrane Materials for CO_2 /Light Gas Separations. *Acc. Chem. Res.* **2016**, *49* (4), 724–732. https://doi.org/10.1021/acs.accounts.5b00547.
(58) Zhang, S.; Zhang, J.; Zhang, Y.; Deng, Y. Nanoconfined Ionic Liquids. *Chem. Rev.* **2017**, *117* (10), 6755–6833. https://doi.org/10.1021/acs.chemrev.6b00509.
(59) Jiang, S.; Hu, Y.; Wang, Y.; Wang, X. Viscosity of Typical Room-Temperature Ionic Liquids: A Critical Review. *J. Phys. Chem. Ref. Data* **2019**, *48* (3), 033101. https://doi.org/10.1063/1.5090486.

(60) Shakeel, A.; Mahmood, H.; Farooq, U.; Ullah, Z.; Yasin, S.; Iqbal, T.; Chassagne, C.; Moniruzzaman, M. Rheology of Pure Ionic Liquids and Their Complex Fluids: A Review. *ACS Sustain. Chem. Eng.* **2019**, *7* (16), 13586–13626. https://doi.org/10.1021/acssuschemeng.9b02232.

(61) Lei, Z.; Chen, B.; Koo, Y.-M.; MacFarlane, D. R. Introduction: Ionic Liquids. *Chem. Rev.* **2017**, *117* (10), 6633–6635. https://doi.org/10.1021/acs.chemrev.7b00246.

(62) Small, L. J.; Pratt, H. D.; Staiger, C. L.; Anderson, T. M. MetILs 3 : A Strategy for High Density Energy Storage Using Redox-Active Ionic Liquids. *Adv. Sustain. Syst.* **2017**, *1* (9), 1700066. https://doi.org/10.1002/adsu.201700066.

(63) Hernández, G.; Işik, M.; Mantione, D.; Pendashteh, A.; Navalpotro, P.; Shanmukaraj, D.; Marcilla, R.; Mecerreyes, D. Redox-Active Poly(Ionic Liquid)s as Active Materials for Energy Storage Applications. *J. Mater. Chem. A* **2017**, *5* (31), 16231–16240. https://doi.org/10.1039/C6TA10056B.

(64) Schaltin, S.; Li, Y.; Brooks, N. R.; Sniekers, J.; Vankelecom, I. F. J.; Binnemans, K.; Fransaer, J. Towards an All-Copper Redox Flow Battery Based on a Copper-Containing Ionic Liquid. *Chem. Commun. Camb. Engl.* **2016**, *52* (2), 414–417. https://doi.org/10.1039/c5cc06774j.

(65) Cappillino, P. J.; Pratt, H. D.; Hudak, N. S.; Tomson, N. C.; Anderson, T. M.; Anstey, M. R. Application of Redox Non-Innocent Ligands to Non-Aqueous Flow Battery Electrolytes. *Adv. Energy Mater.* **2014**, *4* (1), 1300566. https://doi.org/10.1002/aenm.201300566.

(66) Doherty, A. P. Redox-Active Ionic Liquids for Energy Harvesting and Storage Applications. *Curr. Opin. Electrochem.* **2018**, *7*, 61–65. https://doi.org/10.1016/j.coelec.2017.10.009.

(67) Lin, M.-C.; Gong, M.; Lu, B.; Wu, Y.; Wang, D.-Y.; Guan, M.; Angell, M.; Chen, C.; Yang, J.; Hwang, B.-J.; Dai, H. An Ultrafast Rechargeable Aluminium-Ion Battery. *Nature* **2015**, *520* (7547), 324–328. https://doi.org/10.1038/nature14340.

(68) Marszalek, M.; Fei, Z.; Zhu, D. R.; Scopelliti, R.; Dyson, P. J.; Zakeeruddin, S. M.; Grätzel, M. Application of Ionic Liquids Containing Tricyanomethanide [C(CN) 3]- or Tetracyanoborate [B(CN)4]- Anions in Dye-Sensitized Solar Cells. *Inorg. Chem.* **2011**, *50* (22), 11561–11567. https://doi.org/10.1021/ic201513m.

(69) Wang, P.; Zakeeruddin, S. M.; Moser, J.-E.; Humphry-Baker, R.; Grätzel, M. A Solvent-Free, SeCN -/(SeCN) 3-Based Ionic Liquid Electrolyte for High-Efficiency Dye-Sensitized Nanocrystalline Solar Cells. *J. Am. Chem. Soc.* **2004**, *126* (23), 7164–7165.

(70) Lau, G. P. S.; Décoppet, J.-D.; Moehl, T.; Zakeeruddin, S. M.; Grätzel, M.; Dyson, P. J. Robust High-Performance Dye-Sensitized Solar Cells Based on Ionic Liquid-Sulfolane Composite Electrolytes. *Sci. Rep.* **2015**, *5* (November), 18158–18166. https://doi.org/10.1038/srep18158.

(71) Bi, S.; Banda, H.; Chen, M.; Niu, L.; Chen, M.; Wu, T.; Wang, J.; Wang, R.; Feng, J.; Chen, T.; Dincă, M.; Kornyshev, A. A.; Feng, G. Molecular Understanding of Charge Storage and Charging Dynamics in Supercapacitors with MOF Electrodes and Ionic Liquid Electrolytes. *Nat. Mater.* **2020**, *19* (5), 552–558. https://doi.org/10.1038/s41563-019-0598-7.

(72) Matsumoto, M.; Shimizu, S.; Sotoike, R.; Watanabe, M.; Iwasa, Y.; Itoh, Y.; Aida, T. Exceptionally High Electric Double Layer Capacitances of Oligomeric Ionic Liquids. *J. Am. Chem. Soc.* **2017**, *139* (45), 16072–16075. https://doi.org/10.1021/jacs.7b09156.

(73) Mourad, E.; Coustan, L.; Lannelongue, P.; Zigah, D.; Mehdi, A.; Vioux, A.; Freunberger, S. A.; Favier, F.; Fontaine, O. Biredox Ionic Liquids with Solid-like Redox Density in the Liquid State for High-Energy Supercapacitors. *Nat. Mater.* **2016**, *16* (4), 446–453. https://doi.org/10.1038/nmat4808.
(74) Abraham, T. J.; MacFarlane, D. R.; Pringle, J. M. High Seebeck Coefficient Redox Ionic Liquid Electrolytes for Thermal Energy Harvesting. *Energy Environ. Sci.* **2013**, *6* (9), 2639. https://doi.org/10.1039/c3ee41608a.
(75) Mazaheripour, A.; Majumdar, S.; Hanemann-Rawlings, D.; Thomas, E. M.; McGuiness, C.; D'Alencon, L.; Chabinyc, M. L.; Segalman, R. A. Tailoring the Seebeck Coefficient of PEDOT:PSS by Controlling Ion Stoichiometry in Ionic Liquid Additives. *Chem. Mater.* **2018**, *30* (14), 4816–4822. https://doi.org/10.1021/acs.chemmater.8b02114.
(76) Abraham, T. J.; MacFarlane, D. R.; Pringle, J. M. Seebeck Coefficients in Ionic Liquids – Prospects for Thermo-Electrochemical Cells. *Chem. Commun.* **2011**, *47* (22), 6260. https://doi.org/10.1039/c1cc11501d.
(77) Rosen, B. a; Salehi-Khojin, A.; Thorson, M. R.; Zhu, W.; Whipple, D. T.; Kenis, P. J. a; Masel, R. I. Ionic Liquid-Mediated Selective Conversion of CO2 to CO at Low Overpotentials. *Science* **2011**, *334* (6056), 643–644. https://doi.org/10.1126/science.1209786.
(78) Yamamoto, T.; Matsumoto, K.; Hagiwara, R.; Nohira, T. Room-Temperature Fluoride Shuttle Batteries Based on a Fluorohydrogenate Ionic Liquid Electrolyte. *ACS Appl. Energy Mater.* **2019**, *2* (9), 6153–6157. https://doi.org/10.1021/acsaem.9b01260.
(79) Matsubara, Y.; Grills, D. C.; Kuwahara, Y. Thermodynamic Aspects of Electrocatalytic CO2 Reduction in Acetonitrile and with an Ionic Liquid as Solvent or Electrolyte. *ACS Catal.* **2015**, *5* (11), 6440–6452. https://doi.org/10.1021/acscatal.5b00656.
(80) Hollingsworth, N.; Taylor, S. F. R.; Galante, M. T.; Jacquemin, J.; Longo, C.; Holt, K. B.; De Leeuw, N. H.; Hardacre, C. Reduction of Carbon Dioxide to Formate at Low Overpotential Using a Superbase Ionic Liquid. *Angew Chem Int Ed* **2015**, *54* (47), 14164–14168. https://doi.org/10.1002/anie.201507629.
(81) Zhu, Q.; Ma, J.; Kang, X.; Sun, X.; Liu, H.; Hu, J.; Liu, Z.; Han, B. Efficient Reduction of CO2into Formic Acid on a Lead or Tin Electrode Using an Ionic Liquid Catholyte Mixture. *Angew Chem Int Ed* **2016**, *55* (31), 9012–9016. https://doi.org/10.1002/anie.201601974.
(82) Rosen, B. A.; Salehi-Khojin, A.; Thorson, M. R.; Zhu, W.; Whipple, D. T.; Kenis, P. J. A.; Masel, R. I. Ionic Liquid-Mediated Selective Conversion of CO2 to CO at Low Overpotentials. *Science* **2011**, *334* (6056), 643–644. https://doi.org/10.1126/science.1209786.
(83) Sun, L.; Ramesha, G. K.; Kamat, P. V.; Brennecke, J. F. Switching the Reaction Course of Electrochemical CO2 Reduction with Ionic Liquids. *Langmuir* **2014**, *30* (21), 6302–6308. https://doi.org/10.1021/la5009076.
(84) Lau, G. P. S.; Schreier, M.; Vasilyev, D.; Scopelliti, R.; Grätzel, M.; Dyson, P. J. New Insights into the Role of Imidazolium-Based Promoters for the Electroreduction of CO2 on a Silver Electrode. *J. Am. Chem. Soc.* **2016**, *138* (25), 7820–7823. https://doi.org/10.1021/jacs.6b03366.

(85) Matthews, R. P.; Welton, T.; Hunt, P. A. Competitive Pi Interactions and Hydrogen Bonding within Imidazolium Ionic Liquids. *Phys. Chem. Chem. Phys.* **2014**, *16* (7), 3238–3253. https://doi.org/10.1039/c3cp54672a.
(86) Hayes, R.; Warr, G. G.; Atkin, R. Structure and Nanostructure in Ionic Liquids. *Chem. Rev.* **2015**, *115* (13), 6357–6426. https://doi.org/10.1021/cr500411q.
(87) Slattery, J. M.; Daguenet, C.; Dyson, P. J.; Schubert, T. J. S.; Krossing, I. How to Predict the Physical Properties of Ionic Liquids: A Volume-Based Approach. *Angew. Chem.* **2007**, *119* (28), 5480–5484. https://doi.org/10.1002/ange.200700941.
(88) Fedorov, M. V.; Georgi, N.; Kornyshev, A. A. Double Layer in Ionic Liquids: The Nature of the Camel Shape of Capacitance. *Electrochem. Commun.* **2010**, *12* (2), 296–299. https://doi.org/10.1016/j.elecom.2009.12.019.
(89) Goodwin, Z. A. H.; Kornyshev, A. A. Underscreening, Overscreening and Double-Layer Capacitance. *Electrochem. Commun.* **2017**, *82* (July), 129–133. https://doi.org/10.1016/j.elecom.2017.07.008.
(90) Fedorov, M. V.; Kornyshev, A. A. Ionic Liquids at Electrified Interfaces. *Chem. Rev.* **2014**, *114* (5), 2978–3036. https://doi.org/10.1021/cr400374x.
(91) Kornyshev, A. A. Double-Layer in Ionic Liquids: Paradigm Change? *J. Phys. Chem. B* **2007**, *111* (20), 5545–5557. https://doi.org/10.1021/jp067857o.
(92) Mao, X.; Brown, P.; Červinka, C.; Hazell, G.; Li, H.; Ren, Y.; Chen, D.; Atkin, R.; Eastoe, J.; Grillo, I.; Padua, Agilio. A. H.; Costa Gomes, Margarida. F.; Hatton, T. A. Self-Assembled Nanostructures in Ionic Liquids Facilitate Charge Storage at Electrified Interfaces. *Nat. Mater.* **2019**, *18* (12), 1350–1357. https://doi.org/10.1038/s41563-019-0449-6.
(93) Rocha, M. A. A.; Neves, C. M. S. S.; Freire, M. G.; Russina, O.; Triolo, A.; Coutinho, J. A. P.; Santos, L. M. N. B. F. Alkylimidazolium Based Ionic Liquids: Impact of Cation Symmetry on Their Nanoscale Structural Organization. *J. Phys. Chem. B* **2013**, *117* (37), 10889–10897. https://doi.org/10.1021/jp406374a.
(94) Estager, J.; Nockemann, P.; Seddon, K. R.; Swadźba-Kwaśny, M.; Tyrrell, S. Validation of Speciation Techniques: A Study of Chlorozincate(II) Ionic Liquids. *Inorg. Chem.* **2011**, *50* (11), 5258–5271. https://doi.org/10.1021/ic200586u.
(95) Currie, M.; Estager, J.; Licence, P.; Men, S.; Nockemann, P.; Seddon, K. R.; Swadźba-Kwaśny, M.; Terrade, C. Chlorostannate(II) Ionic Liquids: Speciation, Lewis Acidity, and Oxidative Stability. *Inorg. Chem.* **2013**, *52* (4), 1710–1721. https://doi.org/10.1021/ic300241p.
(96) Gjikaj, M.; Xie, T.; Brockner, W. Uncommon Compounds in Antimony Pentachloride - Ionic Liquid Systems: Synthesis, Crystal Structure and Vibrational Spectra of the Complexes [TPT][SbCl6] and [Cl-EMIm][SbCl6]. *J. Inorg. Gen. Chem.* **2009**, *635* (6–7), 1036–1040. https://doi.org/10.1002/zaac.200801392.
(97) Wang, Q.; Geng, Y.; Lu, X.; Zhang, S. First-Row Transition Metal-Containing Ionic Liquids as Highly Active Catalysts for the Glycolysis of Poly(Ethylene Terephthalate) (PET). *ACS Sustain. Chem. Eng.* **2015**, *3* (2), 340–348. https://doi.org/10.1021/sc5007522.
(98) Jagadeeswara Rao, C.; Venkatesan, K. A.; Nagarajan, K.; Srinivasan, T. G.; Vasudeva Rao, P. R. Electrochemical and Thermodynamic Properties of Europium(III), Samarium(III) and

Cerium(III) in 1-Butyl-3-Methylimidazolium Chloride Ionic Liquid. *J. Nucl. Mater.* **2010**, *399* (1), 81–86. https://doi.org/10.1016/j.jnucmat.2010.01.005.
(99) Estager, J.; Holbrey, J. D.; Swadźba-Kwaśny, M. Halometallate Ionic Liquids-Revisited. *Chem. Soc. Rev.* **2014**, *43* (3), 847–886. https://doi.org/10.1039/c3cs60310e.
(100) Kore, R.; Berton, P.; Kelley, S. P.; Aduri, P.; Katti, S. S.; Rogers, R. D. Group IIIA Halometallate Ionic Liquids: Speciation and Applications in Catalysis. *ACS Catal.* **2017**, 7014–7028. https://doi.org/10.1021/acscatal.7b01793.
(101) Weingärtner, H. NMR Studies of Ionic Liquids: Structure and Dynamics. *Curr. Opin. Colloid Interface Sci.* **2013**, *18* (3), 183–189. https://doi.org/10.1016/j.cocis.2013.04.001.
(102) Nanda, R.; Damodaran, K. A Review of NMR Methods Used in the Study of the Structure and Dynamics of Ionic Liquids. *Magn. Reson. Chem.* **2018**, *56* (2), 62–72. https://doi.org/10.1002/mrc.4666.
(103) Noda, A.; Hayamizu, K.; Watanabe, M. Pulsed-Gradient Spin-Echo 1H and 19F NMR Ionic Diffusion Coefficient, Viscosity, and Ionic Conductivity of Non-Chloroaluminate Room-Temperature Ionic Liquids. *J. Phys. Chem. B* **2001**, *105* (20), 4603–4610. https://doi.org/10.1021/jp004132q.
(104) Currie, M.; Estager, J.; Licence, P.; Men, S.; Nockemann, P.; Seddon, K. R.; Swadźba, M.; Kwaśny, S.-K.; Terrade, C. C. Chlorostannate(II) Ionic Liquids: Speciation, Lewis Acidity, and Oxidative Stability. *Inorg Chem* **2013**, *52*. https://doi.org/10.1021/ic300241p.
(105) Hamer, N. K. The Spectra of Some Tetrahedral Halide Complexes of Transition Metal Ions. *Mol. Phys.* **1963**, *6* (3), 257–264. https://doi.org/10.1080/00268976300100291.
(106) Ferguson, J. Crystal-Field Spectra of D3,7 Ions. I. Electronic Absorption Spectrum of CoCl4- in Three Crystalline Environments. *J. Chem. Phys.* **1963**, *39* (1), 116–128. https://doi.org/10.1063/1.1733987.
(107) Weakliem, H. A. Optical Spectra of Ni2+, Co2+, and Cu2+ in Tetrahedral Sites in Crystals. *J. Chem. Phys.* **1962**, *36* (8), 2117–2140. https://doi.org/10.1063/1.1732840.
(108) Smith, G. Pedro.; Liu, C. H.; Griffiths, T. R. Charge-Transfer and Ligand-Field Spectra of Tetrahedral Tetrahalonickel(II) Ions in Molten Dimethyl Sulfone and Molten Organic Halide Salts. *J. Am. Chem. Soc.* **1964**, *86* (22), 4796–4802. https://doi.org/10.1021/ja01076a014.
(109) Goodgame, D. M. L. L.; Goodgame, M.; Cotton, F. A. Electronic Spectra of Some Tetrahedral Nickel(II) Complexes. *J. Am. Chem. Soc.* **1961**, *83* (20), 4161–4167. https://doi.org/10.1021/ja01481a014.
(110) Torardi, C. C.; Calabrese, J. C.; Deeth, R. J.; Hitchman, M. A.; Lehmann, G.; Sachs, H. *EPR and Optical Spectra of CuCl4 Doped into Single Crystals of Several Zinc(II) Host Lattices*; 1984; Vol. 23.
(111) Wenger, O. S.; Valiente, R.; Güdel, H. U. Influence of Hydrostatic Pressure on the Jahn-Teller Effect in the 4T2g Excited State of CrCl63- Doped Cs2NaScCl6. *J. Chem. Phys.* **2001**, *115* (8), 3819–3826. https://doi.org/10.1063/1.1387038.
(112) García-Lastra, J. M.; Moreno, M.; Barriuso, M. T. Pressure Effects on Cr Cl6 3- Embedded in Cubic Cs2 NaM Cl6 (M=Sc,Y) Lattices: Study through Periodic and Cluster Calculations. *J. Chem. Phys.* **2008**, *128* (14). https://doi.org/10.1063/1.2894546.

(113) Cotton, F. A.; Goodgame, D. M. L.; Goodgame, M. The Electronic Structures of Tetrahedral Cobalt(II) Complexes. *J. Am. Chem. Soc.* **1961**, *83* (23), 4690–4699. https://doi.org/10.1021/ja01484a002.
(114) Pierson, S. A.; Nacham, O.; Clark, K. D.; Nan, H.; Mudryk, Y.; Anderson, J. L. Synthesis and Characterization of Low Viscosity Hexafluoroacetylacetonate-Based Hydrophobic Magnetic Ionic Liquids. *New J. Chem.* **2017**, *41* (13), 5498–5505. https://doi.org/10.1039/c7nj00206h.
(115) Chiappe, C.; Rajamani, S. Structural Effects on the Physico-Chemical and Catalytic Properties of Acidic Ionic Liquids: An Overview. *Eur. J. Org. Chem.* **2011**, No. 28, 5517–5539. https://doi.org/10.1002/ejoc.201100432.
(116) Currie, M.; Estager, J.; Licence, P.; Men, S.; Nockemann, P.; Seddon, K. R.; Swadźba, M.; Kwaśny, S.-K.; Terrade, C. C. Chlorostannate(II) Ionic Liquids: Speciation, Lewis Acidity, and Oxidative Stability. *Inorg Chem* **2013**, *52*. https://doi.org/10.1021/ic300241p.
(117) Brown, L. C.; Hogg, J. M.; Swadz´ba, M.; Kwas´ny, S.-K. Lewis Acidic Ionic Liquids. *Top. Curr. Chem.* **2017**, *375* (78), 1–40. https://doi.org/10.1007/s41061-017-0166-z.
(118) Hitchcock, P. B.; Lewis, R. J.; Welton, T. Vanadyl Complexes in Ambient-Temperature Ionic Liquids. The First x-Ray Crystal Structure of a Tetrachlorooxovanadate(IV) Salt. *Polyhedron* **1993**, *12* (16), 2039–2044. https://doi.org/10.1016/S0277-5387(00)81478-3.
(119) Bakač, A.; Thornton, A. T.; Sykes, A. G. Mechanistic Studies on the Vanadium(II) and Vanadium(III) Reductions of Iodate and Bromate. *Inorg. Chem.* **1976**, *15* (2), 274–278. https://doi.org/10.1021/ic50156a006.
(120) Buglyó, P.; Crans, D. C.; Nagy, E. M.; Lindo, R. L.; Yang, L.; Smee, J. J.; Jin, W.; Chi, L. H.; Godzala, M. E.; Willsky, G. R. Aqueous Chemistry of the vanadiumIII (VIII) and the VIII-Dipicolinate Systems and a Comparison of the Effect of Three Oxidation States of Vanadium Compounds on Diabetic Hyperglycemia in Rats. *Inorg. Chem.* **2005**, *44* (15), 5416–5427. https://doi.org/10.1021/ic048331q.
(121) Gruen, D. M.; McBeth, R. L. ABSORPTION SPECTRA OF THE II, III, IV AND V OXIDATION STATES OF VANADIUM IN LiCl-KCl EUTECTIC. OCTAHEDRAL-TETRAHEDRAL TRANSFORMATIONS OF V(II) AND V(III) 1. *J. Phys. Chem.* **1962**, *66* (1), 57–65. https://doi.org/10.1021/j100807a012.
(122) Seddon, K. R. *Electron Paramagnetic Resonance Spectroscopy of Vanadium(IV) Complexes and Related Species*; 1980.
(123) Sydney Furman, B. C.; Garner, C. S. *Absorption Spectra of Vanadium (III) and Vanadium (IV) Ions in Complexing and Non-Complexing Media*; UTC, 1934; Vol. 3.
(124) Polovov, I. B.; Volkovich, V. A.; Shipulin, S. A.; Maslov, S. V.; Khokhryakov, A. A.; Vasin, B. D.; Griffiths, T. R.; Thied, R. C. Chemistry of Vanadium Chlorides in Molten Salts: An Electronic Absorption Spectroscopy Study. *J. Mol. Liq.* **2003**, *103–104*, 387–394. https://doi.org/10.1016/S0167-7322(02)00156-3.
(125) Bell, R. C.; Castleman, A. W.; Thorn, D. L. Vanadium Oxide Complexes in Room-Temperature Chloroaluminate Molten Salts. *Inorg. Chem.* **1999**, 5709–5715. https://doi.org/10.1021/ic990693o.

(126) Smith, T. S.; LoBrutto, R.; Pecoraro, V. L. Paramagnetic Spectroscopy of Vanadyl Complexes and Its Applications to Biological Systems. *Coord. Chem. Rev.* **2002**, *228* (1), 1–18. https://doi.org/10.1016/S0010-8545(01)00437-4.
(127) Xu, Q.; Qin, L. Y.; Ji, Y. N.; Leung, P. K.; Su, H. N.; Qiao, F.; Yang, W. W.; Shah, A. A.; Li, H. M. A Deep Eutectic Solvent (DES) Electrolyte-Based Vanadium-Iron Redox Flow Battery Enabling Higher Specific Capacity and Improved Thermal Stability. *Electrochimica Acta* **2019**, *293*, 426–431. https://doi.org/10.1016/j.electacta.2018.10.063.
(128) Li, L.; Kim, S.; Wang, W.; Vijayakumar, M.; Nie, Z.; Chen, B.; Zhang, J.; Xia, G.; Hu, J.; Graff, G.; Liu, J.; Yang, Z. A Stable Vanadium Redox-Flow Battery with High Energy Density for Large-Scale Energy Storage. *Adv. Energy Mater.* **2011**, *1* (3), 394–400. https://doi.org/10.1002/aenm.201100008.
(129) Taylor, M. J.; Coddington, J. M. The Constitution of Aqueous Tin(IV) Chloride and Bromide Solutions and Solvent Extracts Studied by 119Sn NMR and Vibrational Spectroscopy. *Polyhedron* **1992**, *11* (12), 1531–1544. https://doi.org/10.1016/S0277-5387(00)83148-4.
(130) Li, Y.-N.; Wang, J.-Q.; He, L.-N.; Yang, Z.-Z.; Liu, A.-H.; Yu, B.; Luan, C.-R. Green Chemistry Experimental and Theoretical Studies on Imidazolium Ionic Liquid-Promoted Conversion of Fructose to 5-Hydroxymethylfurfural †. *Green Chem.* **2012**, 2752–2758. https://doi.org/10.1039/c2gc35845j.
(131) Amarasekara, A. S. Acidic Ionic Liquids. *Chem. Rev.* **2016**, *116* (10), 6133–6183. https://doi.org/10.1021/acs.chemrev.5b00763.
(132) Izgorodina, E. I.; MacFarlane, D. R. Nature of Hydrogen Bonding in Charged Hydrogen-Bonded Complexes and Imidazolium-Based Ionic Liquids. *J. Phys. Chem. B* **2011**, *115* (49), 14659–14667. https://doi.org/10.1021/jp208150b.
(133) Minomura, S.; Drickamer, H. G. Effect of Pressure on the Spectra of Transition Metal Ions in MgO and Al 2 O 3. *J. Chem. Phys.* **1961**, *35* (3), 903–907. https://doi.org/10.1063/1.1701235.
(134) Wang, Y.; Li, H.; Han, S. Structure and Conformation Properties of 1-Alkyl-3-Methylimidazolium Halide Ionic Liquids: A Density-Functional Theory Study. *J Chem Phys* **2005**, *123*, 174501. https://doi.org/10.1063/1.1979478.
(135) Tsuzuki, S.; Katoh, R.; Mikami, M. Analysis of Interactions between 1-Butyl-3-Methylimidazolium Cation and Halide Anions (Cl − , Br − and I −) by Ab Initio Calculations: Anion Size Effects on Preferential Locations of Anions Analysis of Interactions between 1-Butyl-3-Methylimidazolium Cat. *Mol. Phys.* **2008**, *106*, 1621–1629. https://doi.org/10.1080/00268970802258575.
(136) Tsuzuki, S.; Tokuda, H.; Mikami, M. Theoretical Analysis of the Hydrogen Bond of Imidazolium C 2-H with Anions. *Phys. Chem. Chem. Phys.* **2007**, 4780–4784. https://doi.org/10.1039/b707419k.
(137) Weingärtner, H. Understanding Ionic Liquids at the Molecular Level: Facts, Problems, and Controversies. *Angew. Chem. - Int. Ed.* **2008**, *47* (4), 654–670. https://doi.org/10.1002/anie.200604951.
(138) Chen, Z. J.; Xue, T.; Lee, J.-M. What Causes the Low Viscosity of Ether-Functionalized Ionic Liquids? Its Dependence on the Increase of Free Volume. *RSC Adv* **2012**, 10564–10574. https://doi.org/10.1039/c2ra21772d.

(139) Schaltin, S.; Nockemann, P.; Thijs, B.; Binnemans, K.; Fransaer, J. Influence of the Anion on the Electrodeposition of Cobalt from Imidazolium Ionic Liquids. *Electrochem. Solid-State Lett.* **2007**, *10* (10), D104. https://doi.org/10.1149/1.2760185.
(140) Ye, Y.; Elabd, Y. A. Anion Exchanged Polymerized Ionic Liquids: High Free Volume Single Ion Conductors. *Polymer* **2011**, 1309–1317. https://doi.org/10.1016/j.polymer.2011.01.031.
(141) Wellens, S.; Thijs, B.; Binnemans, K. Green Chemistry An Environmentally Friendlier Approach to Hydrometallurgy: Highly Selective Separation of Cobalt from Nickel by Solvent Extraction with Undiluted Phosphonium Ionic Liquids. *Green Chem.* **2012**, 1657. https://doi.org/10.1039/c2gc35246j.
(142) Ueda, T.; Tominaga, T.; Mochida, T.; Takahashi, K.; Kimura, S. Photogeneration of Microporous Amorphous Coordination Polymers from Organometallic Ionic Liquids. *Chem Eur J* **2018**, 9490–9493. https://doi.org/10.1002/chem.201801365.
(143) Funasako, Y.; Mori, S.; Mochida, T. Reversible Transformation between Ionic Liquids and Coordination Polymers by Application of Light and Heat. *Chem. Commun.* **2016**, *52* (37), 6277–6279. https://doi.org/10.1039/c6cc02807a.
(144) Estager, J.; Holbrey, J. D.; Swadźba-Kwaśny, M. Halometallate Ionic Liquids – Revisited. **2014**. https://doi.org/10.1039/c3cs60310e.
(145) Estager, J.; Nockemann, P.; Seddon, K. R.; Swad Zba-Kwa, M.; Tyrrell, S. Validation of Speciation Techniques: A Study of Chlorozincate(II) Ionic Liquids. *Inorg Chem* **2011**, *50*, 16. https://doi.org/10.1021/ic200586u.
(146) Dong, K.; Liu, X.; Dong, H.; Zhang, X.; Zhang, S. Multiscale Studies on Ionic Liquids. *Chem. Rev.* **2017**, 6636–6695. https://doi.org/10.1021/acs.chemrev.6b00776.
(147) Gebbie, M. A.; Smith, A. M.; Dobbs, H. A.; Lee, A. A.; Warr, G. G.; Banquy, X.; Valtiner, M.; Rutland, M. W.; Israelachvili, J. N.; Perkin, S.; Atkin, R. Long Range Electrostatic Forces in Ionic Liquids. *Chem Commun* **2017**, *53*, 1214. https://doi.org/10.1039/c6cc08820a.
(148) Ogawa, T.; Takahashi, K.; Nagarkar, S. S.; Ohara, K.; Hong, Y.-L.; Nishiyama, Y.; Horike, S. Coordination Polymer Glass from Protic Ionic Liquid: Proton Conductivity and Mechanical Property as Electrolyte. https://doi.org/10.1039/D0SC01737J.
(149) Ogiwara, N.; Inukai, M.; Itakura, T.; Horike, S.; Kitagawa, S. Fast Conduction of Organic Cations in Metal Sulfate Frameworks. *Chem. Mater.* **2016**, *28* (11), 3968–3975. https://doi.org/10.1021/acs.chemmater.6b01284.
(150) Ueno, K.; Tokuda, H.; Watanabe, M.; Yoshida, Y.; Saito, G.; Wood, N.; Stephens, G.; MacFarlane, D. R.; Pringle, J. M.; Howlett, P. C.; Forsyth, M.; Hayes, R.; Warr, G. G.; Atkin, R.; Chem, P.; Liu, H.; Liu, Y.; Li, J.; Chem Chem, P.; Höfft, O.; Borisenko, N.; Henrique Gasparotto, L.; Prowald, A.; Al-Salman, R.; Carstens, T.; Bund, A.; Zein El Abedin, S.; Bretthollе, M.; Höfft, O.; Klarhöfer, L.; Mathes, S.; Maus-Friedrichs, W.; Zein El Abedin, S.; Krischok, S.; Janek, J.; Kameyama, T.; Ohno, Y.; Kurimoto, T.; Okazaki, K.; Uematsu, T.; Kuwabata, S.; Krekeler, C.; Dommert, F.; Schmidt, J.; Zhao, Y. Y.; Holm, C.; Berger, R.; Delle, L.; Min Lee, J.; Palgunadi, J.; Hyung Kim, J.; Jung, S.; Choi, Y.; Cheong, M.; Sik Kim, H.; Abbott, A. P.; Qiu, F.; A Abood, H. M.; Rostom Ali, M.; Ryder, K. S.; M Martindale, B. C.; Ward Jones, S. E.; Glyn Jones, S.; Man Yau, H.; Davies, E.; Hook, J. M.; A Youngs, T. G.; Harper, J. B.; Croft, A. K.; Cui, Y.; Biondi, I.; Chaubey, M.; Yang, X.; Fei, Z.; Scopelliti, R.;

Hartinger, C. G.; Li, Y.; Chiappe, C.; Dyson, P. J.; Lunstroot, K.; Driesen, K.; Nockemann, P.; Viau, L.; Hubert Mutin, P.; Vioux, A.; Binnemans, K.; Hayaki, S.; Kido, K.; Sato, H.; Sakaki, S.; Strehmel, V.; Rexhausen, H.; Strauch, P.; Sato, B. M.; de Oliveira, C. G.; Martins, C. T.; El, O. A. Physical Chemistry of Ionic Liquids. *Phys. Chem. Chem. Phys.* **2010**, *12* (8), 1648. https://doi.org/10.1039/c001176m.

(151) Li, H.; Ibrahim, M.; Agberemi, I.; Kobrak, M. N. Viscosity of Typical Room-Temperature Ionic Liquids: A. *Crit. Rev. J. Phys. Chem. Ref. Data* **2008**, *129*, 33101. https://doi.org/10.1063/1.2978378.

(152) Anderson, J. L.; Ding, J.; Welton, T.; Armstrong, D. W. Characterizing Ionic Liquids On the Basis of Multiple Solvation Interactions. *J Am Chem Soc* **2002**, 14247–14254. https://doi.org/10.1021/ja028156h.

(153) Xiao, L.; Wilkes, J. S.; Johnson, K. E. The Molarities of Ionic Liquid Species — Densities Are Not Boring. *ECS Proc. Vol.* **2002**, *2002–19* (1), 964–972. https://doi.org/10.1149/200219.0964PV.

(154) Mecozzi, S.; Rebek, Jr., J. The 55 % Solution: A Formula for Molecular Recognition in the Liquid State. *Chem. - Eur. J.* **1998**, *4* (6), 1016–1022. https://doi.org/10.1002/(SICI)1521-3765(19980615)4:6<1016::AID-CHEM1016>3.0.CO;2-B.

(155) Sutton, E. C.; Mcdevitt, C. E.; Prochnau, J. Y.; Yglesias, M. V; Mroz, A. M.; Yang, M. C.; Cunningham, R. M.; Hendon, C. H.; Derose, V. J. Nucleolar Stress Induction by Oxaliplatin and Derivatives. *J Am Chem Soc* **2019**, *141*, 28. https://doi.org/10.1021/jacs.9b10319.

(156) Mcdevitt, C. E.; Yglesias, M. V; Mroz, A. M.; Sutton, E. C.; Yang, M. C.; Hendon, C. H.; Derose, V. J. Monofunctional Platinum(II) Compounds and Nucleolar Stress: Is Phenanthriplatin Unique? *JBIC J. Biol. Inorg. Chem.* **2019**, *24*, 899–908. https://doi.org/10.1007/s00775-019-01707-9.

(157) Phan, H. T.; Haes, A. J. What Does Nanoparticle Stability Mean? *J. Phys. Chem. C* **2019**, *123* (27), 16495–16507. https://doi.org/10.1021/acs.jpcc.9b00913.

(158) Klajn, R.; Bishop, K. J. M.; Grzybowski, B. A. Light-Controlled Self-Assembly of Reversible and Irreversible Nanoparticle Suprastructures. *Proc. Natl. Acad. Sci.* **2007**, *104* (25), 10305–10309. https://doi.org/10.1073/pnas.0611371104.

(159) Michelson, A.; Minevich, B.; Emamy, H.; Huang, X.; Chu, Y. S.; Yan, H.; Gang, O. Three-Dimensional Visualization of Nanoparticle Lattices and Multimaterial Frameworks. *Science* **2022**, *376* (6589), 203–207. https://doi.org/10.1126/science.abk0463.

(160) Bischoff, M.; Biriukov, D.; Předota, M.; Roke, S.; Marchioro, A. Surface Potential and Interfacial Water Order at the Amorphous TiO2 Nanoparticle/Aqueous Interface. *J. Phys. Chem. C* **2020**, *124* (20), 10961–10974. https://doi.org/10.1021/acs.jpcc.0c01158.

(161) Kim, M.; Jeong, J.; Lu, H.; Lee, T. K.; Eickemeyer, F. T.; Liu, Y.; Choi, I. W.; Choi, S. J.; Jo, Y.; Kim, H.-B.; Mo, S.-I.; Kim, Y.-K.; Lee, H.; An, N. G.; Cho, S.; Tress, W. R.; Zakeeruddin, S. M.; Hagfeldt, A.; Kim, J. Y.; Grätzel, M.; Kim, D. S. Conformal Quantum Dot–SnO2 Layers as Electron Transporters for Efficient Perovskite Solar Cells. *Science* **2022**, *375* (6578), 302–306. https://doi.org/10.1126/science.abh1885.

(162) Zhu, W.; Satterthwaite, P. F.; Jastrzebska-Perfect, P.; Brenes, R.; Niroui, F. Nanoparticle Contact Printing with Interfacial Engineering for Deterministic Integration into Functional Structures. *Sci. Adv.* **2022**, *8* (43), eabq4869. https://doi.org/10.1126/sciadv.abq4869.

(163) Howes, P. D.; Chandrawati, R.; Stevens, M. M. Colloidal Nanoparticles as Advanced Biological Sensors. *Science* **2014**, *346* (6205), 1247390. https://doi.org/10.1126/science.1247390.
(164) Chi, W. S.; Sundell, B. J.; Zhang, K.; Harrigan, D. J.; Hayden, S. C.; Smith, Z. P. Mixed-Matrix Membranes Formed from Multi-Dimensional Metal–Organic Frameworks for Enhanced Gas Transport and Plasticization Resistance. *ChemSusChem* **2019**, *12* (11), 2355–2360. https://doi.org/10.1002/cssc.201900623.
(165) Bachman, J. E.; Smith, Z. P.; Li, T.; Xu, T.; Long, J. R. Enhanced Ethylene Separation and Plasticization Resistance in Polymer Membranes Incorporating Metal-Organic Framework Nanocrystals. *Nat. Mater.* **2016**, *15* (8), 845–849. https://doi.org/10.1038/nmat4621.
(166) Erdosy, D. P.; Wenny, M. B.; Cho, J.; DelRe, C.; Walter, M. V.; Jiménez-Ángeles, F.; Qiao, B.; Sanchez, R.; Peng, Y.; Polizzotti, B. D.; de la Cruz, M. O.; Mason, J. A. Microporous Water with High Gas Solubilities. *Nature* **2022**, *608* (7924), 712–718. https://doi.org/10.1038/s41586-022-05029-w.
(167) Suresh, K.; Aulakh, D.; Purewal, J.; Siegel, D. J.; Veenstra, M.; Matzger, A. J. Optimizing Hydrogen Storage in MOFs through Engineering of Crystal Morphology and Control of Crystal Size. *J. Am. Chem. Soc.* **2021**, *143* (28), 10727–10734. https://doi.org/10.1021/jacs.1c04926.
(168) Pappas, N. S.; Mason, J. A. Effect of Modulator Ligands on the Growth of Co2(Dobdc) Nanorods. *Chem. Sci.* **2023**. https://doi.org/10.1039/D2SC06869A.
(169) Marshall, C. R.; Dvorak, J. P.; Twight, L. P.; Chen, L.; Kadota, K.; Andreeva, A. B.; Overland, A. E.; Ericson, T.; Cozzolino, A. F.; Brozek, C. K. Size-Dependent Properties of Solution-Processable Conductive MOF Nanocrystals. *J. Am. Chem. Soc.* **2022**, *144* (13), 5784–5794. https://doi.org/10.1021/jacs.1c10800.
(170) Decker, G. E.; Stillman, Z.; Attia, L.; Fromen, C. A.; Bloch, E. D. Controlling Size, Defectiveness, and Fluorescence in Nanoparticle UiO-66 through Water and Ligand Modulation. *Chem. Mater.* **2019**, *31* (13), 4831–4839. https://doi.org/10.1021/acs.chemmater.9b01383.
(171) Nag, A.; Kovalenko, M. V.; Lee, J.-S.; Liu, W.; Spokoyny, B.; Talapin, D. V. Metal-Free Inorganic Ligands for Colloidal Nanocrystals: S2–, HS–, Se2–, HSe–, Te2–, HTe–, TeS32–, OH–, and NH2– as Surface Ligands. *J. Am. Chem. Soc.* **2011**, *133* (27), 10612–10620. https://doi.org/10.1021/ja2029415.
(172) Yakin, F. E.; Barisik, M.; Sen, T. Pore Size and Porosity Dependent Zeta Potentials of Mesoporous Silica Nanoparticles. *J. Phys. Chem. C* **2020**, *124* (36), 19579–19587. https://doi.org/10.1021/acs.jpcc.0c04602.
(173) Derjaguin, B. V.; Landau, L. Theory of the Stability of Strongly Charged Lyophobic Sols and of the Adhesion of Strongly Charged Particles in Solutions of Electrolytes. *Acta Physicochim. URSS* **1941**, *14*, 633–662.
(174) Verwey, E. J. W. Theory of the Stability of Lyophobic Colloids. *J. Phys. Colloid Chem.* **1947**, *51* (3), 631–636. https://doi.org/10.1021/j150453a001.
(175) Verwey, E. J. W.; Overbeek, J. Th. G. *Theory of the Stability of Lyophobic Colloids*; Elsevier: Amsterdam, 1948.

(176) Yamamoto, E.; Kitahara, M.; Tsumura, T.; Kuroda, K. Preparation of Size-Controlled Monodisperse Colloidal Mesoporous Silica Nanoparticles and Fabrication of Colloidal Crystals. *Chem. Mater.* **2014**, *26* (9), 2927–2933. https://doi.org/10.1021/cm500619p.
(177) Bouchoucha, M.; Côté, M.-F.; C.-Gaudreault, R.; Fortin, M.-A.; Kleitz, F. Size-Controlled Functionalized Mesoporous Silica Nanoparticles for Tunable Drug Release and Enhanced Anti-Tumoral Activity. *Chem. Mater.* **2016**, *28* (12), 4243–4258. https://doi.org/10.1021/acs.chemmater.6b00877.
(178) Yang, Y.; Qin, H.; Jiang, M.; Lin, L.; Fu, T.; Dai, X.; Zhang, Z.; Niu, Y.; Cao, H.; Jin, Y.; Zhao, F.; Peng, X. Entropic Ligands for Nanocrystals: From Unexpected Solution Properties to Outstanding Processability. *Nano Lett.* **2016**, *16* (4), 2133–2138. https://doi.org/10.1021/acs.nanolett.6b00730.
(179) Guo, A.; Ban, Y.; Yang, K.; Yang, W. Metal-Organic Framework-Based Mixed Matrix Membranes: Synergetic Effect of Adsorption and Diffusion for CO2/CH4 Separation. *J. Membr. Sci.* **2018**, *562*, 76–84. https://doi.org/10.1016/j.memsci.2018.05.032.
(180) Lin, R.; Hernandez, B. V.; Ge, L.; Zhu, Z. Metal Organic Framework Based Mixed Matrix Membranes: An Overview on Filler/Polymer Interfaces. *J. Mater. Chem. A* **2018**, *6* (2), 293–312. https://doi.org/10.1039/C7TA07294E.
(181) Datta, S. J.; Mayoral, A.; Murthy Srivatsa Bettahalli, N.; Bhatt, P. M.; Karunakaran, M.; Carja, I. D.; Fan, D.; Graziane M. Mileo, P.; Semino, R.; Maurin, G.; Terasaki, O.; Eddaoudi, M. Rational Design of Mixed-Matrix Metal-Organic Framework Membranes for Molecular Separations. *Science* **2022**, *376* (6597), 1080–1087. https://doi.org/10.1126/science.abe0192.
(182) DelRe, C.; Hong, H.; Wenny, M. B.; Erdosy, D. P.; Cho, J.; Lee, B.; Mason, J. A. Design Principles for Using Amphiphilic Polymers To Create Microporous Water. *J. Am. Chem. Soc.* **2023**, *145* (36), 19982–19988. https://doi.org/10.1021/jacs.3c06627.
(183) Cravillon, J.; Münzer, S.; Lohmeier, S.-J.; Feldhoff, A.; Huber, K.; Wiebcke, M. Rapid Room-Temperature Synthesis and Characterization of Nanocrystals of a Prototypical Zeolitic Imidazolate Framework. *Chem. Mater.* **2009**, *21* (8), 1410–1412. https://doi.org/10.1021/cm900166h.
(184) Wu, D.; Navrotsky, A. Small Molecule – Silica Interactions in Porous Silica Structures. *Geochim. Cosmochim. Acta* **2013**, *109*, 38–50. https://doi.org/10.1016/j.gca.2013.01.038.
(185) Quan, Z.; Wu, D.; Zhu, J.; Evers, W. H.; Boncella, J. M.; Siebbeles, L. D. A.; Wang, Z.; Navrotsky, A.; Xu, H. Energy Landscape of Self-Assembled Superlattices of PbSe Nanocrystals. *Proc. Natl. Acad. Sci.* **2014**, *111* (25), 9054–9057. https://doi.org/10.1073/pnas.1408835111.
(186) Zhang, X.; Cockreham, C. B.; Yılmaz, E.; Li, G.; Li, N.; Ha, S.; Fu, L.; Qi, J.; Xu, H.; Wu, D. Energetic Cost for Being “Redox-Site-Rich” in Pseudocapacitive Energy Storage with Nickel–Aluminum Layered Double Hydroxide Materials. *J. Phys. Chem. Lett.* **2020**, *11* (9), 3745–3753. https://doi.org/10.1021/acs.jpclett.0c00865.
(187) Li, G.; Sun, H.; Xu, H.; Guo, X.; Wu, D. Probing the Energetics of Molecule–Material Interactions at Interfaces and in Nanopores. *J. Phys. Chem. C* **2017**, *121* (47), 26141–26154. https://doi.org/10.1021/acs.jpcc.7b07450.

(188) Troyano, J.; Carné-Sánchez, A.; Avci, C.; Imaz, I.; Maspoch, D. Colloidal Metal–Organic Framework Particles: The Pioneering Case of ZIF-8. *Chem. Soc. Rev.* **2019**, *48* (23), 5534–5546. https://doi.org/10.1039/C9CS00472F.
(189) Morris, W.; Wang, S.; Cho, D.; Auyeung, E.; Li, P.; Farha, O. K.; Mirkin, C. A. Role of Modulators in Controlling the Colloidal Stability and Polydispersity of the UiO-66 Metal–Organic Framework. *ACS Appl. Mater. Interfaces* **2017**, *9* (39), 33413–33418. https://doi.org/10.1021/acsami.7b01040.
(190) Yang, X.; Zhang, Q.; Liu, Y.; Nian, M.; Xie, M.; Xie, S.; Yang, Q.; Wang, S.; Wei, H.; Duan, J.; Dong, S.; Xing, H. Metal-Organic Framework Nanoparticles with Universal Dispersibility through Crown Ether Surface Coordination for Phase-Transfer Catalysis and Separation Membranes. *Angew. Chem. Int. Ed. n/a* (n/a), e202303280. https://doi.org/10.1002/anie.202303280.
(191) Carey, C. A.; Devlin, A. M.; Matzger, A. J. Dual Modification of MOFs Improves Dispersion and Ionic Conductivity of Mixed Matrix Membranes. *ACS Mater. Lett.* **2023**, 159–164. https://doi.org/10.1021/acsmaterialslett.3c01304.
(192) Schaate, A.; Roy, P.; Godt, A.; Lippke, J.; Waltz, F.; Wiebcke, M.; Behrens, P. Modulated Synthesis of Zr-Based Metal-Organic Frameworks: From Nano to Single Crystals. *Chem. - Eur. J.* **2011**, *17* (24), 6643–6651. https://doi.org/10.1002/chem.201003211.
(193) Butler, E. L.; Reid, B.; Luckham, P. F.; Guldin, S.; Livingston, A. G.; Petit, C. Interparticle Forces of a Native and Encapsulated Metal-Organic Framework and Their Effects on Colloidal Dispersion. *ACS Appl. Mater. Interfaces* **2021**, *13* (38), 45898–45906. https://doi.org/10.1021/acsami.1c13991.
(194) Rojas, S.; Carmona, F. J.; Maldonado, C. R.; Horcajada, P.; Hidalgo, T.; Serre, C.; Navarro, J. A. R.; Barea, E. Nanoscaled Zinc Pyrazolate Metal–Organic Frameworks as Drug-Delivery Systems. *Inorg. Chem.* **2016**, *55* (5), 2650–2663. https://doi.org/10.1021/acs.inorgchem.6b00045.
(195) Tran, E.; Richmond, G. L. Interfacial Steric and Molecular Bonding Effects Contributing to the Stability of Neutrally Charged Nanoemulsions. *Langmuir* **2021**, *37* (43), 12643–12653. https://doi.org/10.1021/acs.langmuir.1c02020.
(196) Derjaguin, B. V.; Churaev, N. V.; Muller, V. M. The Derjaguin—Landau—Verwey—Overbeek (DLVO) Theory of Stability of Lyophobic Colloids. In *Surface Forces*; Derjaguin, B. V., Churaev, N. V., Muller, V. M., Eds.; Springer US: Boston, MA, 1987; pp 293–310. https://doi.org/10.1007/978-1-4757-6639-4_8.
(197) Johny, J.; van Halteren, C. E. R.; Zwiehoff, S.; Behrends, C.; Bäumer, C.; Timmermann, B.; Rehbock, C.; Barcikowski, S. Impact of Sterilization on the Colloidal Stability of Ligand-Free Gold Nanoparticles for Biomedical Applications. *Langmuir* **2022**. https://doi.org/10.1021/acs.langmuir.2c01557.
(198) Zhang, H.; Zhao, M.; Lin, Y. S. Stability of ZIF-8 in Water under Ambient Conditions. *Microporous Mesoporous Mater.* **2019**, *279*, 201–210. https://doi.org/10.1016/j.micromeso.2018.12.035.
(199) Talapin, D. V.; Lee, J.-S.; Kovalenko, M. V.; Shevchenko, E. V. Prospects of Colloidal Nanocrystals for Electronic and Optoelectronic Applications. *Chem. Rev.* **2010**, *110* (1), 389–458. https://doi.org/10.1021/cr900137k.

(200) Herrera-Castro, F.; Torres, L. A. Understanding the Solvation Process and Solute-Solvent Interactions of Imidazole Compounds in Three Different Solvents through Solution Calorimetry and 1H NMR. *J. Mol. Liq.* **2019**, *284*, 232–240. https://doi.org/10.1016/j.molliq.2019.04.002.
(201) Akimbekov, Z.; Wu, D.; Brozek, C. K.; Dincă, M.; Navrotsky, A. Thermodynamics of Solvent Interaction with the Metal–Organic Framework MOF-5. *Phys. Chem. Chem. Phys.* **2016**, *18* (2), 1158–1162. https://doi.org/10.1039/C5CP05370F.
(202) Flory, P. J. Molecular Size Distribution in Linear Condensation Polymers 1. *J. Am. Chem. Soc.* **1936**, *58* (10), 1877–1885. https://doi.org/10.1021/ja01301a016.
(203) Wennerström, H.; Vallina Estrada, E.; Danielsson, J.; Oliveberg, M. Colloidal Stability of the Living Cell. *Proc. Natl. Acad. Sci.* **2020**, *117* (19), 10113–10121. https://doi.org/10.1073/pnas.1914599117.
(204) Israelachvili, J. N.; Wennerstroem, H. Entropic Forces between Amphiphilic Surfaces in Liquids. *J. Phys. Chem.* **1992**, *96* (2), 520–531. https://doi.org/10.1021/j100181a007.
(205) Hobday, C. L.; Woodall, C. H.; Lennox, M. J.; Frost, M.; Kamenev, K.; Düren, T.; Morrison, C. A.; Moggach, S. A. Understanding the Adsorption Process in ZIF-8 Using High Pressure Crystallography and Computational Modelling. *Nat. Commun.* **2018**, *9* (1), 1429. https://doi.org/10.1038/s41467-018-03878-6.
(206) Tan, J. C.; Bennett, T. D.; Cheetham, A. K. Chemical Structure, Network Topology, and Porosity Effects on the Mechanical Properties of Zeolitic Imidazolate Frameworks. *Proc. Natl. Acad. Sci.* **2010**, *107* (22), 9938–9943. https://doi.org/10.1073/pnas.1003205107.
(207) Fairen-Jimenez, D.; Moggach, S. A.; Wharmby, M. T.; Wright, P. A.; Parsons, S.; Düren, T. Opening the Gate: Framework Flexibility in ZIF-8 Explored by Experiments and Simulations. *J. Am. Chem. Soc.* **2011**, *133* (23), 8900–8902. https://doi.org/10.1021/ja202154j.
(208) Zheng, B.; Pan, Y.; Lai, Z.; Huang, K.-W. Molecular Dynamics Simulations on Gate Opening in ZIF-8: Identification of Factors for Ethane and Propane Separation. *Langmuir* **2013**, *29* (28), 8865–8872. https://doi.org/10.1021/la401015m.
(209) Kolokolov, D. I.; Stepanov, A. G.; Jobic, H. Mobility of the 2-Methylimidazolate Linkers in ZIF-8 Probed by 2H NMR: Saloon Doors for the Guests. *J. Phys. Chem. C* **2015**, *119* (49), 27512–27520. https://doi.org/10.1021/acs.jpcc.5b09312.
(210) Tian, T.; Wharmby, M. T.; Parra, J. B.; Ania, C. O.; Fairen-Jimenez, D. Role of Crystal Size on Swing-Effect and Adsorption Induced Structure Transition of ZIF-8. *Dalton Trans.* **2016**, *45* (16), 6893–6900. https://doi.org/10.1039/C6DT00565A.
(211) Coudert, F. Molecular Mechanism of Swing Effect in Zeolitic Imidazolate Framework ZIF-8: Continuous Deformation upon Adsorption. *ChemPhysChem* **2017**, *18* (19), 2732–2738. https://doi.org/10.1002/cphc.201700463.
(212) Vitillo, J. G.; Gagliardi, L. Modeling Metal Influence on the Gate Opening in ZIF-8 Materials. *Chem. Mater.* **2021**, *33* (12), 4465–4473. https://doi.org/10.1021/acs.chemmater.1c00623.
(213) Genix, A.-C.; Bocharova, V.; Carroll, B.; Dieudonné-George, P.; Chauveau, E.; Sokolov, A. P.; Oberdisse, J. How Tuning Interfaces Impacts the Dynamics and Structure of Polymer

Nanocomposites Simultaneously. *ACS Appl. Mater. Interfaces* **2023**, *15* (5), 7496–7510. https://doi.org/10.1021/acsami.2c18083.
(214) Oh, S. M.; Kim, S. Y. Intensified Nonequilibrium Effect of Polymer Nanocomposites with Decreasing Nanoparticle Size. *ACS Appl. Mater. Interfaces* **2023**, *15* (3), 4527–4537. https://doi.org/10.1021/acsami.2c20156.
(215) Sattar, M. A. Interface Structure and Dynamics in Polymer-Nanoparticle Hybrids: A Review on Molecular Mechanisms Underlying the Improved Interfaces. *ChemistrySelect* **2021**, *6* (20), 5068–5096. https://doi.org/10.1002/slct.202100831.
(216) Popov, I.; Carroll, B.; Bocharova, V.; Genix, A.-C.; Cheng, S.; Khamzin, A.; Kisliuk, A.; Sokolov, A. P. Strong Reduction in Amplitude of the Interfacial Segmental Dynamics in Polymer Nanocomposites. *Macromolecules* **2020**, *53* (10), 4126–4135. https://doi.org/10.1021/acs.macromol.0c00496.
(217) Popov, I.; Cheng, S.; Sokolov, A. P. Broadband Dielectric Spectroscopy and Its Application in Polymeric Materials. In *Macromolecular Engineering*; Hadjichristidis, N., Gnanou, Y., Matyjaszewski, K., Muthukumar, M., Eds.; Wiley, 2022; pp 1–39. https://doi.org/10.1002/9783527815562.mme0059.
(218) Yavitt, B. M.; Salatto, D.; Zhou, Y.; Huang, Z.; Endoh, M.; Wiegart, L.; Bocharova, V.; Ribbe, A. E.; Sokolov, A. P.; Schweizer, K. S.; Koga, T. Collective Nanoparticle Dynamics Associated with Bridging Network Formation in Model Polymer Nanocomposites. *ACS Nano* **2021**, *15* (7), 11501–11513. https://doi.org/10.1021/acsnano.1c01283.
(219) Saiz, P. G.; Reizabal, A.; Vilas-Vilela, J. L.; Lanceros-Mendez, S.; Dalton, P. D. Thermochromic Responses on Melt Electrowritten Poly(ϵ-Caprolactone) Microstructures. *ACS Appl. Polym. Mater.* **2023**, *5* (6), 3883–3887. https://doi.org/10.1021/acsapm.3c00427.
(220) Neese, F. Software Update: The ORCA Program System, Version 4.0. *Wiley Interdiscip. Rev. Comput. Mol. Sci.* **2018**, *8* (1), 1–6. https://doi.org/10.1002/wcms.1327.
(221) Weigend, F.; Ahlrichs, R. Balanced Basis Sets of Split Valence, Triple Zeta Valence and Quadruple Zeta Valence Quality for H to Rn: Design and Assessment of Accuracy. *Phys. Chem. Chem. Phys.* **2005**, *7* (18), 3297. https://doi.org/10.1039/b508541a.
(222) Rappoport, D.; Furche, F. Property-Optimized Gaussian Basis Sets for Molecular Response Calculations. *J Chem Phys* **2010**, *133*, 134105. https://doi.org/10.1063/1.3484283.
(223) Weigend, F. Accurate Coulomb-Fitting Basis Sets for H to Rn. *Phys. Chem. Chem. Phys.* **2006**, *8* (9), 1057. https://doi.org/10.1039/b515623h.
(224) Zhao, Y.; Truhlar, D. G. A New Local Density Functional for Main-Group Thermochemistry, Transition Metal Bonding, Thermochemical Kinetics, and Noncovalent Interactions. *J Chem Phys* **2006**, *125*, 194101. https://doi.org/10.1063/1.2370993.
(225) Barone, V.; Cossi, M. Quantum Calculation of Molecular Energies and Energy Gradients in Solution by a Conductor Solvent Model. *J. Phys. Chem. A* **1998**, *102* (11), 1995–2001. https://doi.org/10.1021/jp9716997.
(226) Chen, S.; Izgorodina, E. I. Prediction of 1 H NMR Chemical Shifts for Clusters of Imidazolium-Based Ionic Liquids †. *Phys Chem Chem Phys* **2017**, *19*, 17411. https://doi.org/10.1039/c7cp02951a.

(227) M. J. Frisch, G. W. Trucks, H. B. Schlegel, G. E. Scuseria, M. A. Robb, J. R. Cheeseman, G. Scalmani, V. Barone, G. A. Petersson, H. Nakatsuji, X. Li, M. Caricato, A. Marenich, J. Bloino, B. G. Janesko, R. Gomperts, B. Mennucci, H. P. Hratchian, J. V. Ort, and D. J. F. Gaussian 09, Revision A.02. Gaussian, Inc.: Wallingford CT 2016.

(228) Zhao, Y.; Truhlar, D. G.; Zhao, Y.; Truhlar, · D G. The M06 Suite of Density Functionals for Main Group Thermochemistry, Thermochemical Kinetics, Noncovalent Interactions, Excited States, and Transition Elements: Two New Functionals and Systematic Testing of Four M06-Class Functionals and 12 Other Functionals and Inorganometallic Chemistry and for Noncovalent Interactions. *Theor Chem Acc.* **2008**, *120*, 215–241. https://doi.org/10.1007/s00214-007-0310-x.

(229) Yanai, T.; Tew, D. P.; Handy, N. C. A New Hybrid Exchange-Correlation Functional Using the Coulomb-Attenuating Method (CAM-B3LYP). *Chem. Phys. Lett.* **2004**, *393* (1–3), 51–57. https://doi.org/10.1016/j.cplett.2004.06.011.